

REPORT DOCUMENTATION PAGE			Form Approved OMB NO. 0704-0188		
<p>The public reporting burden for this collection of information is estimated to average 1 hour per response, including the time for reviewing instructions, searching existing data sources, gathering and maintaining the data needed, and completing and reviewing the collection of information. Send comments regarding this burden estimate or any other aspect of this collection of information, including suggestions for reducing this burden, to Washington Headquarters Services, Directorate for Information Operations and Reports, 1215 Jefferson Davis Highway, Suite 1204, Arlington VA, 22202-4302. Respondents should be aware that notwithstanding any other provision of law, no person shall be subject to any penalty for failing to comply with a collection of information if it does not display a currently valid OMB control number.</p> <p>PLEASE DO NOT RETURN YOUR FORM TO THE ABOVE ADDRESS.</p>					
1. REPORT DATE (DD-MM-YYYY) 01-12-2017		2. REPORT TYPE Final Report		3. DATES COVERED (From - To) 1-Jul-2011 - 31-Dec-2016	
4. TITLE AND SUBTITLE Final Report: Chip-Scale, Ultra-Sensitive Opto-Mechanical Acceleration and Force Sensors			5a. CONTRACT NUMBER W911NF-11-1-0173		
			5b. GRANT NUMBER		
			5c. PROGRAM ELEMENT NUMBER 0D10BM		
6. AUTHORS			5d. PROJECT NUMBER		
			5e. TASK NUMBER		
			5f. WORK UNIT NUMBER		
7. PERFORMING ORGANIZATION NAMES AND ADDRESSES California Institute of Technology Office of Sponsored Research 1200 E. California Blvd. Pasadena, CA 91125 -0001			8. PERFORMING ORGANIZATION REPORT NUMBER		
9. SPONSORING/MONITORING AGENCY NAME(S) AND ADDRESS (ES) U.S. Army Research Office P.O. Box 12211 Research Triangle Park, NC 27709-2211			10. SPONSOR/MONITOR'S ACRONYM(S) ARO		
			11. SPONSOR/MONITOR'S REPORT NUMBER(S) 60166-PH-DRP.10		
12. DISTRIBUTION AVAILABILITY STATEMENT Approved for public release; distribution is unlimited.					
13. SUPPLEMENTARY NOTES The views, opinions and/or findings contained in this report are those of the author(s) and should not be construed as an official Department of the Army position, policy or decision, unless so designated by other documentation.					
14. ABSTRACT					
15. SUBJECT TERMS					
16. SECURITY CLASSIFICATION OF:			17. LIMITATION OF ABSTRACT UU	15. NUMBER OF PAGES	19a. NAME OF RESPONSIBLE PERSON Oskar Painter
a. REPORT UU	b. ABSTRACT UU	c. THIS PAGE UU			19b. TELEPHONE NUMBER 626-395-8008

# RPPR Final Report

as of 20-Dec-2017

Agency Code:

Proposal Number: 60166PHDRP  
**INVESTIGATOR(S):**

**Agreement Number: W911NF-11-1-0173**

**Name:** Oskar J. Painter Ph.D.  
**Email:** opainter@caltech.edu  
**Phone Number:** 6263958008  
**Principal:** Y

Organization: **California Institute of Technology**

Address: Office of Sponsored Research, Pasadena, CA 911250001

Country: USA

DUNS Number: 009584210

EIN: 951643307

**Report Date:** 31-Mar-2017

**Date Received:** 01-Dec-2017

**Final Report** for Period Beginning 01-Jul-2011 and Ending 31-Dec-2016

**Title:** Chip-Scale, Ultra-Sensitive Opto-Mechanical Acceleration and Force Sensors

**Begin Performance Period:** 01-Jul-2011

**End Performance Period:** 31-Dec-2016

**Report Term:** 0-Other

Submitted By: Oskar Painter

Email: opainter@caltech.edu

Phone: (626) 395-8008

**Distribution Statement:** 1-Approved for public release; distribution is unlimited.

**STEM Degrees:** 2

**STEM Participants:** 2

**Major Goals:** Our efforts within the DARPA/ARO QuASAR program are focused on developing chip-scale optomechanical (OM) inertial sensors. Our approach involves the use of nanoscale photonic crystal optical resonators for sensitive optical read-out of mechanical motion, and nanoscale tethers for low-mechanical-dissipation anchoring of the mechanical proof mass. Our primary program goal was to develop an optomechanical accelerometer with bandwidth of 10kHz and noise-equivalent acceleration (NEA) less than 100 nano-gee/sqrt(Hz) ["gee"=10m/s<sup>2</sup>]. We also explored the realization of OM gyros based upon similar optomechanical structures.

**Accomplishments:** See uploaded pdf.

**Training Opportunities:** During the QuASAR program there were 4 PhD students, 2 undergraduate summer research students, and a post-doc who were provided training. Also, during the course of the program 2 of these graduate students received their PhDs.

**Results Dissemination:** A complete list of our QuASAR-related publications are listed below for reference, and are freely available via Caltech authors (<https://authors.library.caltech.edu/>):

1. A. G. Krause, M. Winger, T. D. Blasius, Q. Lin, and O. Painter, "A high-resolution microchip optomechanical accelerometer," *Nature Photonics*, doi:10.1038/nphoton.2012.245, October 14, 2012.
2. Amir H. Safavi-Naeini and Oskar Painter, "Optomechanical Crystal Devices," a book chapter in *Cavity Optomechanics: Nano- and Micromechanical Resonators Interacting with Light*, July 7, 2014 (Springer link).
3. Alex G. Krause, Tim D. Blasius, and Oskar Painter, "Optical read out and feedback cooling of a nanostring optomechanical cavity," arXiv:1506.01249, June 3, 2015.
4. Alex G. Krause, "Acceleration Sensing, Feedback Cooling, and Nonlinear Dynamics with Nanoscale Cavity-Optomechanical Devices," PhD Thesis, California Institute of Technology (2015).
5. Tim D. Blasius, "Optomechanical Inertial Sensors and Feedback Cooling," PhD Thesis, California Institute of Technology (2016).

**Honors and Awards:** Nothing to Report

# RPPR Final Report

as of 20-Dec-2017

## Protocol Activity Status:

**Technology Transfer:** Two patents related to our work during the QuASAR program were granted:

“Optomechanical disk vibratory gyroscope,” Patent Number: 9,389,079

“Systems and Methods for Tuning a Cavity,” Patent Number: 8,849,075

We also have a third patent application under review:

“Optomechanical accelerometer,” Patent Application, Pub. No.2015/0020590

## PARTICIPANTS:

**Participant Type:** PD/PI

**Participant:** Oskar Painter

**Person Months Worked:** 2.00

**Funding Support:**

Project Contribution:

International Collaboration:

International Travel:

National Academy Member: N

Other Collaborators:

**Participant Type:** Co PD/PI

**Participant:** Qiang Lin

**Person Months Worked:** 3.00

**Funding Support:**

Project Contribution:

International Collaboration:

International Travel:

National Academy Member: N

Other Collaborators:

**Participant Type:** Postdoctoral (scholar, fellow or other postdoctoral position)

**Participant:** Justin Cohen

**Person Months Worked:** 2.00

**Funding Support:**

Project Contribution:

International Collaboration:

International Travel:

National Academy Member: N

Other Collaborators:

**Participant Type:** Graduate Student (research assistant)

**Participant:** Greg MacCabe

**Person Months Worked:** 12.00

**Funding Support:**

Project Contribution:

International Collaboration:

International Travel:

National Academy Member: N

Other Collaborators:

## ARTICLES:

## RPPR Final Report as of 20-Dec-2017

**Publication Type:** Journal Article      Peer Reviewed: N      **Publication Status:** 0-Other

**Journal:** arXiv

**Publication Identifier Type:** Other

**Publication Identifier:** arXiv:1506.01249

**Volume:**

**Issue:**

**First Page #:**

**Date Submitted:** 11/30/17 12:00AM

**Date Published:** 6/5/15 3:20AM

**Publication Location:**

**Article Title:** Optical read out and feedback cooling of a nanostring optomechanical cavity

**Authors:** Alex G. Krause, Timothy D. Blasius, Oskar Painter

**Keywords:** optomechanics, photonic crystals

**Abstract:** Optical measurement of the motion of a 940 kHz mechanical resonance of a silicon nitride nanostring resonator is demonstrated with a read out noise imprecision reaching 37 dB below that of the resonator's zero-point fluctuations. Via intensity modulation of the optical probe laser, radiation pressure feedback is used to cool and damp the mechanical mode from an initial room temperature occupancy of  $6.5 \times 10^6$  (295 K) down to a phonon occupation of 66, representing a mode temperature of 3 mK. The five decades of cooling is enabled by the system's large single-photon cooperativity ( $C1 = 4$ ) and high quantum efficiency of optical motion detection (0:27).

**Distribution Statement:** 1-Approved for public release; distribution is unlimited.

**Acknowledged Federal Support:** Y

### DISSERTATIONS:

**Publication Type:** Thesis or Dissertation

**Institution:** California Institute of Technology

**Date Received:** 30-Nov-2017

**Completion Date:** 1/13/16 11:14AM

**Title:** Optomechanical Inertial Sensors and Feedback Cooling

**Authors:** Timothy D. Blasius

**Acknowledged Federal Support:** N

**Publication Type:** Thesis or Dissertation

**Institution:** California Institute of Technology

**Date Received:** 30-Nov-2017

**Completion Date:** 1/11/15 4:38AM

**Title:** Acceleration Sensing, Feedback Cooling, and Nonlinear Dynamics with Nanoscale Cavity-Optomechanical Devices

**Authors:** Alexander G. Krause

**Acknowledged Federal Support:** N

### PATENTS:

**Intellectual Property Type:** Patent

**Date Received:** 30-Nov-2017

**Patent Title:** SYSTEMS AND METHODS FOR TUNING A CAVITY

**Patent Abstract:** The present disclosure describes an integrated opto-mechani

**Patent Number:** US 8,849,075 B2

**Patent Country:** USA

**Application Date:** 10-Nov-2012

**Application Status:** 3

**Date Issued:** 01-Dec-2014

**Intellectual Property Type:** Patent

**Date Received:** 30-Nov-2017



**RPPR Final Report**  
as of 20-Dec-2017

**Patent Title:** Optomechanical Disk Vibratory Gyroscopes

**Patent Abstract:** An integrated optomechanical disk vibratory gyroscope device includes a mechanical oscillator l

**Patent Number:** US 9,389,079 B2

Patent Country: USA

Application Date: 21-Feb-2015

Application Status: 3

Date Issued: 13-Jul-2016

## Grant Summary Report

**Sponsor:** DARPA/Army Research Office (ARO)

**Sponsor Award Number:** W911NF-11-1-0173

**Award Title:** Chip-Scale, Ultra-Sensitive Optomechanical Accelerator and Force Sensors

**Reporting Period:** 01-Jul-2011 31-DEC-2016

**Principal Investigator:** Prof. Oskar Painter, California Institute of Technology (CIT)

**co-Principal Investigators:** Prof. Qiang Lin (University of Rochester)

**Report Prepared by:** Prof. Oskar Painter (CIT)

**Abstract:** Our efforts within the DARPA/ARO QuASAR program are focused on developing chip-scale optomechanical (OM) inertial sensors. Our approach involves the use of nanoscale photonic crystal optical resonators for sensitive optical read-out of mechanical motion, and nanoscale tethers for low-mechanical-dissipation anchoring of the mechanical proof mass. Our primary program goal was to develop an optomechanical accelerometer with bandwidth of 10kHz and noise-equivalent acceleration (NEA) less than 100 nano-gee/sqrt(Hz) [gee=10m/s<sup>2</sup>]. We also explored the realization of OM gyros based upon similar optomechanical structures.

**Summary of Key Findings and Research Activities:** Below we provide an introduction to optomechanical accelerometer sensing and to the zipper cavity sensor developed under the QuASAR program. Finally, we also describe our efforts to develop an optomechanical gyro. Details of all of our research efforts during the QuASAR program are described in our publications, which we do not reproduce here. We recommend that these should be read for full comprehension of our work, in particular the PhD thesis of Tim Blasius. A complete list of our QuASAR-related publications are listed below for reference, and are freely available via Caltech authors (<https://authors.library.caltech.edu/>):

1. A. G. Krause, M. Winger, T. D. Blasius, Q. Lin, and O. Painter, "A high-resolution microchip optomechanical accelerometer," *Nature Photonics*, doi:10.1038/nphoton.2012.245, October 14, 2012.
2. Amir H. Safavi-Naeini and Oskar Painter, "Optomechanical Crystal Devices," a book chapter in *Cavity Optomechanics: Nano- and Micromechanical Resonators Interacting with Light*, July 7, 2014 (Springer link).
3. Alex G. Krause, Tim D. Blasius, and Oskar Painter, "Optical read out and feedback cooling of a nanostring optomechanical cavity," arXiv:1506.01249, June 3, 2015.
4. Alex G. Krause, *Acceleration Sensing, Feedback Cooling, and Nonlinear Dynamics with Nanoscale Cavity-Optomechanical Devices*, PhD Thesis, California Institute of Technology (2015).
5. Tim D. Blasius, "Optomechanical Inertial Sensors and Feedback Cooling," PhD Thesis, California Institute of Technology (2016).

### A. Zipper Cavity Optomechanical Accelerometer

#### I Introduction

The radiation pressure interaction of light enables precise measurement of mechanical motion. Perhaps the most powerful and well-known example of this is LIGO - the Laser Interferometer

Gravitational-wave Observatory. LIGO features kg scale mirrors separated by km distances and stored optical powers on the order of 10 kW (advanced LIGO may approach 1 MW [1]). The current stored optical power in LIGO's optical cavities is at the level of 100 kW, which has enabled LIGO to achieve a displacement resolution of  $\sim 10^{-19} \frac{m}{\sqrt{Hz}}$ , with advanced LIGO having a roadmap to  $\sim 10^{-20} \frac{m}{\sqrt{Hz}}$  [1, 2]. Using similar physics, the nano-scale zipper cavities studied in this program are capable of achieving a displacement resolution on the order of  $10^{-16} \frac{m}{\sqrt{Hz}}$ , or 1/10 of a proton radius (see Ref. [3]). With this resolution, one is naturally led to consider the practical applications of such a sensor. The most straightforward application that comes to mind is acceleration sensing. Typical accelerometers operate by monitoring the displacement of a flexibly mounted test mass, see Fig. 1.

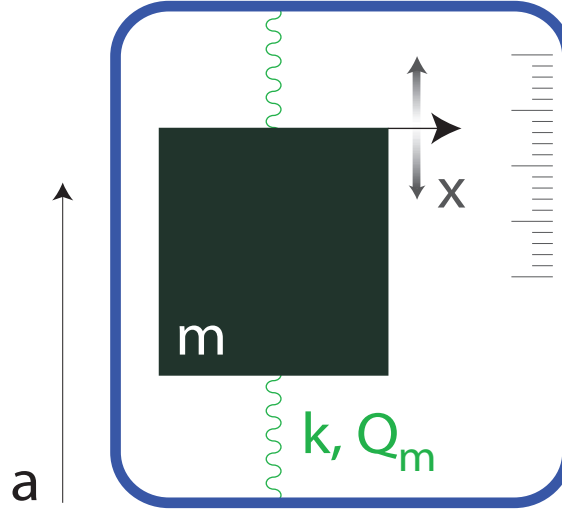


FIG. 1. **Canonical Accelerometer.** This figure is a cartoon of a canonical accelerometer. The test mass (dark square) is flexibly mounted via springs (green) with stiffness  $k$  and quality factor  $Q_m$  to a rigid frame (blue rectangle). If the frame undergoes an acceleration,  $a$ , the test mass will move an amount  $x$ , which can be read-out.

Due to the rapid development of silicon micromachining technology, microelectromechanical systems (MEMS) accelerometers have become exceedingly popular over the past two decades [4]. The monitoring of acceleration is essential for a variety of applications ranging from inertial navigation to consumer electronics [4, 5]. Different technological applications for MEMS accelerometers have diverse requirements for their performance. For example, sensors for inertial navigation require low noise and bias stability [6], but large bandwidth is crucial for sensors in acoustics and vibrometry applications [7]. The read-out of test-mass motion can be accomplished using capacitive [8, 9], piezo-electric [10], piezo-resistive [11], tunnel-current [12], or optical methods [13–16]. Optical detection has some added benefits in that it provides resilience to electromagnetic interference and allows for long-range readout [17]. Fig. 2 shows a plot of displacement resolution versus bandwidth for various examples of these detection schemes. As can be seen in Fig. 2, our optomechanical detection scheme can provide superior displacement resolution. We therefore set out to make an optomechanical accelerometer.

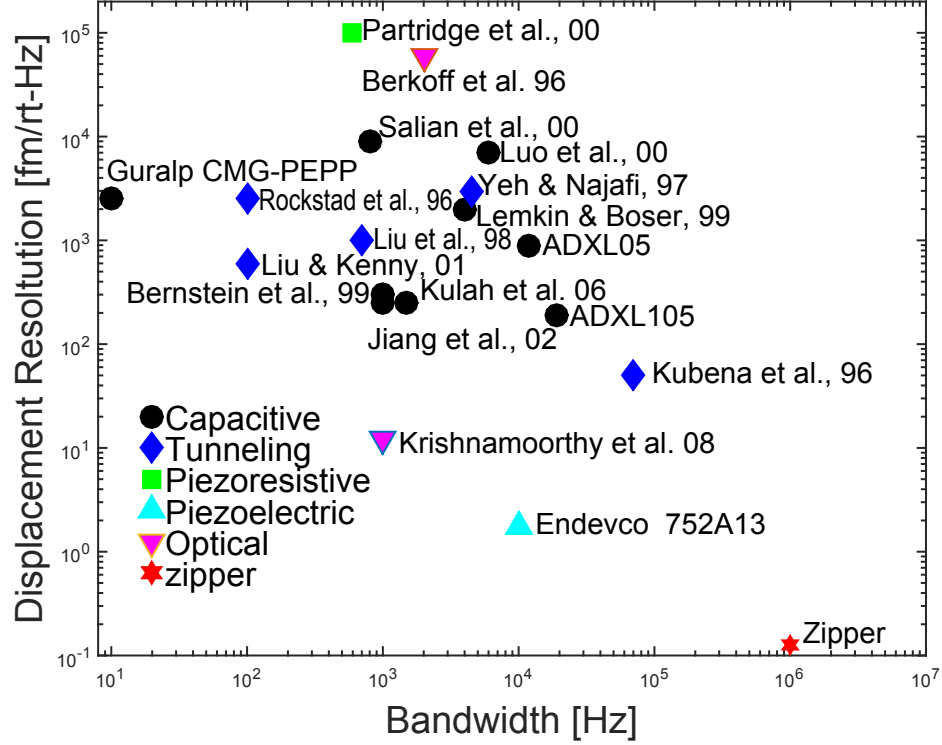


FIG. 2. **Sensor Displacement Resolution.** This figure plots displacement resolution versus bandwidth for various sensors and is adapted from Ref. [18]. “Partridge et al., 00” is Ref. [11]. “Berkoff et al., 96” is Ref. [16]. “Salian et al., 00” is Ref. [19]. “Luo et al., 00” is Ref. [20]. “Yeh & Najafi, 97” is Ref. [21]. “Rockstad et al., 96” is Ref. [22]. “Guralp CMG-PEPP” is Ref. [23]. “Lemkin & Boser, 99” is Ref. [24]. “Liu et al., 98” is Ref. [12]. “ADXL05” is Ref. [25]. “Liu & Kenny, 01” is Ref. [26]. “Bernstein et al., 99” is Ref. [27]. “ADXL105” is Ref. [28]. “Kulah et al., 06” is Ref. [9]. “Jiang et al., 02” is Ref. [18]. “Kubena et al., 96” is Ref. [29]. “Krishnamoorthy et al 08” is Ref. [13]. “Endevco 752A13” is Ref. [30]. “Zipper” is our own work on zipper photonic crystals from Ref. [31].

## II Accelerometer Noise and Design

While displacement resolution is certainly an important figure of merit for accelerometer performance, it is far from the only one. Here we describe the various sources of acceleration noise relevant for our optomechanical accelerometer. This will also serve to motivate the design of our sensor.

### A Thermal Brownian motion ( $a_{th}$ )

The mechanical resonator that comprises the accelerometer undergoes thermal fluctuations due to its finite temperature (room temperature in the devices studied in this work). Specifically, the displacement power spectral density (PSD) due to thermal noise is:

$$S_{xx}^{th}(\omega) = \frac{4k_B T \omega_m}{m Q_m} \frac{1}{(\omega^2 - \omega_m^2)^2 + \left(\frac{\omega \omega_m}{Q_m}\right)^2} = \frac{4k_B T \omega_m}{m Q_m} |\chi(\omega)|^2 \quad (1)$$

These fluctuations will be indistinguishable from displacements due to signals we wish to detect, and hence they represent an important and fundamental noise floor.

We now wish to obtain an expression for the acceleration PSD due to thermal noise of the test mass,  $S_{aa}^{\text{th}}(\omega)$ . Eq. (1) was obtained using the fundamental fluctuating thermal force  $S_{FF}(\omega) = 4k_B T m \gamma$ . From Newton's law,  $a = F/m$ , and thus we have the following:

$$S_{aa}^{\text{th}} = \frac{4k_B T \omega_m}{m Q_m}, \quad (2)$$

$$a_{\text{th}} = \sqrt{\frac{4k_B T \omega_m}{m Q_m}}, \quad (3)$$

where we have defined thermal acceleration noise,  $a_{\text{th}} = \sqrt{S_{aa}^{\text{th}}}$ . Note that  $a_{\text{th}}$  is independent of frequency. This is simply a consequence of the white thermal force noise and that the resonator's susceptibility to thermal forces is the same as that for applied external forces.

Naturally, we wish to minimize  $a_{\text{th}}$  as much as possible. For the original zipper devices [3],  $a_{\text{th}}$  is actually quite large. The mechanical parameters were  $\omega_m = 2\pi \times 8$  MHz,  $m = 40 \times 10^{-15}$  kg,  $Q_m = 1.6 \times 10^4$  (in vacuum). This leads to  $a_{\text{th}} \cong 4$  milli- $g/\sqrt{\text{Hz}}$ . We have introduced a new acceleration unit here,  $g = 9.81 \frac{m}{s^2}$ , which is the acceleration due to gravity at the earth's surface (one "ghee").

Looking at the equation for  $a_{\text{th}}$  it is easy to pick out which parameters are under our control:  $k_B$  is Boltzmann's constant, an immutable constant of the universe;  $T$  for practical accelerometers is set by room temperature, 295 K;  $\omega_m$  is set by the bandwidth needed for the application. The vast majority of accelerometer applications are at acoustic frequencies or less [13]. Therefore, we leave  $\omega_m$  on the order of 10 kHz, and don't treat it as an optimization parameter. This leaves us simply with mass,  $m$ , and quality factor,  $Q$ , as optimization parameters. To minimize  $a_{\text{th}}$ , we want to make both as large as possible.

The final design for our first demonstration of an optomechanical acceleration is shown in Fig. 3. The effective mass was increased to  $10 \times 10^{-12}$  kg by simply adding a large rectangle of silicon nitride to one of the optical beams, see Fig. 3a. In order to increase the mechanical  $Q$ -factor the nanostrings connecting the test mass to the bulk of the chip were made as long and as thin as feasible given our fabrication techniques. The nanostring dimensions are  $150 \text{ nm} \times 560 \mu\text{m} \times 400 \text{ nm}$ , and the measured mechanical  $Q$  of this structure in vacuum is,  $Q_m = 1.4$  million [32] (how this  $Q_m$  is measured is discussed in Section III). The high stress in the nanostrings leads to a frequency of the fundamental in-plane mechanical mode of  $\omega_m = 2\pi \times 27.5$  kHz. A COMSOL finite-element simulation [33] of the in-plane mechanical mode is shown in Fig. 3c (not to scale). Taken together, these parameters imply  $a_{\text{th}} \cong 1.4 \frac{\mu\text{-}g}{\sqrt{\text{Hz}}}$ , a very significant improvement from the original zippers.

## B Detector noise ( $a_{\text{det}}$ )

An additional source of noise for our optomechanical accelerometer will be the electronic noise of the photodetector used to detect the laser light. This electronic noise is usually quantified by its noise-equivalent-optical-power (NEP). For the Newport 2117 detector and the transimpedance gain setting used in this work we have  $\text{NEP} = \sqrt{S_{\text{pp}}^{\text{NEP}}} = 2.8 \text{ pW}/\sqrt{\text{Hz}}$ . Here we utilize direct photodetection so we can convert from the optical power spectral density for NEP to an effective displacement PSD directly. Furthermore, since  $x[\omega] = \chi(\omega) a[\omega]$  we can convert the displacement PSD to an acceleration PSD. Taken all together yields the following results:

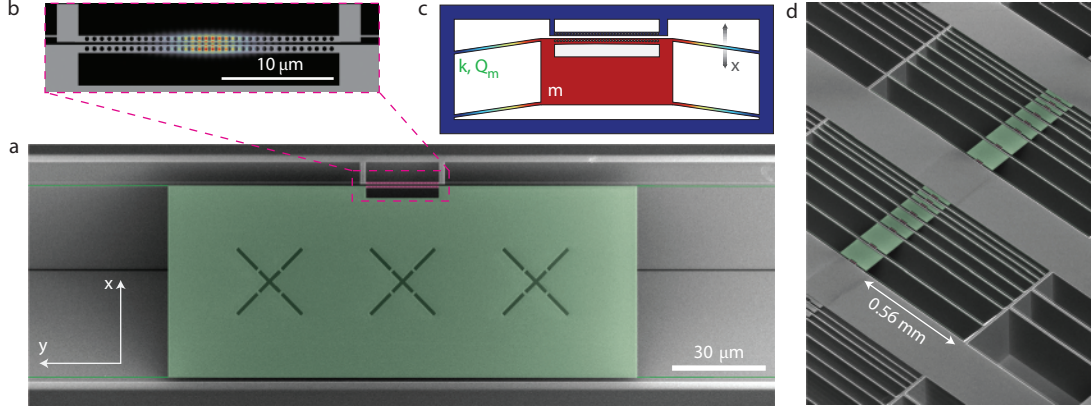


**FIG. 3. Optomechanical Accelerometer Design.** (a) False-colored SEM image of an optomechanical accelerometer. Highlighted in green is the test mass and the nanostrings. The test mass is a rectangle of suspended silicon nitride of dimensions  $150 \mu\text{m} \times 60 \mu\text{m} \times 400 \text{nm}$ . The cross pattern is simply a fabrication technique to allow KOH to get underneath the test mass and more efficiently release it from the underlying silicon. The nanostrings are highly stressed silicon nitride of dimension  $150 \text{nm} \times 560 \mu\text{m} \times 400 \text{nm}$ . These dimensions serve to maximize the mechanical quality factor. The photonic crystal cavity where mechanical motion is sensed, is highlighted in pink. (b) Zoom-in of the optical cavity region showing the magnitude of the electric field,  $|\mathbf{E}(\mathbf{r})|$ , for the fundamental bonded mode of the zipper cavity. The top beam is rigidly connected to the bulk of the chip and can be considered effectively motionless relative to the chip. The bottom beam is connected to the flexible test mass. (c) Illustration of the displacement profile (not to scale) of the fundamental in-plane mechanical mode used for acceleration sensing. (d) SEM image of an array of devices with different test mass sizes.

$$S_{\text{pp}}^{\text{NEP}} = \text{NEP}^2 \quad (4)$$

$$S_{\text{xx}}^{\text{NEP}} = \frac{\text{NEP}^2}{\left(\frac{dR}{d\Delta} P_{\text{in}} \eta g_{\text{OM}}\right)^2} \quad (5)$$

$$S_{\text{aa}}^{\text{NEP}} = \frac{\text{NEP}^2}{\left(\frac{dR}{d\Delta} P_{\text{in}} \eta g_{\text{OM}}\right)^2 |\chi(\omega)|^2} \quad (6)$$

$$a_{\text{NEP}} = \sqrt{S_{\text{aa}}^{\text{NEP}}} = \frac{\text{NEP}}{\left(\frac{dR}{d\Delta} P_{\text{in}} \eta g_{\text{OM}}\right) |\chi(\omega)|} \quad (7)$$

For the parameters used in the experiment of this chapter, including the laser being half an optical linewidth red-detuned from the optical resonance,  $a_{\text{NEP}} = 4.1 \mu\text{g}/\sqrt{\text{Hz}}$ , at frequencies much lower than  $\omega_{\text{m}}$ .

### C Shot noise ( $a_{\text{SN}}$ )

The laser light field used to probe the optical cavity has intrinsic quantum shot noise. This shot noise obeys poissonian statistics and, accordingly, the variance of the detected photon number will simply be,  $n_{\text{det}}$ , which is the number of photons hitting the detector. This leads to the optical power

spectral density for shot noise.

$$S_{pp}^{SN} = 2 (\hbar\omega_\ell)^2 n_{\text{det}}\eta_{qe} = 2\hbar\omega_\ell P_{\text{det}}\eta_{qe} \quad (8)$$

We have included a factor of 2 for using the single-sided power spectral density.  $P_{\text{det}}$  is the optical power at the detector and  $\eta_{qe}$  is the quantum efficiency of the detector. From here we can use the steps as in the previous section, Section II B, to derive the effective shot noise displacement PSD and acceleration PSD.

$$S_{xx}^{SN} = \frac{2\hbar\omega_\ell P_{\text{det}}\eta_{qe}}{\left(\frac{dR}{d\Delta} P_{in}\eta g_{OM}\right)^2} \quad (9)$$

$$S_{aa}^{SN} = \frac{2\hbar\omega_\ell P_{\text{det}}\eta_{qe}}{\left(\frac{dR}{d\Delta} P_{in}\eta g_{OM}\right)^2 |\chi(\omega)|^2} \quad (10)$$

$$a_{SN} = \sqrt{S_{aa}^{SN}} = \frac{\sqrt{2\hbar\omega_\ell P_{\text{det}}\eta_{qe}}}{\left(\frac{dR}{d\Delta} P_{in}\eta g_{OM}\right) |\chi(\omega)|} \quad (11)$$

For the parameters of the experiment to be described in this section,  $a_{SN} = 8.9 \mu - g/\sqrt{\text{Hz}}$ , near DC (low frequency). To make sure extra classical laser noise was not limiting this experiment, we split the laser into two paths with one arm entering the accelerometer optical cavity and the other bypassing it and equal power reaching the detector from both arms. The two paths were detected on a balanced photodetector, which subtracted the two signals. This leaves the accelerometer signal unchanged, but any classical laser noise suppressed. The shot noise in such a scheme is due to the total optical power hitting the detector, or twice the optical power in any one arm.

#### D Back-Action Noise ( $a_{BA}$ )

In addition to providing a sensor read-out imprecision limit, the shot noise of the light field also imparts a force on, and cause motion of, the mechanical resonator. The acceleration PSD due to back-action is given by:

$$S_{aa}^{ba} = \frac{8 (\hbar g_{OM})^2 n_c}{m^2 \kappa} \quad (12)$$

The resulting noise-equivalent acceleration for the parameters used in this experiment is  $a_{ba} = \sqrt{S_{aa}^{ba}} = 5.6 \text{ nano} - g/\sqrt{\text{Hz}}$ . This is much smaller than all other noise sources and can effectively be ignored.

### III Experimental Setup and Device Characterization

Testing and characterization of the accelerometer shown in Fig. 3 was done using the experimental setup shown in Fig. 4. We used a New Focus velocity laser, which is a narrow-bandwidth ( $< 300 \text{ kHz}$ ), 1500 nm telecom band, tunable external cavity diode laser. The laser light is split with a beamsplitter; the signal arm is sent through a fiber polarization controller (FPC) and a fiber taper coupled to the optical cavity, while the other arm is sent directly to a balanced photodetector (BPD). Variable optical attenuators (VOA) in each arm balance the powers. The optomechanical accelerometer chip along with commercial accelerometers are placed on top of a “shake table” composed of a shear piezo. By applying tones from a signal generator to the shear piezo, controlled

accelerations can be applied and calibrated using the commercial accelerometers. Transduced accelerations are measured using either an electronic spectrum analyzer (ESA) or a lock-in amplifier.

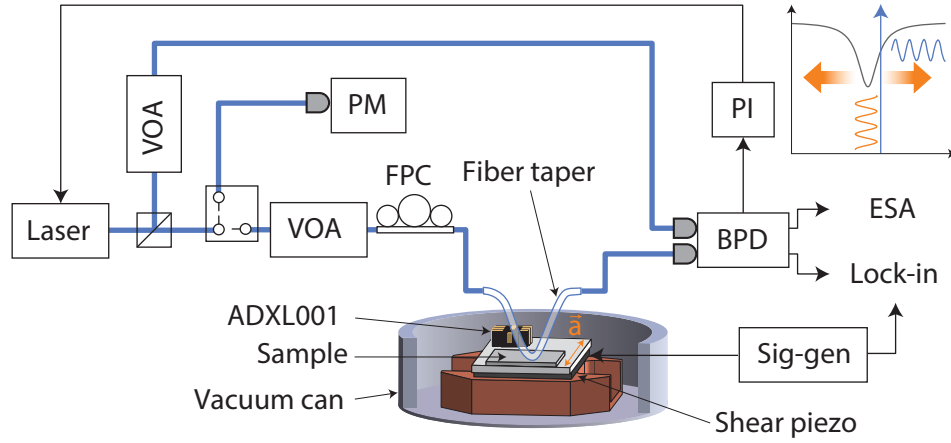


FIG. 4. **Experimental Setup.** Laser light used to probe the zipper cavity motion is split with a beamsplitter; the signal arm is sent through a fiber polarization controller (FPC) and a fiber taper coupled to the optical cavity, while the other arm is sent directly to a balanced photodetector (BPD). Variable optical attenuators (VOA) in each arm balance the powers, and a power meter (PM) is used to calibrate the probe power. The BPD signal is sent to a proportional-integral controller (PI) locking the laser half a linewidth red-detuned from the optical resonance (lock frequency  $< 10$  Hz). The sample is mounted on a shake table comprised of a shear piezo. Transduced accelerations are measured using either an electronic spectrum analyzer (ESA) or a lock-in amplifier.

As shown in Fig. 4, laser light is coupled into the cavity using a dimpled, tapered optical fiber. By scanning the laser frequency across the telecom band we obtain the transmission spectrum of the fundamental bonded mode of the optical cavity as shown in Fig. 5. The measured optical resonance was at a wavelength of  $\lambda_0 = 1537$  nm and had a quality factor of  $Q_0 = 9500$ .

After characterizing the optical mode, the laser is locked using a proportion-integral (PI) controller (see Fig. 4) half a linewidth red-detuned from the optical cavity resonance. This is the point of greatest slope on the laser transmission curve and allows us to transduce mechanical motion with greatest sensitivity. Note that the PI lock only has a bandwidth of  $< 10$  Hz. If the bandwidth were not limited, the lock would cancel out signals that we're interested as well as the slow drifts. We employ a balanced detection scheme, which allows for efficient rejection of classical laser amplitude noise, yielding shot noise limited detection for frequencies above  $\sim 1$  kHz. The power spectrum of the output of our balanced photodetector with a laser power incident at the optical cavity of,  $P_{in} = 116 \mu W$ , half a linewidth red-detuned from the optical resonance is shown in Fig. 6.

The fundamental in-plane mechanical mode (illustrated in Fig. 3) is largest transduced resonance feature at  $\omega_m = 2\pi \times 27.5$  kHz, see Fig. 6. This is in good agreement with finite-element method simulations in COMSOL, from which we also extracted the effective mass,  $m = 10 \times 10^{-12}$  kg. In principle, the mechanical quality factor can be determined by fitting the PSD to the form of Eq. (1) and extracting the  $Q_m$  fit parameter. In practice, the sub-Hz linewidths of our mechanical modes make establishing the quality factor from the PSD measured on a spectrum ana-



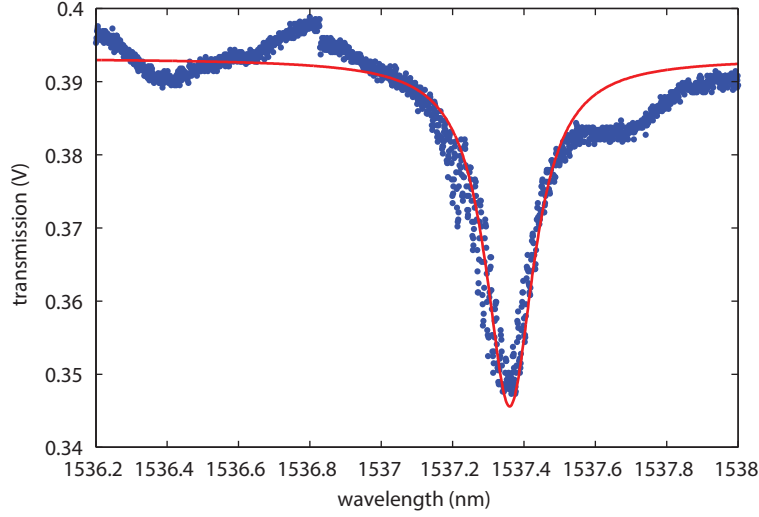


FIG. 5. **Optical Cavity Transmission Spectrum.** This figure plots the unnormalized optical transmission spectrum of the fundamental bonded optical mode of the accelerometer’s zipper cavity.

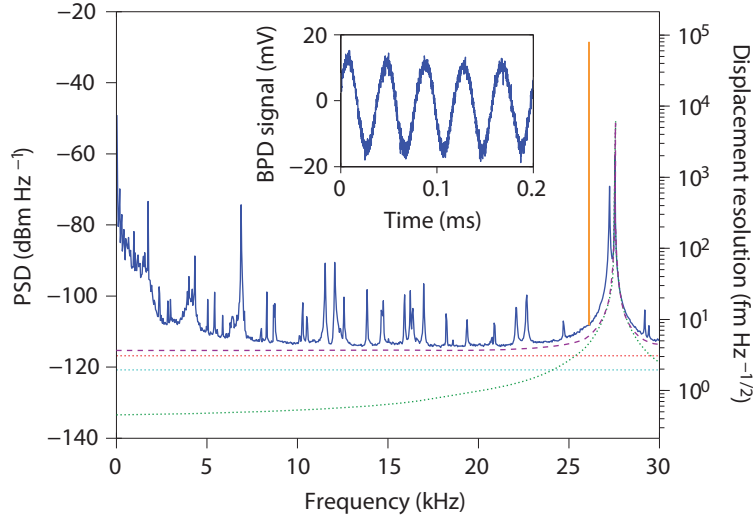
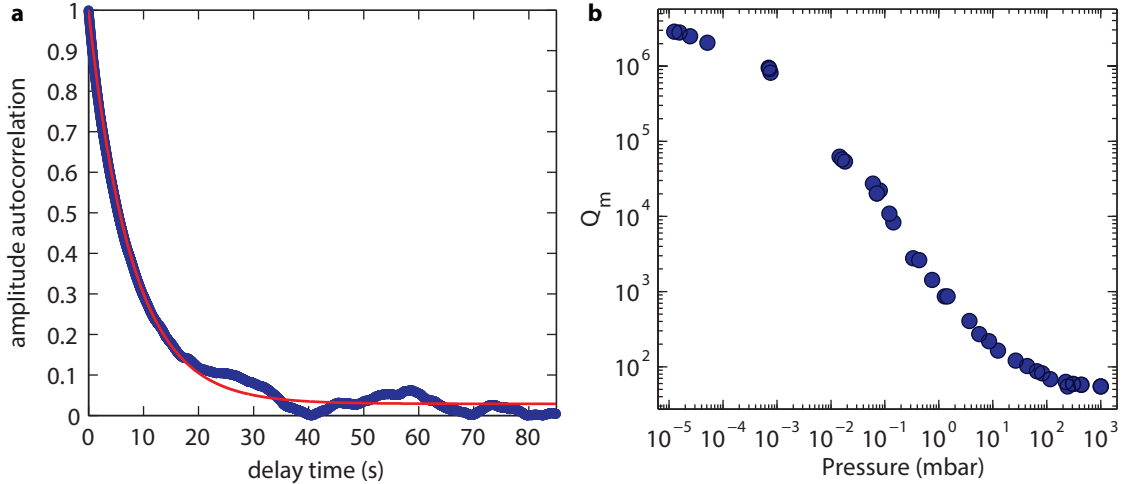


FIG. 6. **Optical Power Spectral Density.** Left, axis: optical PSD of the BPD signal showing the fundamental in-plane mechanical mode at 27.5 kHz. Right axis: equivalent displacement noise. The tone at 26 kHz (orange) is transduction of a tone applied to the shear piezo corresponding to an rms acceleration of 38.9 milli-g. The dashed and dotted lines are theoretical noise levels for shot noise (red), detector noise (cyan), thermal noise (green), and total of all noise contributions (purple). Inset: time trace of the transduction of an applied acceleration of 35.6 milli-g at 25 kHz.

lyzer infeasible because it requires a fractional stability of the mechanical frequency much greater than  $1/Q_m \approx 5 \times 10^{-7}$  over a time period much longer than the decay time  $Q_m/\omega_m > 10$  s. However, since the system is driven by a Gaussian thermal noise process, the autocorrelation of

the amplitude  $\langle x(t)x(t+\tau) \rangle$  can be shown to decay as  $e^{-\frac{t}{\tau}}$ , from which the quality factor can be obtained as  $Q_m = \tau\omega_m$  [34, 35]. The slowly-varying envelope of  $\langle x(t) \rangle$  is obtained from the magnitude channel of a lock-in amplifier tuned to the mechanical resonance frequency with a bandwidth ( $\approx 100$  Hz) much larger than the linewidth, which ensures that small frequency diffusion does not affect the measurement of the envelope. To obtain the bare mechanical Q-factors the measurement is made at an optical power low enough to ensure there is no back-action. The autocorrelation is numerically computed and the decay is fit to an exponential curve with a constant (noise) offset. In Fig. 7a we show an autocorrelation trace of the devices presented in the main text calculated from  $\approx 3000$  s of data sampled at 100 Hz and fit to find  $\tau = 7.85$  s and for  $\omega_m = 2\pi \times 27.5$  kHz that yields  $Q_m = 1.4 \times 10^6$ . For lower-Q structures, it was confirmed that this technique agrees with a direct measurement of the linewidth from a spectrum analyzer.

Since gas damping severely limits the mechanical Q-factor of our oscillator, measurements were carried out in vacuum. Fig. 7b, shows pressure-dependent mechanical Q-factors using a device of equal mass to the device shown in Fig. 3, but with 70 nanostring tethers, resulting in an eigenfrequency of  $\omega_m = 2\pi \times 110$  kHz. We find that the device exhibits a Q-factor of 53 at ambient pressure, which strongly increases when reducing the pressure in the vacuum chamber. In particular, for pressures below  $10^{-3}$  mbar – the regime in which we carried out our acceleration resolution measurements ( $\lesssim 2 \times 10^{-5}$  mbar) – we observe Q-factors above  $10^6$ .



**FIG. 7. Investigation of Mechanical Q-factors.** (a) Autocorrelation trace of the thermal noise driven mechanical amplitude. The signal was obtained from computing the autocorrelation of the slowly varying magnitude of the mechanical motion returned from a lock-in amplifier, using the experimental setup of Fig. 4. Fitting the trace with an exponential decay yields the time constant and thereby the mechanical Q-factor of the mode ( $Q_m = 1.4 \times 10^6$ ). (b) Pressure-dependence of the mechanical Q-factor of a control device with  $m = 10^{-11}$  kg and 70 nanostring tethers, showing an increase from  $Q_m \approx 53$  to  $Q_m \approx 2.5 \times 10^6$  in high vacuum.

Careful calibration of our optical mode parameters, input power, optical losses from the cavity to the detector,  $\eta = 0.57$ , and mechanical mode parameters allow us to calibrate our value of  $g_{OM}$ . Furthermore, for the  $g_{OM}$  calibration, we use low optical powers where back-action effects are negligible, and therefore the mechanical mode's effective temperature is room temperature. Under

these experimental conditions, fitting the optical PSD in the vicinity of the mechanical resonance at  $\omega_m = 27.5$  kHz yields the optomechanical coupling constant,  $g_{\text{OM}} = 2\pi \times 5.5$  GHz/nm. From electromagnetic finite-element simulations in Comsol using zipper cavity dimensions determined by scanning electron microscopy (SEM), we calculate  $g_{\text{OM}} = 2\pi \times 13.5$  GHz/nm, in relatively good agreement with the measured value.

#### IV Calibration: Accelerometer Sensitivity and Resolution

With knowledge of the optical, mechanical, and noise sources of the optomechanical sensor, one can calibrate the accelerometric performance of the zipper cavity. As previously mentioned, this calibration is done by driving a shear piezo upon which our accelerometer and commercial sensors sit; see Fig. 4. Applying a sinusoidal voltage to the shear piezo results in a harmonic in-plane acceleration,  $a(\omega)$ , and thus modulation of the transmitted optical power. The optical power in the modulation sideband is given by,

$$P_m(\omega) = P_{\text{in}} \eta \frac{dT}{d\Delta} g_{\text{OM}} |\chi(\omega) a(\omega)|. \quad (13)$$

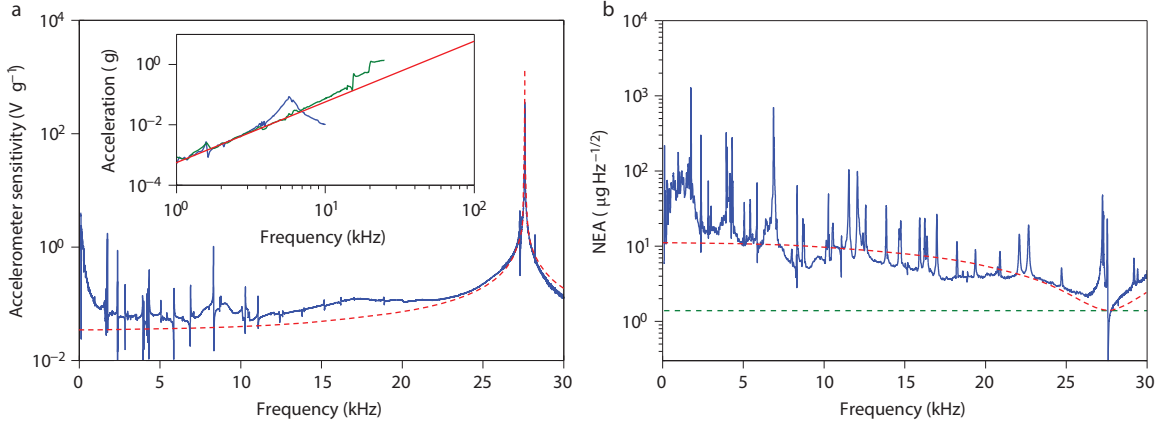
In Eq. (13),  $T$  is the normalized cavity transmission, the un-normalized cavity transmission for this experiment is plotted in Fig. 5. An example of such an applied acceleration tone is shown in Fig. 6. The narrow tone at 26 kHz (orange) arises from an applied root-mean square (rms) acceleration of  $a_{\text{rms}} = 38.9$  mg, calibrated using the two commercial accelerometers mounted on the shake table. From the signal-to-noise ratio of this calibration tone, we estimate  $a_{\text{th}} = 2.0 \mu\text{g}/\sqrt{\text{Hz}}$ , comparable to the predicted theoretical value of  $a_{\text{th}} = 1.4 \mu\text{g}/\sqrt{\text{Hz}}$ . This confirms that the fundamental in-plane mechanical mode at 27.5 kHz is largely driven by room-temperature thermal noise.

Fig. 8a shows the demodulated photodiode signal (using the lock-in amplifier, see Fig. 4) normalized to the applied acceleration as a function of drive frequency, corresponding to the frequency-dependent acceleration sensitivity of the zipper cavity. The inset of Fig. 8a presents the data from the commercial accelerometers used to calibrate the applied acceleration. The dashed red line is the theoretical calculation of the sensitivity without fit parameters and shows excellent agreement. The sharp, Fano-shaped features for lower frequencies can again be attributed to mechanical resonances of the fiber-taper waveguide. The broad region of apparent higher sensitivity around 15 kHz is due to an underestimate of the applied acceleration arising from an acoustic resonance of the shake table.

The calibrated frequency-dependent acceleration resolution, or noise-equivalent acceleration NEA, is shown in Fig. 8b. It was obtained by normalizing the PSD in Fig. 6 with the sensitivity curve in Fig. 8a. This is the same procedure as discussed for the tone at 26 kHz in Fig. 6. A known acceleration tone is applied and the noise floor is calibrated using the signal-to-noise ratio of this tone. Between 25 and 30 kHz, the resolution is limited by the thermal noise of the oscillator, and from 5 to 25 kHz, shot noise limits the resolution to  $\sim 10 \mu\text{g}/\sqrt{\text{Hz}}$ . For frequencies lower than 5 kHz, motion of the fiber-taper waveguide and the environment contribute extra noise. The sharp Fano-shaped feature at 27 kHz arises from interference with the fundamental out-of-plane mode of the test mass. The dashed red curve corresponds to a theoretical estimate of the NEA given shot noise and thermal noise, and shows good agreement. The dashed green line is the fundamental thermal noise sensing limit,  $a_{\text{th}}$ .

With a demonstrated acceleration resolution on the order of a few  $\mu\text{g}/\sqrt{\text{Hz}}$  and a bandwidth above 25 kHz, the zipper cavity device presented here shows performance comparable to the best

MEMs commercial sensors [30].



**FIG. 8. Frequency-dependence of sensitivity and resolution.** (a) Sensitivity curve as a function of frequency, obtained by driving the shear piezo with a sinusoidal voltage and measuring the amplitude of the resulting voltage modulation of the BPD signal using a lock-in amplifier. The dashed red line corresponds to the theoretical expectation for the sensitivity without fit parameters. Inset: data from commercial accelerometers also attached to the shake table (blue and green curves), which were used for calibrating the applied acceleration (best-fit line, solid red curve). (b) Frequency-dependent NEA of the device, quantifying its broadband resolution. The plot is obtained by taking the PSD in Fig. 6 and normalizing it with the sensitivity in (a). The dashed red line depicts the theoretical expectation for the NEA given shot noise and thermal noise limitations. The green dashed curve corresponds to the thermal noise,  $a_{th}$ .

## V Moving Forward

Encouraged by the excellent acceleration resolution of the initial zipper cavity optomechanical accelerometer, several avenues of improvement for the device's performance and practicality were pursued throughout the QuASAR program, including but not limited to: (i) fiber-coupled on-chip waveguides [15, 36] enable convenient small form-factor packaging as well facilitating the removal of noise associated with the current fiber-taper coupling, and (ii) integration of electrostatic tuning capacitors [37] allow dynamic tuning of the optical cavity resonance frequency, enabling replacement of expensive tunable lasers with cheaper and essentially fixed-wavelength laser sources which can be fabricated on-chip [38]. Additionally, the thermal noise performance of our sensor can easily be enhanced by an order of magnitude by adding mass. Naively, adding mass would decrease the mechanical resonance frequency, thereby, sacrificing bandwidth. However, by increasing the number of nanostring tethers commensurate with the mass increase, the frequency can be held constant. Moreover, increasing the number of tethers to 140 does not greatly affect the mechanical quality factor. Furthermore, by increasing the mass by several orders of magnitude, the same  $a_{th}$  performance can be achieved with lower mechanical quality factor. Lower  $Q_m$  devices are more stable to shock inputs and can be operated in higher air pressure environments (see Fig. 7b), relaxing packaging constraints.

## B. Improvements in the Zipper Cavity OMA

The first demonstration of the zipper cavity optomechanical accelerometer (OMA) described above was an important proof of principle. However, there remains significant room for improvement

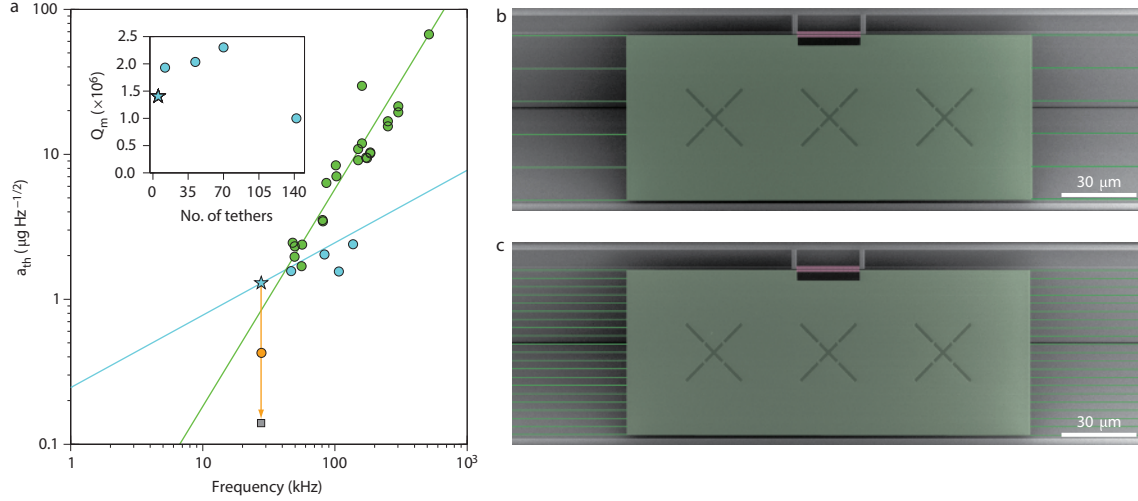


**FIG. 9. Future Directions: adding mass and nanostrings.** (a) Thermal acceleration noise density of measured devices (green, cyan, and orange data points). The starred point represents the device discussed in this chapter. The green line is that traversed for adding mass with fixed  $Q_m$  and spring constant,  $k$ , and the cyan line is obtained for varying  $k$  while keeping  $Q_m$  and  $m$  fixed. Varying both  $m$  and  $k$  allows for independent control of bandwidth and resolution, for example along the orange line, where  $\frac{k}{m}$  is constant and  $Q_m$  is fixed. The grey point represents the theoretical device performance for the test mass increased by a factor of 100 over that in this chapter. Inset:  $Q_m$  for devices corresponding to the cyan circles in (a) versus the number of nanostring tethers attached to the test mass. (b)(c) False-color SEM images of devices with 12 (b) and 42 (c) nanostring tethers and  $\omega_m = 2\pi \times 46$  kHz (b) and  $\omega_m = 2\pi \times 83$  kHz (c), respectively.

in the sensor design and implementation. Throughout the course of the QuASAR program we made significant improvements in the original zipper cavity OMA in the following principle areas: (i) robust optical coupling using optical fibers mounted in precision aligned V-grooves, (ii) implementation of an electrostatic (capacitively driven) tuning mechanism for dynamic control and trimming of the optical cavity resonance wavelength, (iii) characterization and demonstration of sensor read-out using hybrid III-V-silicon semiconductor laser diodes provided by Intel, (iv) identification, characterization, and mitigation of low frequency sensor noise, and (v) development of a new fabrication technique for realization of sensors with increased test mass size by approximately 4 orders of magnitude, realizing a thermal noise resolution less than  $100 \text{ ng}/\sqrt{\text{Hz}}$  at atmospheric pressure. We detail each of these developments in the sections that follow below.

## VI V-groove Fiber Coupled Accelerometer

Example V-groove fiber coupled accelerometers are shown in Fig. 10. The mechanical resonator component of the accelerometer is of identical design to that in part A. . The V-groove optical coupling method was designed in Ref. [36]. The on-chip waveguide can either take a 90-degree turn, Fig. 10f, or continue straight to the optical cavity, Fig. 10g. The data presented in this section were taken on devices similar to that in Fig. 10g.

The fabrication methods used to make these devices are similar to the original zipper cavity devices, with one technical detail omitted. When fabricating devices of the design shown in Fig. 10g, the KOH release step was done in two parts, with the first KOH etch defining the V-groove and

the second releasing the mechanical resonator and optical cavity. This was done to avoid the deleterious consequences of excessive etching of convex corners. Such a two step KOH release was accomplished by first spinning on a photosensitive protective coating for alkaline etches called Protek PSB by Brewer Science. The region of this coating covering the V-groove region was then exposed to UV radiation and removed upon development. The KOH etch to define the V-groove was then performed, then the remaining PSB was removed in a piranha solution, then the remaining structure was released in the second KOH etch, and then, finally, the structure was rinsed and critical-point dried.

Of particular importance to this section is the optical fiber in Fig. 10f. As one can see in this false-colored SEM image, the optical fiber is securely glued into the silicon V-groove. This is accomplished by slowly lowering the cleaved optical fiber into the V-groove using micrometer stages while monitoring with an optical microscope and then fixing the fiber with ultraviolet (UV) cure epoxy. Once secured, the fiber can sustain even moderate tugs by human hands without budging. By contrast, our standard dimpled, tapered optical fiber is attached to the surface only by van der Waals forces and is known to jump after small bumps of the optical table upon which the testing setup sits. This means the V-groove coupling method is much more robust and useful for practical sensors. Moreover, the rigid connection of the fiber to the substrate suppresses its mechanical motion, shifting its mechanical modes to higher frequencies outside the range of interest.

That mechanical motion of the optical fiber is no longer a problem is shown by comparing Fig. 6 to Fig. 11. Fig. 11 is the optical power spectral density of light collected on reflection from the optical cavity with the laser locked half a linewidth red-detuned from the optical cavity. Note that all of the sharp fiber taper resonances seen in Fig. 6 are no longer present. This represents a significant improvement in the device performance, which is further highlighted by the noise equivalent acceleration plotted in the inset of Fig. 11. This resolution was determined by assuming the fundamental in-plane mechanical mode was dominantly driven by room-temperature thermal noise, an assumption supported by Section IV. Note that the source of the low-frequency noise roll-up is determined and significantly reduced in Section IX.

Using the autocorrelation technique described in Section III, the intrinsic mechanical quality factor (i.e. at low enough optical power that back-action is insignificant) of the fundamental in-plane mechanical mode is found to be,  $Q_m \cong 2 \times 10^6$ . The reader will note the linewidth of the mode of interest in Fig. 11 is much larger than this  $Q$ -factor would suggest, and is a result of the thermo-opto-mechanical cooling. That is, the mode is both damped and cooled due to interactions with the laser light, leaving the fundamental thermal acceleration noise, Eq. (3), unchanged. A plot of the quality factor and effective mode temperature of the fundamental in-plane mechanical mode versus incident power in the optical fiber is shown in Fig. 12. Once again, the effective temperature is found using the integrated area of the mechanical mode in the PSD. For calibration we assume at low optical powers that the mode temperature is room-temperature,  $T = 295$  K.

The optical mode used to measure the spectra and acceleration resolution of Fig. 11 is shown in Fig. 13. The fitted optical  $Q$ -factor is  $Q_o = 16,500$ . Using this and the assumption that at low enough optical power the mechanical mode is at room-temperature, the optomechanical coupling is calibrated from the integrated mechanical motion to be  $g_{om} = 2\pi \times 6.4$  GHz/nm. The series of fringes in the wide optical scan are interpreted to be Fabry-Pérot fringes. From the free spectral range of the fringes,  $\Delta\lambda = 0.5$  nm, the effective length of the Fabry-Pérot cavity can be inferred to be,  $L_{\text{eff}} = \frac{\lambda^2}{2n_{\text{SiN}}\Delta\lambda} \cong 1.2$  mm. This corresponds to the optical path length from the cleaved facet of the optical fiber to the photonic crystal cavity. We therefore conclude that the Fabry-Pérot cavity causing these fringes is resulting from reflections from the cleaved fiber facet and the



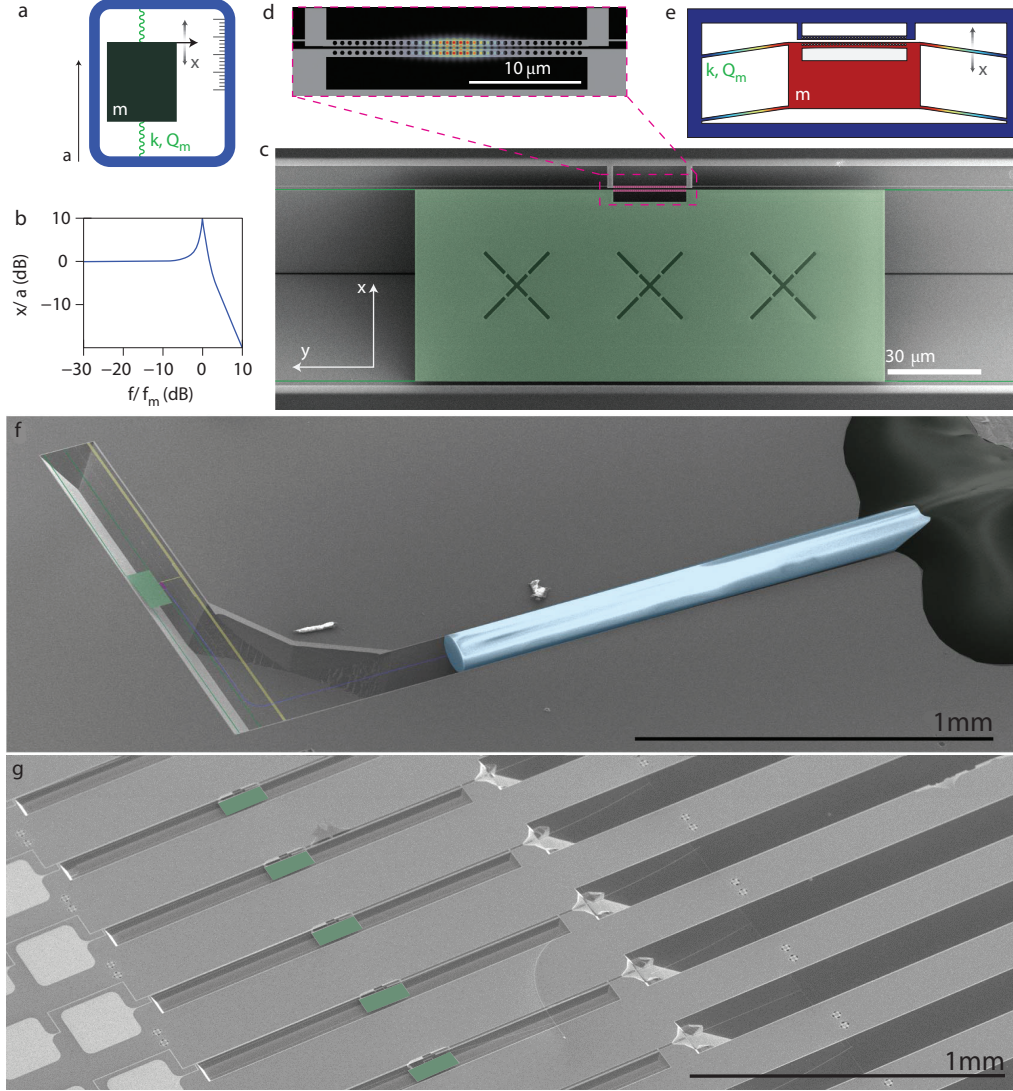


**FIG. 10. V-groove Fiber Coupled Accelerometer .** (a) Canonical accelerometer from Fig. 1 shown again. (b) Plot of the mechanical susceptibility for  $Q_m = 10$ . (c) Zoom-in of an example test mass with the photonic crystal cavity attached. (d) Zoom-in of the photonic crystal cavity region with the norm of the fundamental bonded electric field mode plotted. (e) Finite-element simulation of the fundamental in-plane mechanical mode of the accelerometer (note: not to scale). (f) Zoom-out showing an optical fiber securely glued into a silicon V-groove and coupling into an on-chip waveguide, which carries light to and from the accelerometer photonic crystal cavity. (g) Image showing a series of accelerometers coupled to V-grooves in a straight-line configuration. The data in Fig. 11 was taken on a device with this geometry.

end mirror of the photonic crystal cavity. While these fringes are an annoying side-effect of this coupling scheme, they do allow for calibration of the coupling losses, i.e. the amount of light lost between the cleaved fiber facet and the photonic crystal cavity. The system is modeled as a Fabry-Pérot cavity where the first mirror (the fiber facet) has a reflection coefficient,  $R_{\text{fib}}$ , and the second mirror (the mirror section of the photonic crystal) has unit reflection coefficient, and

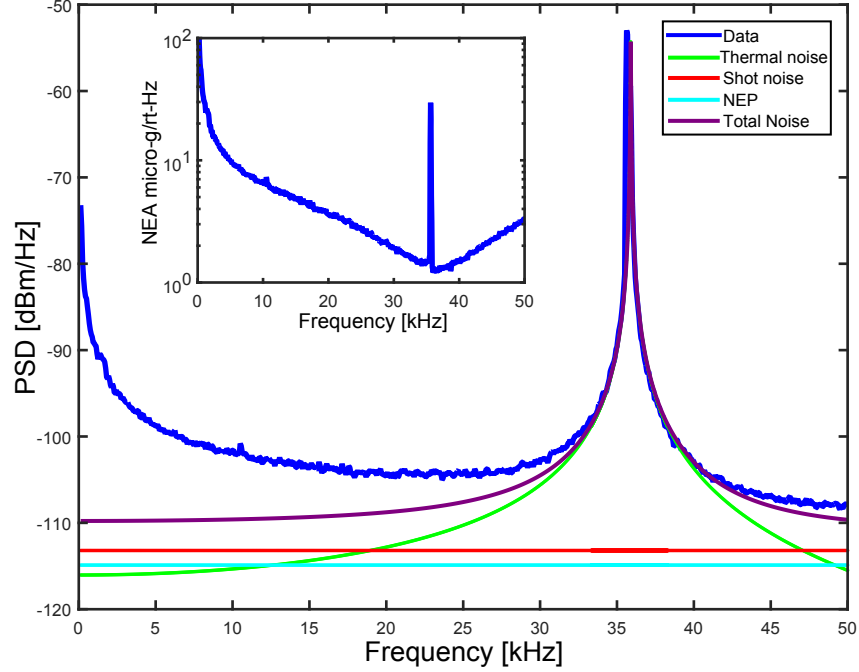


FIG. 11. **V-groove Fiber Coupled PSD.** The main plot is the power spectral density of the photodiode signal with the laser locked half a linewidth red-detuned from the photonic crystal cavity resonance. The thermal noise of the fundamental in-plane mechanical mode is fit in green. The sharp peak near the fitted mechanical resonance is the fundamental out-of-plane mechanical resonance of the accelerometer. Note that it appears slightly better transduced than the fundamental in-plane mode because the in-plane mode is significantly cooled by the optomechanical damping caused by the laser. (inset) The acceleration resolution (noise equivalent acceleration, NEA) is plotted. It is calculated assuming the fundamental in-plane mechanical mode is dominantly driven by fundamental thermal noise Eq. (3). The spike near 35 kHz is again due to the fundamental out-of-plane mechanical mode.

the system has a round-trip efficiency of  $\eta_{rt}$ . Note that  $\sqrt{\eta_{rt}} = \eta_{cpl}$ , where  $\eta_{cpl}$  is the single-sided coupling efficiency. By adding up the infinite series of reflections in this system and choosing the appropriate round-trip phase change to maximize and minimize the reflected signal,  $R$ , we can arrive at the following expression for the visibility,  $V$ , of the fringes (assuming we're far from the photonic crystal resonance) [36, 39, 40].

$$V = \frac{R_{\max} - R_{\min}}{R_{\max} + R_{\min}} = \frac{2\sqrt{R_{\text{fib}}}(1 - R_{\text{fib}})\eta_{cpl}(1 - \eta_{cpl}^2)}{R_{\text{fib}} + \eta_{cpl}^2 + R_{\text{fib}}\eta_{cpl}^2(R_{\text{fib}} + \eta_{cpl}^2 - 4)} \quad (14)$$

The reflection coefficient of the cleaved fiber face is found in finite difference time domain (FDTD) simulations to be,  $R_{\text{fib}} = 0.035$  [39]. Using this parameter along with Eq. (14) and the measured visibilities in Fig. 13a allows us to back-out  $\eta_{cpl}$ . This coupling efficiency has been recorded as high as  $\eta_{cpl} = 0.746$  [36]. Typical values for our accelerometers were  $\eta_{cpl} = 0.5 - 0.6$ . For the particular device whose data is shown in Fig. 13a and Fig. 11, the efficiency was worse,



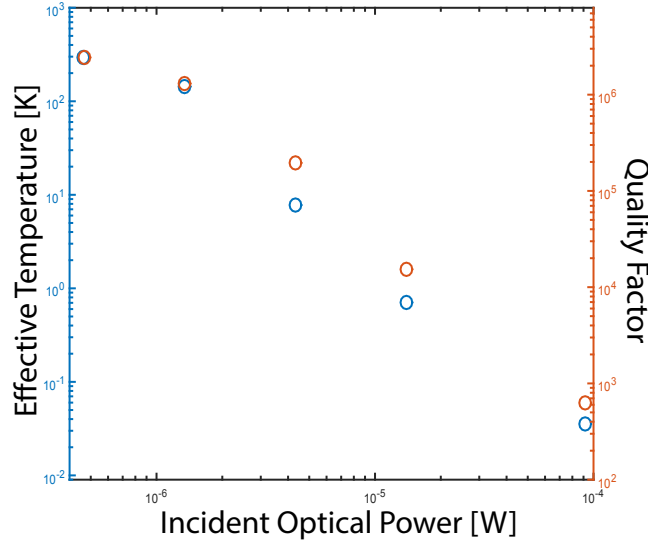


FIG. 12. **Damping and Cooling.** The effective mode temperature (blue circles) and mechanical quality factor (orange circles) of the fundamental in-plane mechanical mode with the laser locked half a linewidth red-detuned is plotted versus incident optical power in the optical fiber. The highest power shown corresponds to the optical power used in Fig. 11.

$\eta_{cpl} \cong 0.3$ . These losses in efficiency come from a number of sources some of which are more fundamental than others. The fundamental sources are the theoretical mode overlap between the optical fiber mode and the on-chip waveguide mode, the finite adiabatic tapering length of the on-chip waveguide, scattering from support tethers for the on-chip waveguide, and scattering during the adiabatic transition from the waveguide to the photonic crystal cavity. Together these more fundamental sources of loss limit the coupling efficiency to  $\eta_{cpl} \cong 0.86$  [36]. The remaining sources of loss are due to fabrication non-idealities. These include particulates on the on-chip waveguide, making the waveguide width (especially its tip) the wrong size, and misalignment of the optical fiber and on-chip waveguide due to over-etching the V-groove. Due to the finite etch-rate in the  $\langle 111 \rangle$  direction, the KOH etch of the V-groove must be carefully timed and temperature controlled.

## VII Capacitive Wavelength Tuning

When dealing with relatively fixed wavelength, on-chip laser sources and thermal drifts, it will be necessary to actively control the optical mode frequency of the OMA sensor. To this end, we investigated capacitive wavelength tuning of the zipper cavity optical resonance as part of the QuASAR program.

### A Working Principle of Capacitive Wavelength Tuning

The basic working principle behind capacitive wavelength tuning is quite simple. One side of a metal capacitor is placed on the rigid bulk of the chip. The other side is connected to a flexible side of the photonic crystal cavity. By applying a voltage, a capacitive force develops, which pulls the flexible side of the photonic crystal cavity away from the other. This increases the optical cavity slot gap and thereby changes the optical resonance frequency.

We can develop a simple mathematical model for this wavelength tuning method [37]. The simple geometry needed to understand this model is shown in Fig. 14. The energy stored in the

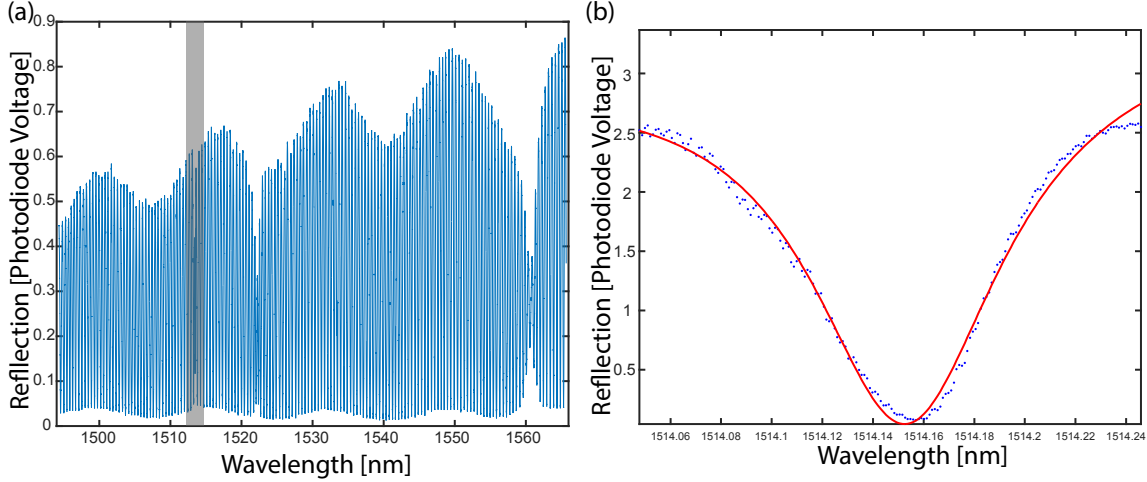


FIG. 13. **V-groove Fiber Coupled Optical Scans.** (a) This is a 1500-band reflection spectrum (unnormalized) of the V-groove fiber-coupled device under test. The series of sharp fringes are due to a parasitic Fabry-Pérot cavity as discussed in the main text. The optical mode of interest is highlighted in grey. (b) A zoom-in of the optical mode of interest is shown along with a Lorentzian fit (red). The fitted optical Q is  $Q_o = 16,500$ . (note that the scans in (a) and (b) were taken at different detector gain and optical power settings).

capacitor and the corresponding force are given by the following equations.

$$E_{\text{cap}} = \frac{1}{2} C(x) V_a^2 \quad (15)$$

$$F_{\text{cap}} = -\frac{dE}{dx} = -\frac{1}{2} V_a^2 \frac{dC(x)}{dx} \quad (16)$$

In Eqs. (15) and (16),  $V_a$  is the applied voltage across the capacitor,  $x$  is the position of the flexible side of the capacitor (see Fig. 14), and  $C(x)$  is the capacitance as a function of  $x$ . For a canonical parallel plate capacitor  $C(x) = \frac{A\epsilon_o}{(w_g - x)}$ , where  $A$  is the cross-sectional area of the plates and  $\epsilon_o$  is the permittivity of free space. For the on-chip capacitive wires we'll use, the parallel plate model isn't an accurate approximation because the wire thicknesses will be comparable to their separation and thus fringing fields will play a role. A realistic model for these on-chip wire capacitors including fringing effects is as follows.

$$C(x) = \frac{A\epsilon_o}{(w_g - x)^n} \quad (17)$$

In Eq. (17),  $n$  is some real number between 0 and 1. Typical parameter values for the wire capacitors in this work are  $C(0) \sim 1 \text{ fF}$  and  $n \cong 0.7$ , calculated by finite element simulation in Comsol [37]. Eq. (17) leads to the following capacitive force.

$$F_{\text{cap}}(x) = \frac{nA\epsilon_o V_a^2}{2(w_g - x)^{n+1}} \quad (18)$$

This capacitive force will be balanced by the elastic restoring force of the flexible side, characterized by an effective spring constant,  $k_{\text{eff}}$ .

$$F_{\text{spring}} = -k_{\text{eff}}x \quad (19)$$

By approximating Eq. (18) to zeroth order for  $x \ll w_g$  and equating it to Eq. (19), we arrive at the displacement caused by the capacitive force,  $\delta x$ .

$$\delta x = \frac{nA\epsilon_o V_a^2}{2k_{\text{eff}}w_g^{n+1}} \quad (20)$$

The corresponding wavelength shift of the optical mode is determined using the optomechanical coupling,  $g_{\text{OM}}$ .

$$\delta\lambda = \frac{g_{\text{OM}}}{2\pi} \frac{\lambda_o^2}{c} \delta x = \frac{g_{\text{OM}}}{2\pi} \frac{\lambda_o^2}{c} \frac{nA\epsilon_o V_a^2}{2k_{\text{eff}}w_g^{n+1}} \quad (21)$$

Therefore, the capacitive force leads to wavelength tuning that is proportional to  $V_a^2$  and  $w_g^{-(n+1)}$ , thus emphasizing the benefit of small capacitive wire gaps.

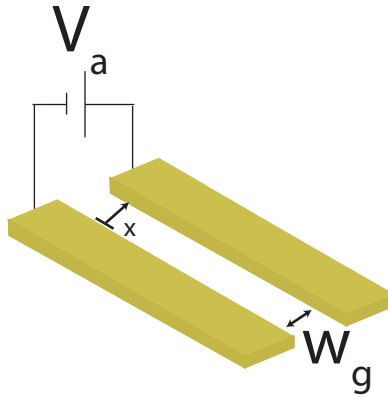


FIG. 14. **Simple Capacitor Geometry.** The two rectangles represent gold wires. The static gap between the wire is  $w_g$ . The applied voltage between the wires is  $V_a$ . The right wire is considered rigidly fixed, and the left wire is flexible with a position given by  $x$ .

## B On-Chip Capacitor Wire Fabrication

The metallized nanofabrication process for realizing on-chip capacitive actuation of the zipper cavity is presented in Fig. 15. The process flow begins identically to the standard process flow of the zipper cavity OMA. The first electron beam lithography step defines the capacitor wires along with a set of alignment markers in the electron beam resist. Metal is subsequently electron-beam deposited upon the developed resist pattern. Typically, we evaporate  $\sim 5$  nm of chromium and  $\sim 200$  nm of gold to create the wires. The thin chromium layer simply acts as an adhesion layer, helping the gold stick to the surface. As long as the metal layer is approximately less than half the e-beam resist thickness, dissolving the e-beam resist in heated solvent such as Acetone removes the metal layer along with it, except where the resist was patterned (see Fig. 15e). Subsequently, a new layer of e-beam resist is spun on the chip and second e-beam lithography step is performed. The gold alignment markers can be imaged through the resist, which allows precise alignment of the second lithography pattern to the first. In this case, the gap between the electrodes is precisely written and, subsequently, dry-etched through the silicon nitride layer (see Fig. 15f-h). Finally, the chip is cleaned in piranha solution, KOH released, piranha cleaned again, and critical-point-dried. We are left with a chip with sections of the silicon nitride layer released from the silicon backside (the flexible regions) with gold capacitor wires with narrow gaps on top.

## C Accelerometer Wavelength Tuning

Using the nanofabrication steps described above we fabricated devices that incorporated both straight-line fiber v-groove coupling and capacitive tuning. The devices and results are shown in Fig. 16. As is shown in detail in Fig. 16, one side of the zipper cavity is, of course, connected to the test mass. The other side, instead of being rigidly connected to the bulk, is suspended on a flexible beam. Note that this flexible suspension is still designed to be much stiffer than the in-plane test-mass mode such that relative motion of zipper beams due to in-plane acceleration is still dominated by the test-mass mode. This flexible support beam is metallized with the other side of the capacitor being placed on the rigid bulk. Because we were simply shooting for a proof-of-principle demonstration, the effort was not made to minimize the capacitor gap size and it was simply designed at  $1\ \mu\text{m}$ . The long length of the capacitor  $\approx 600\ \mu\text{m}$  compensated for this large gap to some degree. Nevertheless, Fig. 16b shows that we were able to achieve a substantial tuning of approximately 3.5 nm with an applied voltage of 15 V. Fabrication optimization could easily increase this tuning range by an order of magnitude.

## VIII Intel On-Chip Laser Testing

Practical use of our accelerometers in their V-groove coupled configuration without on-chip lasers is certainly possible. For example, oil fields on the ocean floor have been probed using arrays of optical accelerometers multiplexed into a remote tunable laser source [17]. These applications capitalize on light's ability to be transmitted over km scale distances with negligible loss. Nevertheless, the ultimate realization of our optomechanical accelerometer would be as a fully packaged and integrated sensor with both the laser source and photodetector on-chip. This would help make the accelerometer measurement system significantly cheaper and open up new applications such as, but certainly not limited to, guidance systems. To this end, we entered into a collaboration with Intel. Intel has developed and begun wafer-scale production of on-chip lasers and detectors based around a CMOS-compatible silicon process. The lasers, originally developed by John Bowers's group at UCSB, are shown in Fig. 17. They are electrically driven, multiple quantum well, separate confinement heterostructure, AlGaInAs-silicon evanescent lasers [38]. The III-V heterostructure is wafer bonded on top of the SOI wafer with the silicon waveguide defined. The silicon waveguide defines the laser cavity and 75% of the optical mode overlaps with the silicon waveguide while 3%

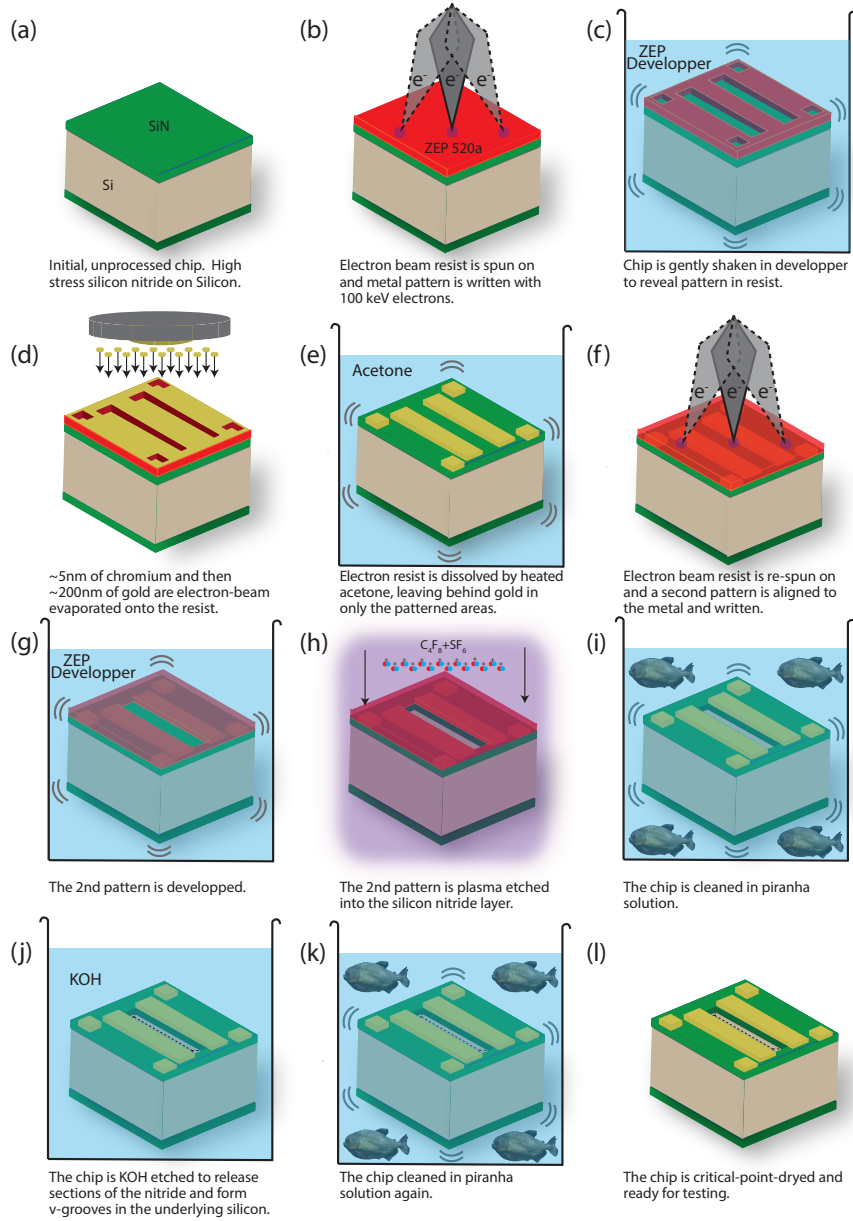
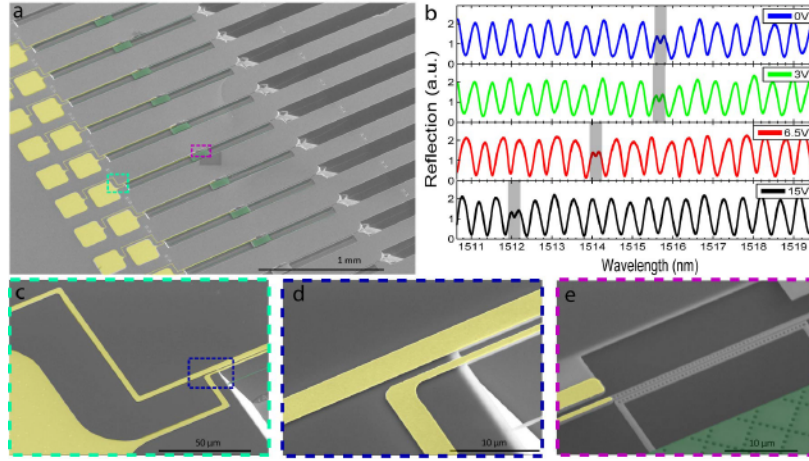


FIG. 15. Nano-fabrication process flow with metallization.

overlaps with the quantum well gain medium.

As previously stated, the ultimate goal would be to incorporate our accelerometer structures with Intel's laser chips. Several factors prevented this full integration route from being pursued during QuASAR. Firstly, our Intel collaborators lacked access to small test nanofabrication facilities necessary for an attempt to fabricate our devices on their wafers. Secondly, intellectual property concerns prevented Intel from allowing us to handle their chips in our cleanroom. Nevertheless, our Intel collaborators did visit our labs at Caltech and allowed us to couple light out of their laser chips for an important proof-of-principle experiment.

As shown in Figs. 8 and 11, our accelerometers have been able to achieve excellent accel-



**FIG. 16. Tunable Accelerometer.** (a) False color SEM showing a wide-field view of several capacitively tunable accelerometers. The gold metal is colored yellow and the large rectangles on the left hand side are the bond pads. The accelerometer test-masses are highlighted in solid green. A zoomed-in image of the regions demarcated by dashed colored rectangles will be shown in subsequent images (b) A series of laser reflection scans of a device. An optical mode is highlighted in grey and tracked as a function of voltage. The mode moves approximately 3.5 nm with 15 Volts applied. (c) A zoom-in of the dashed green rectangle in (a). This shows the edge of one bond pad and the wires running off of it. (d) A zoom-in of the blue dashed rectangle in (c). This shows the two wires running side by side as one wire (the thicker one on top) stays on the bulk of the chip and the other begins to run along the support beam of one side of the zipper cavity. (e) A zoom-in of the dashed magenta rectangle in (a). This shows the zipper cavity and the end of the wire capacitor. As one can clearly see, the bottom beam of the zipper cavity is connected to the accelerometer test-mass, while the top zipper beam is connected to a stiffer, yet flexible, support beam that is metallized, forming one side of a variable gap capacitor. By applying a voltage across these wires, the top zipper beam is pulled away from the bottom beam and the optical cavity frequency is changed (tuned).

eration resolution. However, this resolution has been achieved using expensive, table-top laser sources. Conceivably, Intel's on-chip lasers could have significantly worse noise properties, rendering sensitive optomechanical acceleration measurements impossible. Due to intellectual property concerns, Intel would not allow us to directly measure their lasers' amplitude or phase noise. However, they did allow us to measure the acceleration resolution of one of our devices using their laser.

For the experiment, we used one of our V-groove coupled accelerometers using the straight-line configuration shown in Fig. 10g. Intel's lasers operate in the 1300 nm band, so our zipper photonic crystals were redesigned so that their modes lay in this band. Light was coupled out of Intel's laser chip using an edge-coupling technique illustrated from topview in Fig. 17c and the actual experimental setup is shown in Fig. 17d. The laser chip is cleaved perpendicular to the silicon waveguide and, using a lensed optical fiber mounted on micrometer stages, the light emitted from the edge of the chip was collected. From there, the optical fiber was routed to a circulator, then glued into the on-chip fiber V-groove, then the reflected light was measured on a photodetector. The particular accelerometer chip tested did not have electrostatic tuning capability; however, several accelerometers were tested until one was found with an optical mode near the laser wavelength,



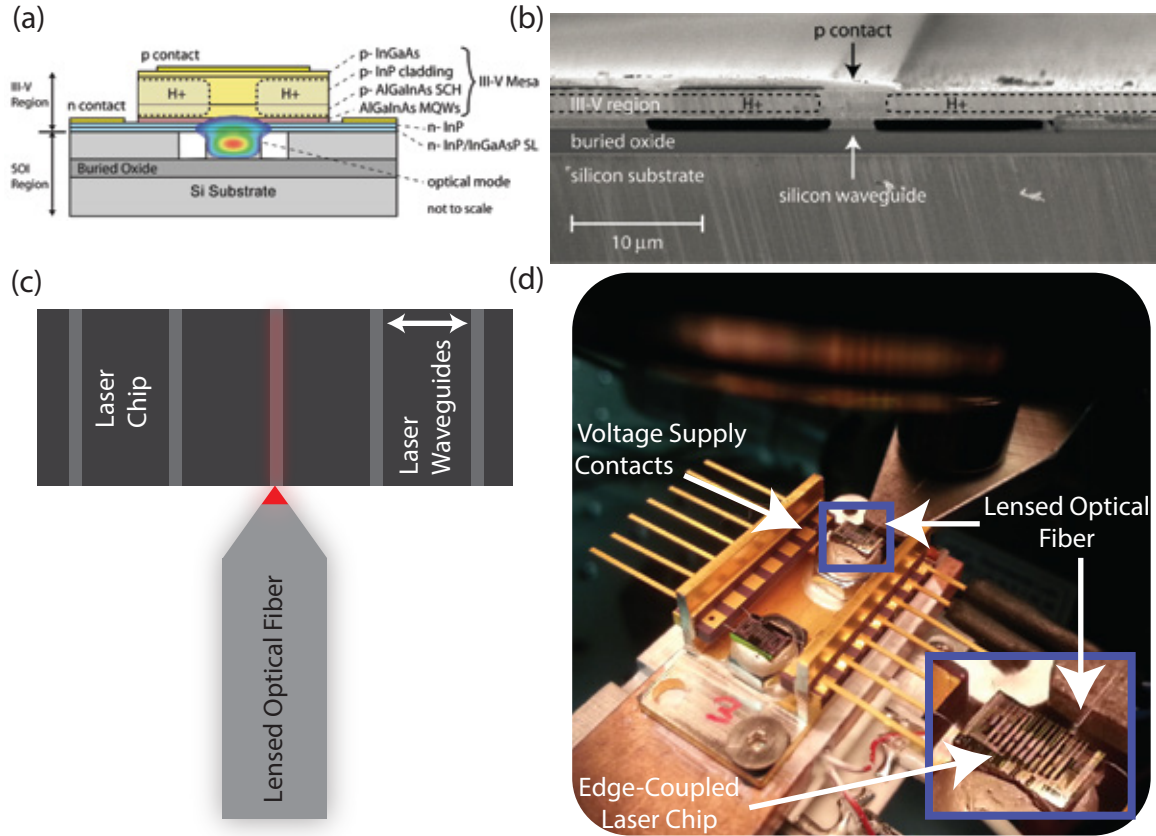


**FIG. 17. Intel On-Chip Laser Coupling.** (a) This is a schematic drawing of the layer structure of the hybrid III-V silicon laser used in this experiment. This image is reproduced from Ref. [38]. (b) This is an SEM cross-sectional image of a fabricated laser. This image is reproduced from Ref. [38]. (c) Cartoon of the lensed fiber technique used to gather the light emitted from the on-chip waveguides at the edge of the chip. (d) This is an optical image of the experimental setup. The laser chip is mounted on a temperature-controlled stage. The outer packaging provides voltage supply bond pads and pins so the electrical pump can be supplied to the on-chip lasers. A lensed optical fiber mounted on micrometer stages can be finely positioned to efficiently collect light that is edge-emitted from the on-chip waveguides.

1310 nm. From there, the modest thermal and current tuning capability of the on-chip laser was used to tune the laser approximately half a linewidth detuned from the optical resonance. The results of this acceleration resolution measurement are shown in Fig. 18. The data from Intel's on-chip laser is the blue curve and the data from our New Focus Velocity tunable external cavity diode laser is the red curve. The two curves were taken at the same laser power input to the optical cavity of 330  $\mu\text{W}$ , and the dashed lines of the same color are the corresponding laser shot noises for each experiment. There is discrepancy in the shot noise levels due to slightly different laser detunings for each experiment (achieving a precise detuning with the intel laser was difficult in our experimental setup). As can be seen in Fig. 18, the acceleration noise floors are limited primarily by shot noise and a low frequency noise roll-up (whose source we will investigate in the subsequent sections). Regardless, the two curves lie directly on top of each other, meaning Intel's on-chip lasers are capable of achieving comparable noise performance to our table-top lasers with

our accelerometers. This is an important proof of principle that shows excellent performance can be expected if our accelerometers are successfully integrated with Intel’s on-chip lasers.

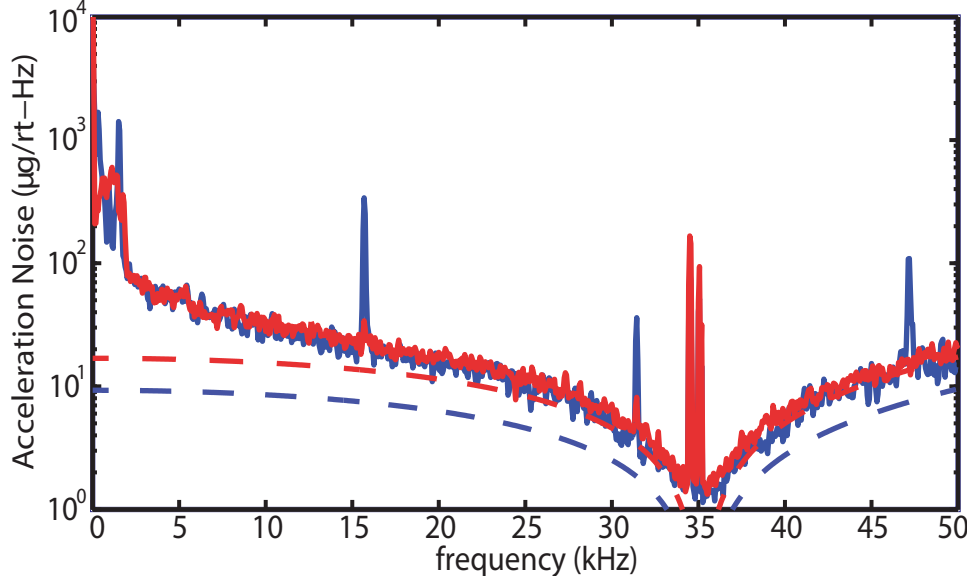


FIG. 18. **Intel Laser Acceleration Resolution.** The acceleration resolution of a V-groove coupled accelerometer using Intel’s on-chip laser (blue curve) and a New Focus velocity table-top laser (red curve). The dashed lines of the same color are the corresponding shot noise floors for each experiment. The low frequency rollup of the acceleration noise is present again, as it was in the inset Fig. 11. The source of this noise will be discussed in Section IX.

### IX Reduction of Low-Frequency Noise

In Section VI and Fig. 11, we noted the presence of a low-frequency noise increase, or “roll-up” in the noise, in the electronic PSD of our accelerometer. This is an important noise source because it dramatically limits the low frequency performance of our devices. It turns out this noise originates from fluctuations of the optical cavity frequency. In this section, we will characterize this noise, argue for its noise source, model it, and demonstrate several methods for eliminating it.

A close-up, log-log plot of the roll-up noise is shown in Fig. 19. The blue data is taken on an accelerometer device of the type shown in Fig. 26. The red data is taken on a “test” cavity which consists of a zipper cavity with no test mass and a very stiff mechanical clamping to eliminate mechanical motion. The PSDs for each curve are normalized by the optical transduction factor to make direct comparison meaningful. The roll-up noise follows an approximate  $\omega^{-1.5}$  frequency dependence until very low frequencies of 10-20 Hz (the black line in Fig. 19 is the fitted frequency slope which is -1.52). Moreover, to within a factor of two, the roll-up on the two devices is the same. As mentioned, the two mechanical structures of these devices are vastly different. The accelerometer structure has a fundamental resonance frequency at  $\sim 10$  kHz, and the test cavity’s fundamental mechanical frequency is  $\sim 10$  MHz. It is inconceivable, therefore, that the noise source could be mechanical or vibratory in nature.

It is also relatively simple to rule out classical laser noise as the source of the roll-up. By putting the output of our laser directly onto our photodetector we can see that the amplitude noise of our laser is shot noise limited at powers relevant to our experiment. This is neither the same



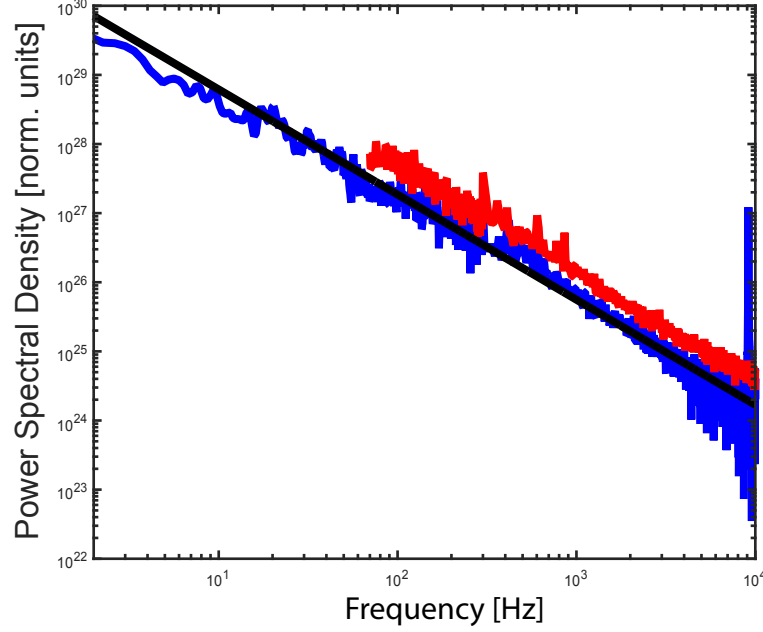


FIG. 19. **Roll-up Noise Characterization.** This is a log-log plot of the electronic power spectral density normalized by the optical transduction coefficient. The flat noise floor consisting of NEP and shot noise has been subtracted. The blue curve is data for an accelerometer of the same design as shown in Fig. 26. The red curve is data from a test optical zipper cavity without a test mass and a much stiffer mechanical clamping (resonance frequency around 10 MHz). The black line is a fitted slope to the blue data and its value is -1.52.

magnitude nor the same shape as the observed roll-up. Similarly, by putting our laser through a Mach-Zehnder interferometer and locking it to the side of a fringe (lock frequency  $< 100$  Hz), we can see the phase noise of the laser is neither the right magnitude nor the right shape.

Moreover, there is an elegant experiment we can do that simultaneously rules out mechanical motion and laser noise as the sources of the roll-up. The zipper optical cavity hosts a series of optical modes. Of interest here is the fundamental bonded and anti-bonded modes. If the source of the roll-up noise is common to both optical modes then by probing both modes at the same time and subtracting their response, the noise should be cancelled. If the noise is uncorrelated between the two optical modes then the cancellation scheme should be ineffective.

The experimental setup for this measurement is quite simple. Light from two separate lasers is sent to two respective attenuators to independently control their power. The two lasers are combined into a single fiber using a 50-50 coupler, which is then connected to port 1 of a circulator; port 2 of the circulator is connected to the device under test, while port 3 is connected to a de-multiplexer. Using the de-multiplexer the two laser frequencies can again be separated, with each laser sent through an optical switch to one of the ports of a balanced photodetector. The switches allow us to turn the cancellation on or off, by switching one of the lasers away from the detector. Using this experimental setup we set each laser approximately half a linewidth red-detuned, one from the fundamental bonded mode and the other from the fundamental anti-bonded mode. By fine tuning the optical power in each mode, the roll-ups were made to match each other in magnitude and then were subtracted on the balanced photodetector. The results of the experiment are shown

in Fig. 20.

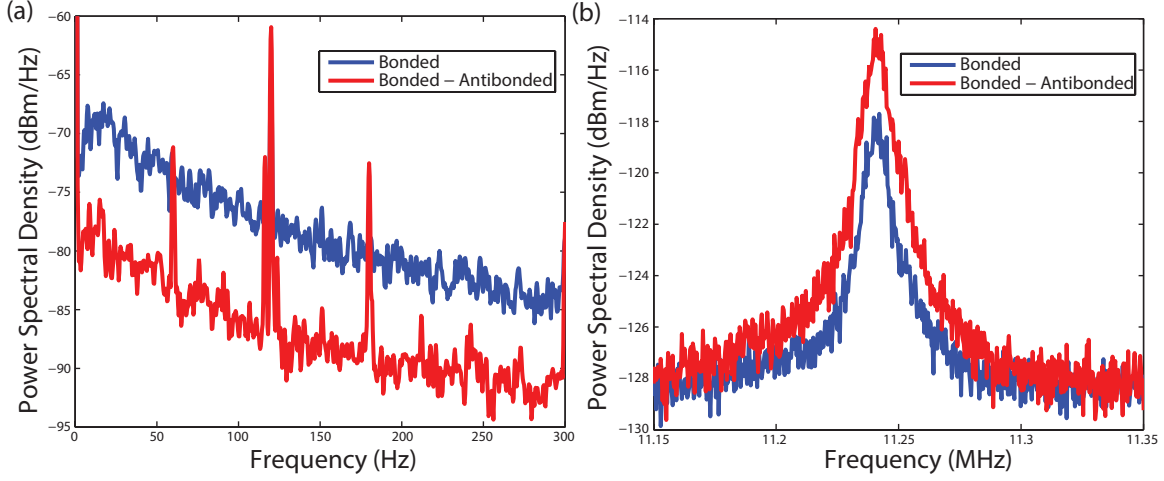


**FIG. 20. Roll-up Noise 2 Laser Cancellation.** (a) Shows the cancellation of the roll-up noise between 0 and 300 Hz. The blue data is obtained when only laser light reflected from the bonded optical mode hits the balanced photodetector. The red data is obtained when both light reflected from the bonded and anti-bonded modes hits the balanced photodetector and the signals are subtracted. (b) This data is the same as (a) except the frequency span is confined to a narrow band around the fundamental mechanical resonance. Note how subtraction of the bonded and antibonded modes leads to an increase in mechanical signal (this is discussed in the main text). Also note that this mechanical data was taken using a different balanced photodetector than the data in (a), so strict comparison of the y-axis is not meaningful.

As can be seen in Fig. 20a, the two laser cancellation scheme reduces the low-frequency roll-up noise by 9 dB. The two lasers used were independent of each other and, in fact, the laser cavities were located in different laboratories. Therefore, it is unreasonable to propose that their classical noise would be correlated and, thus, this cancellation shows that the source of the roll-up noise can not be classical laser noise. Additionally, in Fig. 20b, we see that when the two laser signals are subtracted the mechanical transduction actually increases by approximately 3.5 dB. This is because the bonded and anti-bonded optical modes, due to their different symmetry about the zipper slot gap, actually have optomechanical couplings,  $g_{OM}$ , that differ in sign. Thus, when the two lasers are subtracted (with the same sign for their detuning), mechanical motion is actually added together. This, in turn, implies the low frequency roll-up can not be mechanical motion.

If the roll-up is not caused by laser noise or mechanical motion, the remaining reasonable source is fluctuations of the optical cavity frequency. The roll-up does have a definite dependence on the laser's detuning from the optical resonance. That is, the noise disappears when the laser is directly on resonance with the optical cavity or very far-detuned (several linewidths). This is consistent with a noise source that causes frequency fluctuations of the optical cavity frequency.

There are several such noise sources for micro-resonators and the most common and best understood sources are described in great detail in Refs. [41, 42]. However, none of these well-understood noise sources accurately describes our noise source. Frequency noise from a Kerr nonlinearity, pondermotive fluctuations, and photothermal noise are not good descriptions because those transduced noises increase nonlinearly with optical power while our noise increases linearly. Thermo-elastic (sometimes called thermo-mechanical) noise involves temperature fluctua-

tions causing thermal expansion or mechanical vibrations of the cavity. We have already discussed that this can not be the source. Moreover, the expected frequency spectrum would look like the mechanical susceptibility and not the  $\omega^{-1.5}$  we observe. Elasto-optic noise involves temperature fluctuations, causing mechanical motion fluctuations which induce stress and thereby shift the optical resonance via the photoelastic effect [42]. For many reasons, elasto-optic noise is not a good description of the observed roll-up, the easiest reason for this is again it predicts the wrong frequency spectrum (it should follow the mechanical susceptibility). Moreover, the fundamental mechanical frequencies of these structures are  $\sim 10$  kHz for the accelerometer and  $\sim 10$  MHz for the test cavities, yet the roll-up has significant frequency dependence all the way down to at least the 1 Hz range. Finally, thermo-refractive noise, which is fluctuations of the refractive index due to fundamental temperature fluctuations, is also not a good model for our noise. The theoretical prediction for the magnitude of thermo-refractive fluctuations (see Refs. [41, 43]) is about a factor of 100 smaller than the magnitude of the roll-up we observe. Moreover, the frequency spectrum for thermo-refractive noise should be essentially flat below the frequency of the lowest thermal eigenmode [43]. Yet, we find that for the test cavity structure the lowest thermal eigenmode is  $\sim 2700$  Hz assuming a thermal conductivity of 3.2 W/mK [44, 45], and we still have significant frequency dependence of our roll-up at Hz-level frequencies.

### A Adsorbed Water Diffusion Model

If none of the well-known optical cavity frequency noise sources is a good description of our observed noise, we are left to develop an alternative reasonable explanation. In a paper from the Roukes group at Caltech on their nanomechanical mass sensors, mechanical frequency noise was observed and attributed to surface diffusion of adsorbates on their mechanical beams [46]. On our devices, as we'll discuss more later, we do expect the presence of adsorbed water molecules. In this section, we will develop a model for the effect the diffusion of adsorbed water molecules would have on the frequency of our optical cavities.

We will assume that these adsorbed water molecules primarily affect the optical frequency by changing the local refractive index. From Ref. [43], the relative shift of the optical frequency due to a index of refraction change  $\delta n$  is given by the following.

$$\frac{\delta\omega}{\omega_0} = -\frac{\int |\mathbf{E}_0|^2 \delta n dV}{\int n |\mathbf{E}_0|^2 dV} \quad (22)$$

In Eq. (22),  $n$  is the index of refraction of the photonic crystal,  $\mathbf{E}_0$  is the unperturbed optical mode of interest, and  $\delta n$  is the refractive index change induced by the adsorbed water molecules. For simplicity, we will model the photonic crystal beams and this system as a 1-dimensional problem. We will assume a fluctuating density per unit length of adsorbed water molecules on the surface of the beams given by  $C(x, t)$ . Using  $C(x, t)$ , we can rewrite Eq. (22) as follows.

$$\frac{\delta\omega}{\omega_0} = -V_{\text{water}} \frac{\int |\mathbf{E}_0(x, y_0, z_0)|^2 (n_{\text{water}} - 1) C(x, t) dx}{\int n |\mathbf{E}_0|^2 dV} \quad (23)$$

In Eq. (23),  $V_{\text{water}}$  is the volume of a water molecule,  $n_{\text{water}}$  is the index of refraction of water, and  $\mathbf{E}_0(x, y_0, z_0)$  is the value of the electric field at the surface of the beams. Note that the top integral in Eq. (23) will be broken into 8 parts, one for each surface of the two beams (many of them will be the same from symmetry). Simplifying Eq. (23) yields the following.

$$\frac{\delta\omega}{\omega_0} = A \int |\mathbf{E}_0(x, y_0, z_0)|^2 C(x, t) dx \quad (24)$$

$$A \equiv \frac{-(n_{\text{water}} - 1) V_{\text{water}}}{\int n |\mathbf{E}_0|^2 dV} \quad (25)$$

The subsequent derivation borrows heavily from Ref. [46]. Our ultimate goal will be to obtain the power spectral density of the optical frequency. The power spectral density of a variable is the Fourier transform of its autocorrelation, therefore our first step will be to calculate the autocorrelation,  $G(\tau)$ , of the frequency fluctuations:

$$G(\tau) = \frac{\langle \omega(t) \omega(t + \tau) \rangle}{\omega_0^2} = A^2 \int dx \int |\mathbf{E}_0(x, y_0, z_0)|^2 |\mathbf{E}_0(x', y_0, z_0)|^2 \langle C(x, t + \tau) C(x', t) \rangle dx' \quad (26)$$

In order to move forward with Eq. (26), we'll need to find  $\phi(x, x', t) \equiv \langle C(x, t + \tau) C(x', t) \rangle$ . We can do this by recognizing that  $C(x, t)$  must satisfy a diffusion equation as follows.

$$\frac{\partial C(x, t)}{\partial t} = D \frac{\partial^2 C(x, t)}{\partial x^2} \quad (27)$$

$$\frac{\partial C[k, t]}{\partial t} = -Dk^2 C[k, t] \quad (28)$$

$$C[k, t] = e^{-Dk^2 t} C[k, 0] \quad (29)$$

Between Eqs. (27) and (28), we performed a Fourier transform with respect to the x-coordinate and denoted this as,  $C[k, t]$ . Using Eq. (29), and standard Fourier transform results for Gaussians, we can find  $\phi(x, x', t)$ .

$$\phi(x, x', t) = \frac{N}{L} \frac{1}{2\sqrt{\pi D \tau}} e^{-\frac{(x-x')^2}{4D\tau}} \quad (30)$$

The normalization constant out in front in Eq. (30) contains N, the total number of adsorbed water molecules on the particular surface of the beam, and L, the relevant length of the beam (relevance set by optical mode size). In order to obtain a reasonable analytic expression for the integral in Eq. (26), we fit the optical mode to a gaussian on each surface of the beam.

$$|\mathbf{E}_0(x, y_0, z_0)|^2 = |\mathbf{E}_a|^2 e^{-\left(\frac{x}{L}\right)^2} \quad (31)$$

In Eq. (31),  $\mathbf{E}_a$  is the electric field amplitude for the gaussian fit and L is the fitted length scale for the optical mode (same L as the one found in Eq. (30)). Putting Eqs. (30) and (31) into Eq. (26) and performing the integral yields the following.

$$G(\tau) = |\mathbf{E}_a|^4 \frac{A^2 N \sqrt{\pi}}{\sqrt{2}} \frac{1}{\sqrt{1 + \frac{\tau}{\tau_D}}} \quad (32)$$

$$\tau_D \equiv \frac{L^2}{2D} \quad (33)$$

Now we are in a position to calculate the power spectral density for the relative optical frequency fluctuations,  $y = \frac{\delta\omega}{\omega_0}$ .

$$\begin{aligned} S_{yy} &= \int_{-\infty}^{\infty} G(\tau) e^{-i\omega\tau} d\tau = 2 |\mathbf{E}_a|^4 A^2 N \sqrt{\frac{\pi}{2}} \int_0^{\infty} \frac{\cos(\omega\tau)}{\sqrt{1 + \frac{\tau}{\tau_D}}} d\tau \\ &= \frac{|\mathbf{E}_a|^4 A^2 N \pi \tau_D}{\sqrt{\omega \tau_D}} (\cos(\omega \tau_D) + \sin(\omega \tau_D) - 2C_1(\sqrt{\omega \tau_D}) \cos(\omega \tau_D) - 2S_1(\sqrt{\omega \tau_D}) \sin(\omega \tau_D)) \end{aligned} \quad (34)$$

In Eq. (34),  $C_1$  and  $S_1$  are the first Fresnel cosine function and the first Fresnel sine function, respectively. Once again, there will be 8 contributions of Eq. (34) to the total noise, one for each surface of the optical beams. The gaussian fit to the optical mode along the top surface of the optical beam is shown in Fig. 21. The value of the norm-squared of the electric field was found in COMSOL simulation in the middle between consecutive holes (black circles in Fig. 21a) and fit to a gaussian (red line in Fig. 21a). The fitted gaussian width, parameterized by  $L$  in Eq. (31), is  $2.35 \mu m$  and the fitted magnitude is  $|\mathbf{E}_a| = 1.06 \times 10^8 \frac{V}{m}$ . The gaussian fits for the other sides of the optical beam were very similar.

The remaining parameters needed in Eq. (34) are the number of adsorbed water molecules,  $N$ , and the diffusion coefficient,  $D$  (note that  $D$  determines  $\tau_D$  through Eq. (33)). Silicon nitride, when exposed to the oxidizing piranha solution [47] or simply ambient air [48], will oxidize forming a thin layer of silicon dioxide. From Refs. [49–51], silicon dioxide is hydrophilic because water easily hydrogen bonds to surface hydroxyl (OH) groups. Furthermore, at room temperature silicon dioxide will develop approximately 2-4 monolayers of water when exposed to atmosphere with relative humidity between 20% and 70% [49]. The surface diffusion coefficient,  $D$ , for water on a hydrophilic silicon dioxide surface can be modeled using molecular dynamics simulations [51]. The lateral (in-plane) diffusion coefficient is found to be between  $0.99 \times 10^{-9} \frac{m^2}{s}$  and  $1.18 \times 10^{-9} \frac{m^2}{s}$  for the first monolayer, between  $2.18 \times 10^{-9} \frac{m^2}{s}$  and  $2.34 \times 10^{-9} \frac{m^2}{s}$  for the second monolayer, and approximately  $3 \times 10^{-9} \frac{m^2}{s}$  for the remaining bulk water layers. These numbers give us a great idea of the reasonable values for the diffusion coefficient and the number of monolayers of water on our structures.

Briefly, before proceeding further with fitting our measured roll-up noise to the form in Eq. (34), we note that the molecular dynamics simulation results for the diffusion coefficient do not account for interactions with air molecules at atmospheric pressure. Therefore, we'll fit using data taken at vacuum pressure ( $\sim 1 \times 10^{-5}$  mbar). The character of the roll-up noise does change slightly in vacuum versus atmospheric pressure and a comparison plot is shown in Fig. 22.

Fig. 23 shows the best fit (using least squares optimization) of Eq. (34) (including the contributions from all 8 surfaces) to the low-frequency roll-up noise measured on the fundamental bonded

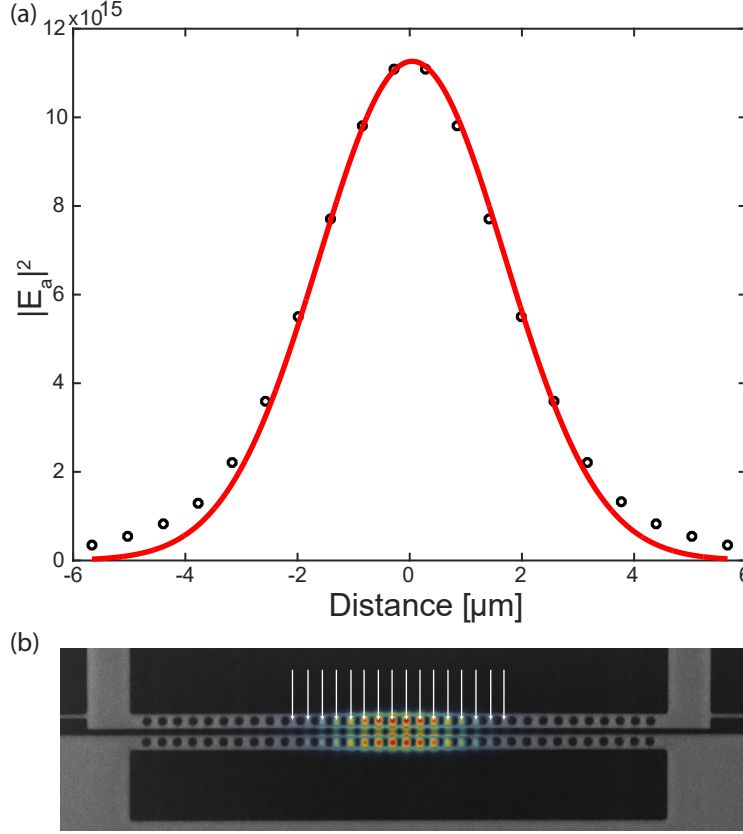


FIG. 21. **Optical Mode Gaussian Fit.** (a) Gaussian fit to the norm-squared of the fundamental bonded optical mode. The black circles are the value of the norm-squared electric field at the top surface of the optical beam at the middle point between optical holes (see white arrows in (b)). The red line is the gaussian fit with fitted width,  $L$  (see Eq. (31)), of approximately  $2.35 \mu m$ . (b) Plot of the norm of the electric field overlayed on the optical beams. The white arrows indicate the points where the electric field was sampled on the top surface for the gaussian fit.

mode of a zipper optical cavity in vacuum, with no proof mass and a stiff clamping. As one can readily see, the fit is excellent. As discussed earlier, there are really only two fit parameters: the number of water molecules (or equivalently the number of water monolayers) and the surface diffusion coefficient. The best fit shown in Fig. 23 occurs when  $D = 1.3 \times 10^{-9} \frac{m^2}{s}$  and the number of monolayers is 2.3. As discussed previously, this is in very good agreement with the values expected from the literature [49, 51].

### B Removing Diffusion Noise Through Surface Treatment

As shown in Fig. 23, the adsorbed water diffusion model (Eq. (34)) appears to predict the low frequency roll-up very well. Nevertheless, an experiment on a device with a reduced amount of adsorbed water, which showed a reduction in this noise would increase our confidence in the model. The water layers cannot be removed simply by going to vacuum (as is consistent with our data) and instead have to be subjected to a bake-out procedure much like ultra high vacuum systems [52]. However, we decided to implement a more permanent solution by using a surface treatment of the silicon nitride devices that makes them highly hydrophobic and, thereby, less susceptible to water

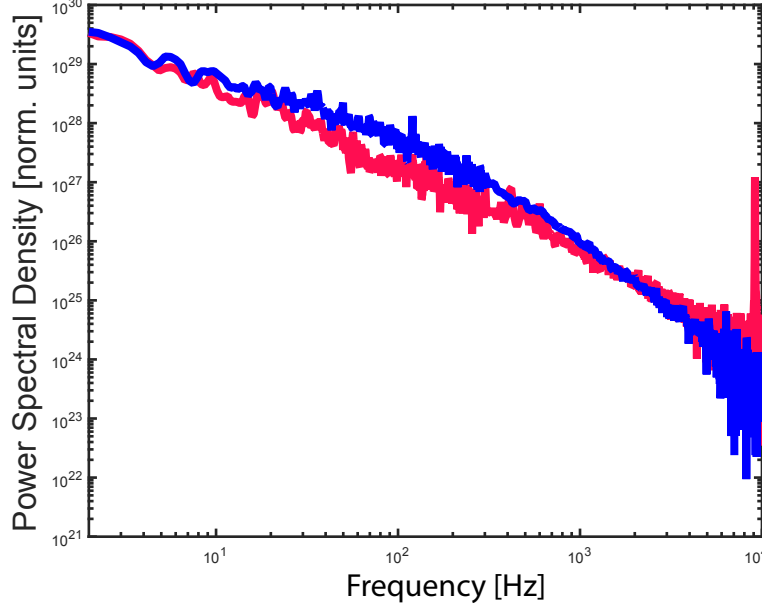


FIG. 22. **Compare Roll-Up Noise in Vacuum and Atmospheric Pressure.** This is a log-log plot of the electronic power spectral density normalized by the optical transduction coefficient (see discussion of Fig. 19). The flat noise floor consisting of NEP and shot noise has been subtracted. The blue curve is data taken in vacuum ( $\sim 1 \times 10^{-5}$  mbar) and the red curve is data taken atmospheric pressure.

adsorption. Both theoretical Monte Carlo simulations and experimental work have shown the lack of water adsorption on hydrophobic surfaces [52, 53].

The main idea is to conformally cover our released structures with a hydrophobic monolayer of material that takes the place of the water monolayers. Furthermore, this hydrophobic monolayer should be rigidly (covalently) bonded to the surface to prevent its own diffusion like the hydrogen bonded water molecules.

More specifically, we used alkyltrichlorosilane based self-assembled monolayer (SAM) techniques that are excellently described in Refs. [47, 54–57]. Broadly speaking, this SAM method works as follows. The alkyl-trichlorosilane ( $\text{RSiCl}_3$ ) precursor molecules (R is a hydrocarbon chain and  $\text{SiCl}_3$  is trichlorosilane) are placed in a suitable solution with the oxidized chip. The trichlorosilane head groups hydrolyze into three silanols ( $\text{SiOH}$ ), if the solution used is anhydrous this occurs at the water layer on the device surface. These silanols then condense with both hydroxyl groups on the oxidized device surface and silanol groups on other precursor molecules. These reactions replace the water layer with an extremely hydrophobic monolayer of covalently bonded siloxane ( $\text{Si-O-Si}$ ) crosslinks, see Fig. 24 adapted from Ref. [54].

The fabrication of our devices with SAM coatings is done following exactly the steps as for the zipper cavity OMAs, except before the final critical-point drying step the processes in table I is performed. The SAM coating is formed from 1H, 1H, 2H, 2H-perfluorodecyltrichlorosilane (FDTS). The FDTS mixture mentioned in table I is a 1 mM (milliMolar) solution of FDTS in anhydrous iso-octane. The entire SAM process technique is taken Ref. [57], with a slight modification to the hydrofluoric acid (HF) dip step. In Ref. [57], the HF dip step is used to undercut a sacrificial layer, which is not necessary here. In order to deviate as minimally as possible from the prescribed

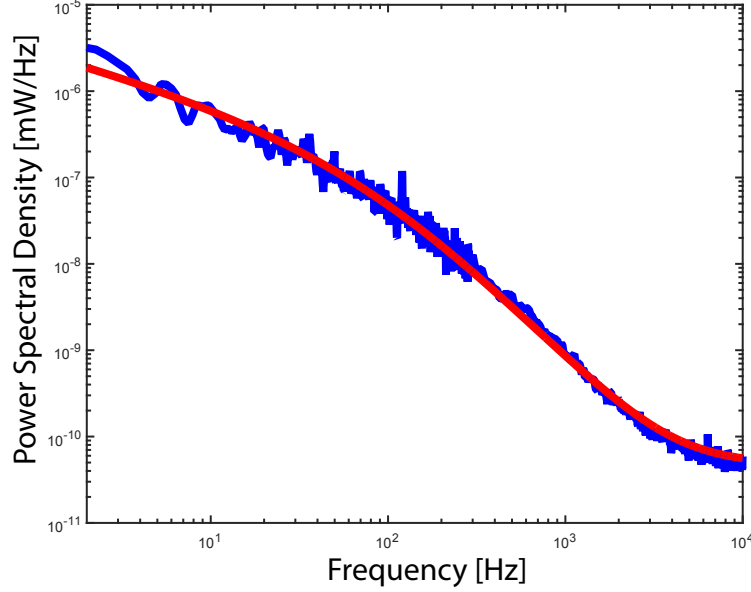


FIG. 23. **Adsorbed Water Diffusion Model Fit.** The blue curve is the electronic power spectral density of light reflected approximately half a linewidth red-detuned from the fundamental bonded optical mode of a zipper resonant cavity, at a vacuum pressure of  $1 \times 10^{-5}$  mbar. The flat noise floor consisting of NEP and shot noise has not been subtracted. The red curve is the best fit of this data to Eq. (34). The best fit has  $D = 1.3 \times 10^{-9} \frac{\text{m}^2}{\text{s}}$  and 2.3 monolayers of water.

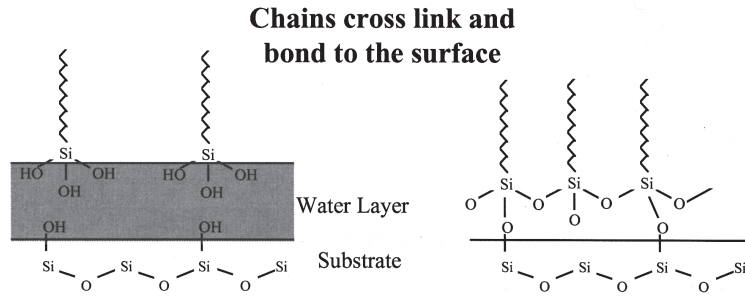


FIG. 24. **SAM Siloxane Crosslinking.** This figure illustrates the silanols from the precursor molecules reacting with surface hydroxyl groups to form a crosslinked siloxane layer as discussed in the main text. This figure is adapted from Ref. [54].

process, we incorporated a short, low concentration, HF dip, which Ref. [58] states may slightly increase  $Q_m$  by removing the thin top layer of nitride that may have been damaged by the dry etch. During all steps and rinses the chip was carried in a teflon holder to avoid deleterious surface tension forces. Also, we note that the critical-point dry step in table I may well be unnecessary, but we included it as a precaution. Because the water does not wet the SAM coated nitride surface, the devices can be simply lifted out of the last rinse step without fear of stiction for they will be dry. In fact, this SAM procedure reduces the work of adhesion by approximately four orders of



magnitude when compared to the standard oxide coating [55, 57]. Therefore, the SAM coating, from our point of view, doubles as a useful fabrication technique for low-frequency mechanical structures (in fact, this is the real reason why they were developed).

SAM Process Sequence		Approximate Time
Surface Preparation Step	1:10 HF to H <sub>2</sub> O Dip	1.5 min.
Surface Oxidization	H <sub>2</sub> O Rinse	10 min.
	H <sub>2</sub> O <sub>2</sub> Rinse	15 min.
	H <sub>2</sub> O Rinse	5 min.
SAM Formation	Isopropanol Rinse	5 min.
	Iso-octane Rinse	5 min.
	Iso-octane Rinse	5 min.
	FDTS mixture	10 min.
	Iso-octane Rinse	5 min.
	Iso-octane Rinse	5 min.
	Isopropanol Rinse	5 min.
Rinse and Dry	Isopropanol Rinse	5 min.
	H <sub>2</sub> O Rinse	5 min.
	Critical-Point Dry	

TABLE I. **SAM Procedure.** Procedure taken from Ref. [57].

Finally, in Fig. 25 we show the result of coating our structures with this SAM layer. Both data sets (red and blue) are taken on the same optical mode and device at atmospheric pressure. The red data was taken before the device was coated with the SAM layer and the blue data afterward. As one can readily see, there is a dramatic 15 dB reduction in the low-frequency roll-up noise. This adds another excellent piece of evidence that the low-frequency noise is really due to adsorbed water diffusion on the surface of the optical beams.

Note there is still low-frequency noise remaining after SAM treatment. This could be due to step imperfections in the SAM layer, which can act as sites for water adsorption and can lead to water surface coverage of approximately 10% [59]. Water on hydrophobic SAM layers does not form a uniform layer but instead forms microspheres (much like what happens on the macro-scale) [59, 60]. Perhaps these sources could be mitigated by refining our techniques for the SAM coating process. Ref. [56] states that the FDTS mixture and coating step may be improved by using a nitrogen dry box (to avoid contact with moisture in the air) and that was not done in this work. Additionally, the two laser cancellation scheme could be used to provide further cancellation. As it currently stands we have a very good understanding of the noise source and the 15 dB suppression will provide nearly a factor of 6 improvement in acceleration resolution.

## X Heavy Mass Accelerometers

A further improvement to the performance and practicality of the accelerometer can be achieved by greatly increasing the test mass size. By releasing entire sections of the 200  $\mu m$  thick chip, the test mass size can be increased by a factor greater than 10,000. This significantly reduces the fundamental acceleration thermal noise, Eq. (3). Furthermore, it allows the use of a lower mechanical quality factor while still achieving excellent thermal noise resolution. This means devices can be operated at room (atmospheric) pressure, which alleviates long-term low pressure packaging complications. Additionally, risk of failure due to resonant response from a large, broadband, shock input is greatly reduced when using lower mechanical Q.

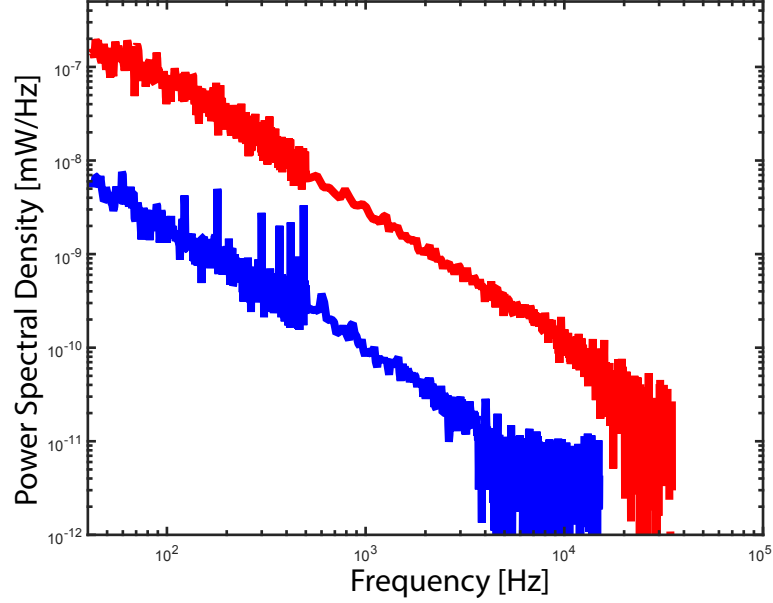
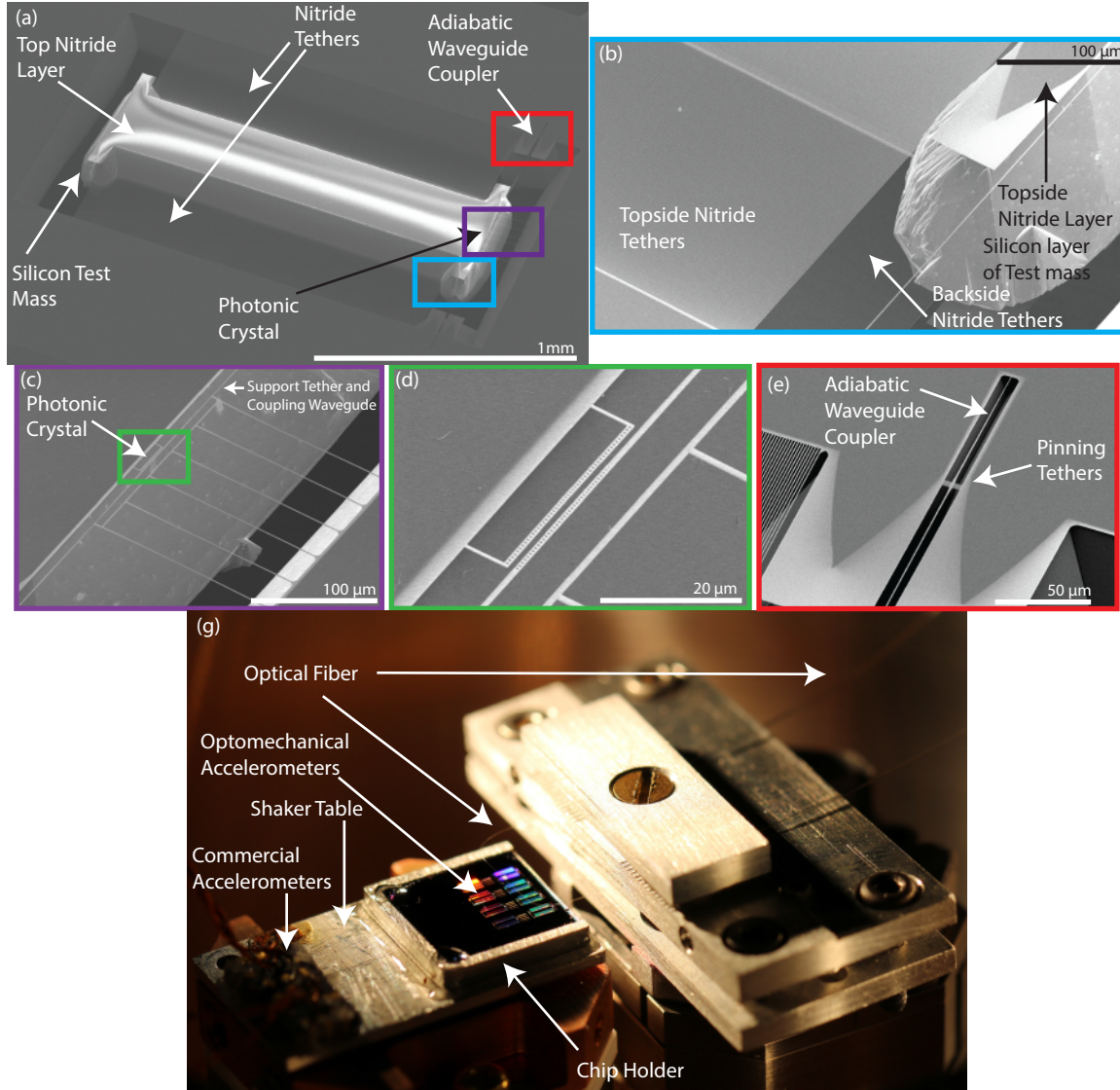


FIG. 25. **SAM Suppression of Low-Frequency Roll-Up.** This is a plot of the electronic power spectral density of light reflected approximately half a linewidth red-detuned from fundamental bonded mode of a zipper optical cavity. The flat noise floor consisting of NEP and shot noise has been subtracted. The red curve is taken before SAM coating and the blue curve afterward. The blue curve is adjusted by approximately 0.1 dB to account for changes in the optical transduction coefficient between experiments. Both data sets are taken at atmospheric pressure. The dB difference between the two curves is 15 dB.

The fabrication techniques used to release entire sections of the chip are not fundamentally different from those used for our single-sided lithography. The same test mass and nanostring pattern is written on the top and bottom side of the chip. If the patterns are well-aligned and the openings etched in the silicon nitride are wide enough, the KOH+IPA liquid etch can etch all the way through the chip. Moreover, due to the anisotropic nature of the KOH etch, the silicon underneath the rectangular test mass defined in the nitride layer remains (see Fig. 26). Again, we should note that these fully released devices are floppy and the  $\sim 200$  nm photonic crystal slot gaps are liable to collapse during fabrication if great care is not taken. As such, during all wet etches and rinses the samples must not be lifted out of liquid or else surface tension will cause collapse. These techniques are described in great detail in Ref. [61]. Also, the device studied in this section has been coated in a SAM layer as described in Section IX B to reduce the low-frequency roll-up.

Scanning electron microscope (SEM) images of an example heavy mass accelerometer are shown in Fig. 26. It is essentially the same as our initial accelerometer design (shown in Fig. 3) except at a much larger scale. That is, a rectangular test mass with a photonic crystal on one side. This time, however, there are several thousand tethers to maintain frequencies of  $\sim 10$  kHz with this much larger test mass (see Section V for our first discussion of this technique). Light is coupled into the photonic crystal using the adiabatic on-chip waveguide (see Fig. 26a,e). The adiabatic coupler is placed at a point after the coupling waveguide has been pinned to the bulk (Fig. 26e) to help mitigate the presence of taper modes, although, as we'll see, their effect is not completely eliminated. If the fiber taper is placed on the coupling waveguide before it is pinned to the bulk,

taper motion can cause motion of the waveguide and the taper modes are much more pronounced.



**FIG. 26. Heavy Mass Accelerometer.** (a) SEM image showing a heavy mass accelerometer. The large rectangle in the middle is the test mass, which is supported by  $\sim 3000$  nanostring tethers. The photonic crystal cavity is located on the right hand side (purple rectangle). Light enters the cavity via an adiabatic coupler and on-chip waveguide (red rectangle). The small rectangles added to the corners of the test mass and where the adiabatic waveguide is pinned to the bulk protect those regions from the KOH etching of convex corners. (b) This is a zoom-in of the side of the test mass (cyan rectangle in (a)). Here one can see individual nanostring tethers on both the topside and backside and the silicon layer of the test mass. (c) Zoom-in of the photonic crystal region. One side is attached to the test mass while the other side is attached to the bulk via a long parallel tether (which doubles as an input waveguide) and several perpendicular tethers. (d) Further zoom-in of the photonic crystal. Here one can resolve that the cavity is end-coupled to the input waveguide. (e) zoom-in of the adiabatic on-chip waveguide coupling region. (g) Optical image of the test setup.

### A Testing at Atmospheric Pressure

This heavy mass accelerometer was first characterized at atmospheric pressure in order to highlight its excellent acceleration resolution at these high pressures. Data characterizing the device, including an electronic power spectral density of the reflected laser light, is shown in Fig. 27. The optical mode used was the fundamental bonded mode and its quality factor was  $Q_o = 9600$ , as shown in Fig. 27c. The mechanical quality factor at air pressure was found by fitting the power spectral density to be  $Q_m = 5500$ , as shown in Fig. 27d. The electronic power spectral densities shown in Fig. 27a-b, were obtained from the photodetector signal of laser light reflected from the optical cavity with the laser approximately half a linewidth red-detuned from the optical cavity. Both Fig. 27a and Fig. 27b plot the same electronic power spectral density, but the difference is (a) uses linear axes while (b) is plotted on a logarithmic scale. Using the fiber taper and on-chip adiabatic waveguide end-coupled into the photonic crystal, the total detection efficiency of light in the cavity to the detector was  $\eta_{tot} \cong 0.24$ . The optical power used at the photonic crystal cavity was  $P = 12.4 \mu W$ , limited by a thermo-optic bistability [62]. Using these optical loss and power calibrations, and assuming the main mechanical peak in Fig. 27a is driven by room-temperature thermal noise (an assumption which will be validated later), we can fit an optomechanical coupling to this mechanical mode of  $g_{OM} = 2\pi \times 10 \frac{GHz}{nm}$ .

In Fig. 27a-b, the noise contributions of shot noise, detector NEP, and intrinsic mechanical thermal noise are shown. However, these cannot account for the mostly noise floor seen best in Fig. 27a. The cause of this noise floor is a rather simple and tractable one: it is the result of extraneous mechanical modes of the “stiff” side of the photonic crystal cavity, which are shown in the inset of Fig. 27a. The “stiff” side of the photonic crystal cavity is best illustrated in Fig. 26a,c,d. One side of the zipper cavity is attached to test-mass whose fundamental frequency is  $\omega_m \cong 2\pi \times 11.48 \text{ kHz}$ . The other side is tethered to the bulk in such a way that KOH etchant can get through to release the test-mass, yet its mechanical frequencies are still much greater than that of the test-mass  $\omega_m \gtrsim 100 \text{ kHz}$  (see inset of Fig. 27a). As the fundamental frequencies of the “stiff” side are at least 10 times greater than the fundamental frequency of the test-mass, this means the “stiff” side’s response to applied in-plane accelerations will be at least 100 times less than that of the test-mass. Therefore, the response of our entire accelerometer structure is dominated by the response of the test-mass and accelerations are efficiently sensed. If both sides of the photonic crystal had the same mechanical resonance frequency, their DC response to applied accelerations would be the same and no relative motion could be sensed. Even though the “stiff” side was correctly engineered to have much higher frequency modes, the combination of the much lower mass and much lower room-pressure  $Q$ ’s of these modes causes their thermal noise to be pushed above our other noise sources in Fig. 27a. As shown below, however, by going to vacuum the mechanical  $Q$ ’s of these modes will greatly increase and, consequently, their thermal noise will decrease and become negligible.

The acceleration resolution of the heavy mass accelerometer at room pressure is shown in Fig. 28. To measure the acceleration resolution the device was mounted on a shear piezo “shake table” just as shown Fig. 4 and Fig. 26g. As one can see in Fig. 28, we utilized two different ways to calibrate the acceleration resolution of this device and they agree extremely well above  $\sim 500 \text{ Hz}$  and diverge below that frequency. The “driven response” calibration simply involves shaking (driving) the device with a tone (whose strength is calibrated by commercial accelerometers) at each frequency, measuring the response, and comparing that to the noise spectrum. In other words, it is the same measurement technique as that used for Fig. 8b. The “assumed response” calibration involves shaking the device with a calibrated tone at one frequency where the test-mass response is known to dominate, i.e. very near the fundamental in-plane resonance frequency of the

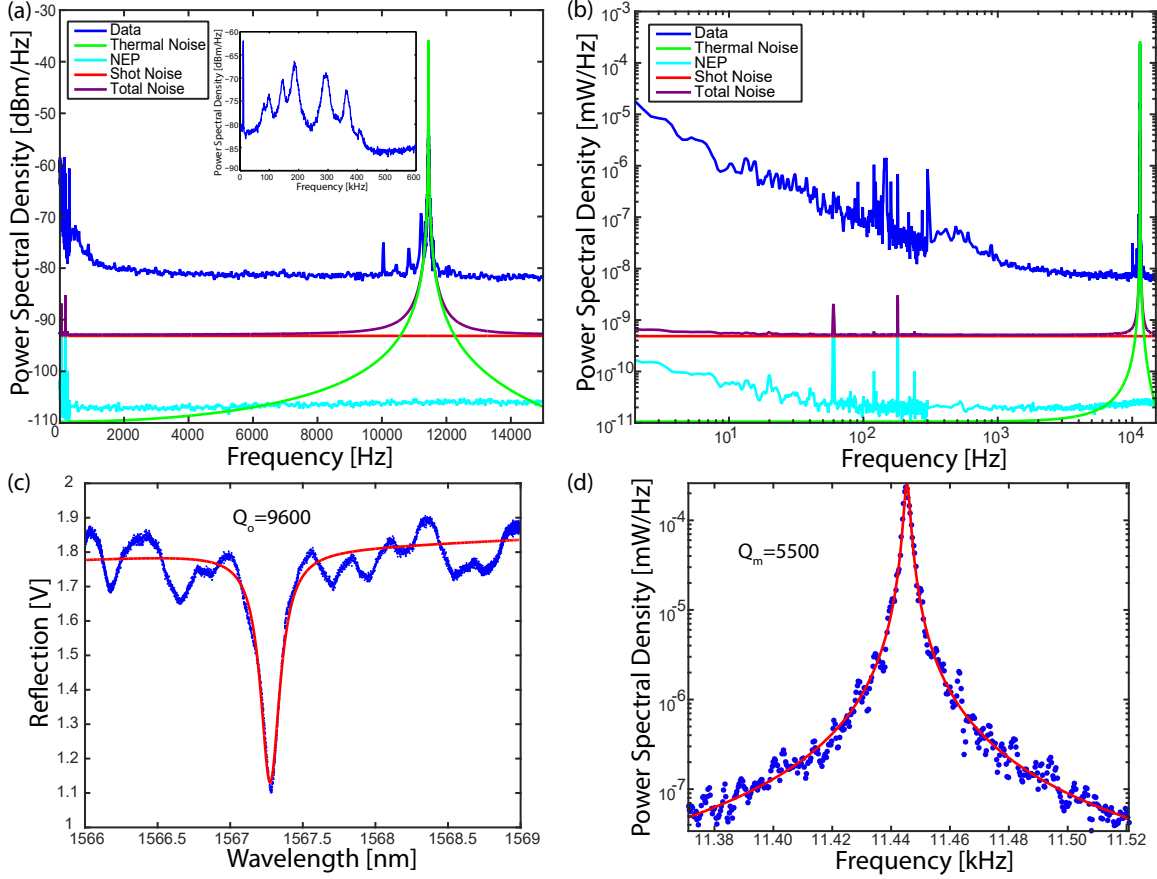


**FIG. 27. Heavy Mass Accelerometer Room Pressure Characterization.** (a) Electronic power spectral density of laser light reflected from the optical cavity with the laser approximately half a linewidth red-detuned from the optical resonance. The noise floor is set by the “DC” tail of mechanical modes of the “rigid” side of the optical cavity. inset: electronic PSD showing the “rigid” side mechanical modes. (b) same as (a) except with logarithmic scaling on both axes. (c) The un-normalized reflected laser light at the photodetector is shown in blue. In red is the fit of the optical resonance to a lorentzian lineshape with a  $Q_o = 9600$ . (d) A zoom-in of the electronic PSD centered around the main mechanical resonance is shown in blue. In red, a theoretical fit to the mechanical resonance showing a  $Q_m = 5500$ .

test-mass. This calibrates the acceleration noise of the mechanical mode in Fig. 27a, and then the standard mechanical response is assumed for all other frequencies. In other words, the “assumed response” method involves calibrating the acceleration noise of the green mechanical response curve in Fig. 27a-b and then using the signal-to-noise ratio of the measured power spectral density and the green mechanical response curve to obtain the broadband acceleration resolution of the device. The result of applying these calibration techniques are shown in Fig. 28.

Both of these methods obviously agree at the mechanical resonance, the lowest point on both resolution curves, with a resolution of  $\approx 100 \frac{\text{nano-g}}{\sqrt{\text{Hz}}}$ . This agrees very well with theoretical thermal acceleration noise, Eq. (3),  $a_{\text{th}} = \sqrt{\frac{4k_B T \omega_m}{m Q_m}} \cong 92 \frac{\text{nano-g}}{\sqrt{\text{Hz}}}$ . Here we have used  $\omega_m = 2\pi \times 11.48 \text{ kHz}$ ,  $Q_m = 5500$ ,  $T = 300 \text{ K}$ , and  $m = 267 \text{ nano-Kg}$ . The mass was calculated using the well-known

density of silicon and the physical dimensions of the test mass as shown in Fig. 26a. This confirms, once again, that the mechanical motion observed in our measured electronic PSDs is indeed due to room-temperature thermal noise of the fundamental in-plane mechanical mode of the test mass.

These two methods obviously diverge at frequencies below  $\sim 500$  Hz. This is due to a low-lying resonance of the fiber taper. This low-lying taper mode causes a spurious increase in response at low frequencies and a corresponding decrease in the noise equivalent acceleration, as was also observed previously in Fig. 8. Such a low-lying taper mode is again observed when testing this heavy-mass accelerometer as shown in Fig. 29, where the driven response is shown normalized by the strength of the drive. The red curve in this figure shows the expected response due solely to the fundamental in-plane mechanical mode of the test mass. This is a good fit to the measured response curve until  $\approx 500$  Hz, where the response rises like  $\omega^{-1.7}$ . This is reasonably close to the  $\omega^{-2}$  behavior we'd expect if approaching a low-lying mechanical resonance. Furthermore, this behavior is observed even if the laser is far-detuned from the optical cavity (inset of Fig. 29) and an increase in response is not observed on the commercial accelerometers. All of this evidence taken together makes us confident this spurious increased response at low frequency is due to a low-frequency taper mode. Therefore, for low frequencies, we rely on the “assumed response” calibration shown in Fig. 28.

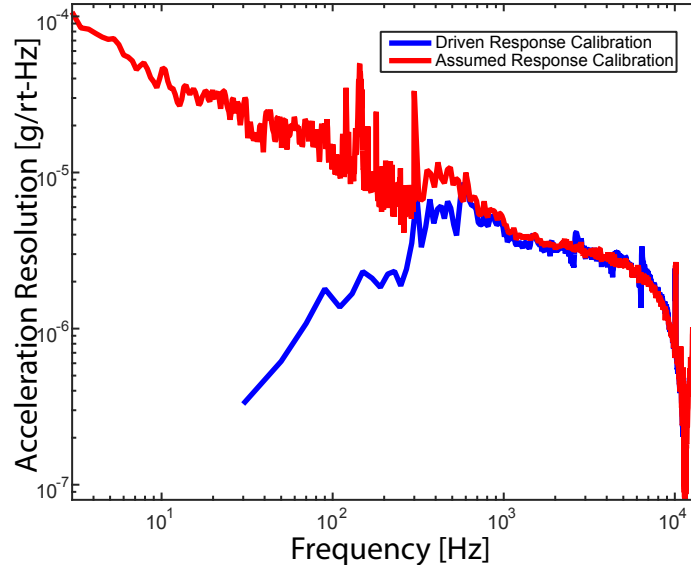


FIG. 28. **Heavy Mass Accelerometer Room Pressure Resolution.** Plotted here is the acceleration resolution (or, noise equivalent acceleration) of the heavy-mass accelerometer at atmospheric (air) pressure. A description of the two techniques used to calibrate the resolution, “driven response” and “assumed response”, can be found in the main text.

## B Testing in Vacuum

These measurements were repeated in vacuum (pressure  $\approx 10^{-5}$  mbar), in order to eliminate the relevance of the mechanical modes of the “stiff” side of the optical cavity. The electronic PSD of the measurement is shown in Fig. 30, again with (a) plotted on a linear scale and (b) on a log-log scale. It must be noted that this vacuum data was taken with 8 dB less optical power incident at the optical cavity than the room pressure data. This, again, is due to the thermo-optic bistability.



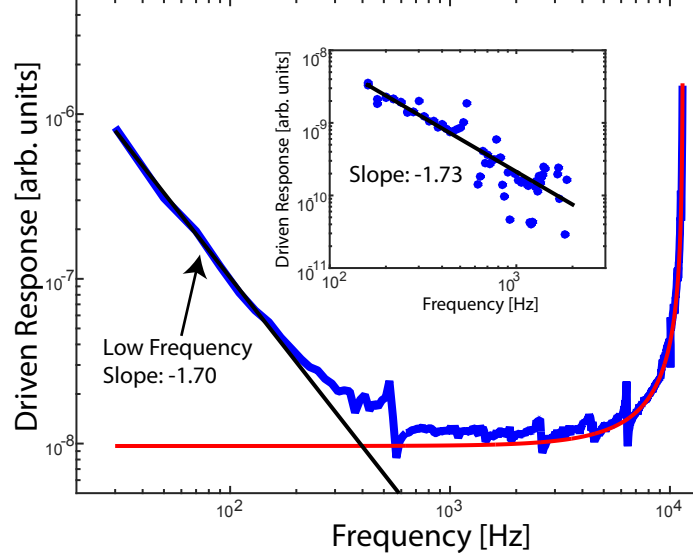


FIG. 29. **Heavy Mass Accelerometer Normalized Driven Response.** This is a plot (in arb. units) of the response of the heavy mass accelerometer with the laser approximately half a linewidth red-detuned from the optical resonance, normalized by the drive strength. The red line is the expected response based solely on the susceptibility of the mechanical mode at  $\omega_m = 2\pi \times 11.48$  kHz, which is in excellent agreement down to several hundred Hz. At low frequency the response increases as  $\omega^{-1.7}$  and this behavior is repeated even when the laser is far-detuned from the optical resonance (inset). This reasonably agrees with the  $\omega^{-2}$  response expected for a low-lying taper mode.

In vacuum, the device is less able to conduct heat from absorbed photons away from optical cavity and the thermo-optic bistability sets in at a lower optical power. In air, mechanical noise from the “rigid” side of the optical cavity was  $\sim 12$  dB above shot noise (see Fig. 27a). Therefore, even at this 8 dB lower power, we’d expect this mechanical noise to 4 dB above shot noise, if not reduced. However, in Fig. 30a, we see that the noise floor is set predominantly by shot noise of the laser light, meaning the mechanical noise of the “rigid” side has been reduced by going to vacuum and increasing the  $Q_m$  of those modes. The inset of Fig. 30a plots the autocorrelation of the amplitude of the fundamental in-plane mechanical mode of the test mass, which yields  $Q_m = 75,000$  (see Section III and Fig. 7 for more information on this technique).

The resolution of the heavy mass accelerometer in vacuum is shown in Fig. 31. We plot both the “driven response” calibration and the “assumed response” calibration. Once again, the presence of a low-frequency taper mode is inferred from the driven data, and therefore at low-frequency we trust the “assumed response” calibration. The resolution in vacuum from approximately 1 kHz to 10 kHz, is approximately 1.5 times lower than the resolution in air (Fig. 28). This makes sense given the additional 4 dB of signal to noise we have in our vacuum measurement (this 4 dB is argued for in the previous paragraph), note that  $\sqrt{10^{\frac{4}{10}}} \approx 1.5$ . Note also that the minimum of the acceleration resolution occurs near the mechanical resonance frequency and its value is  $\approx 25 \frac{ng}{\sqrt{Hz}}$ , in agreement with what we expect theoretically for  $a_{th}$  given the increase in  $Q_m$ , so the test mass can still be considered driven by room-temperature thermal noise.

Note that in Fig. 30b we can still see the low frequency noise roll-up, but this device was given

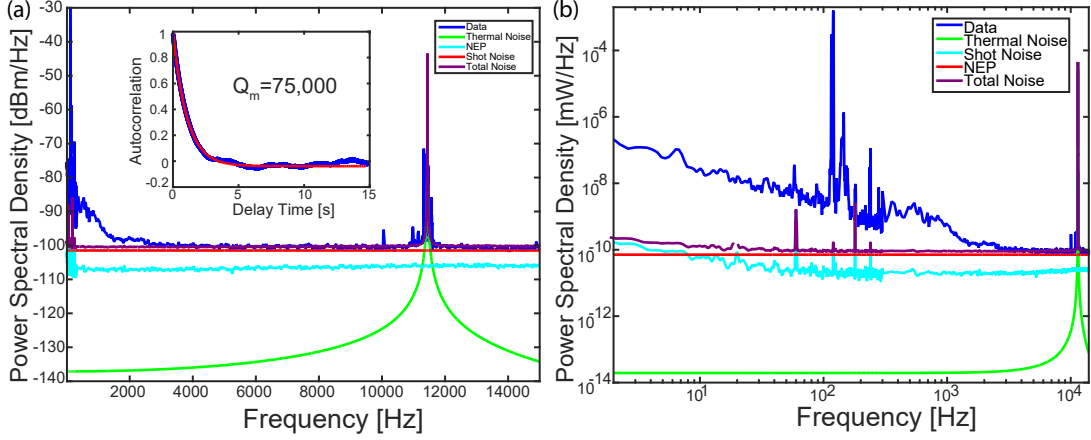


FIG. 30. **Heavy Mass Accelerometer Vacuum Characterization.** (a) Electronic power spectral density of laser light reflected from the optical cavity with the laser approximately half a linewidth red-detuned from the optical resonance in vacuum. (b) same as (a) but on a log-log scale.

a SAM treatment, so this noise is much lower than what it would have been otherwise. If this noise could be further reduced by another 10 dB, using the two laser cancellation technique or refining our SAM treatment techniques, and the  $g_{OM}$  of the structure was increased to  $200 \frac{\text{GHz}}{\text{nm}}$  (demonstrated in Ref. [3]), the resolution would be  $\lesssim 1 \mu g$  over the entire bandwidth shown (ignoring the couple taper modes, which can be eliminated with V-groove coupling).

### C. An Optomechanical Gyroscope

After exploring and developing an optomechanical accelerometer, it is natural to consider what other types of sensors could benefit from optomechanical displacement sensing. Micromachined vibratory gyroscopes, which sense rates of rotation, are the obvious candidate. Their use has increased greatly in recent years with applications ranging from inertial navigation (when paired with accelerometers) to automotive ride-stabilization to video recording stabilization and the video game industry [5]. In this chapter, we'll explore the working principle of micromachined vibratory gyroscopes and the progress we made towards developing an optomechanical version.

#### XI Introductory notes on rotation sensing

The first question to answer is how micromachined vibratory gyroscopes sense rotation. Imagine that you wanted to prove to a child that the earth is indeed spinning, how would you do so? One popular and conceptually easy proof of the earth's rotation is the dynamics of a Foucault pendulum. The plane in which the pendulum swings precesses due to the coriolis force, a force unique to rotating reference frames. In a similar vein, micromachined gyroscopes leverage the coriolis force by monitoring how it causes vibrational motion in one mechanical resonance to be transferred into another orthogonal mechanical resonance. For reference, the form of the coriolis force,  $F_c$ , is provided below, where  $m$  is the mass of the test mass,  $\Omega$  is the angular velocity of the test mass's reference frame,  $v$  is the velocity of the test mass, and  $\times$  represents the cross-product.

$$F_c = -2m\Omega \times v \quad (35)$$



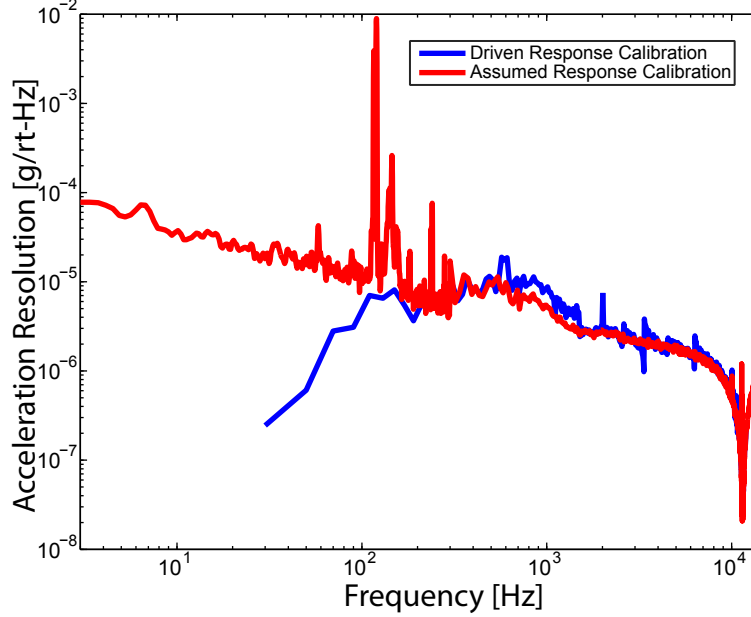


FIG. 31. **Heavy Mass Accelerometer Vacuum Resolution.** Plotted here is the acceleration resolution (a.k.a. noise equivalent acceleration) of the heavy-mass accelerometer in vacuum. A description of the two techniques used to calibrate the resolution, “driven response” and “assumed response”, can be found in the main text.

A cartoon of a z-axis canonical vibratory gyroscope is shown in Fig. 32. This style of gyroscope incorporates an accelerometer, however, instead of just a single mechanical mode for sensing with stiffness  $k_{\text{sense}} = m\omega_{\text{sense}}^2$ , and quality factor,  $Q_{\text{sense}}$ , the test mass is now engineered to have a second orthogonal mechanical mode, called the “drive” mode with stiffness  $k_{\text{drive}} = m\omega_{\text{drive}}^2$ , and quality factor,  $Q_{\text{drive}}$ . The idea is to purposefully ring-up (drive) motion in the aptly named “drive” mode and then observe the amplitude of motion in the sense mode and, from that, infer the magnitude of the angular velocity,  $\Omega$ . Walking through a general example, let’s suppose the drive mode is rung-up to an amplitude  $A$ , its velocity will then be  $v = A\omega_{\text{drive}}\sin(\omega_{\text{drive}}t)$  (in the y-direction, using the reference frame of Fig. 32), if there is a constant angular rotational velocity of magnitude,  $\Omega$ , in the z-direction, the coriolis acceleration will be in the sense ( $x$ ) direction and its magnitude is

$$a_c = 2A\omega_{\text{drive}}\sin(\omega_{\text{drive}}t)\Omega. \quad (36)$$

A fundamental sensing limit for such a vibratory gyroscope, similar to the accelerometer, comes from the fundamental thermal motion of the test mass in the sense mode. This thermal motion of the sense mode will be indistinguishable from the motion caused by rotations that we wish to detect. From Eq. (3) we know the noise equivalent acceleration of the test mass in the sense mode due to fundamental thermal noise. Furthermore, from Eq. (36), we know the acceleration expected in the sense mode for angular velocity of magnitude  $\Omega$ . Combining Eq. (3) and the amplitude of Eq. (36) allows us to write the fundamental thermal noise limited noise equivalent rotation for a

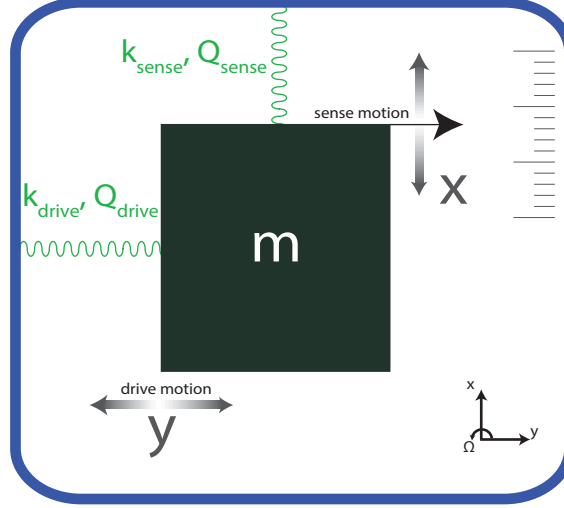


FIG. 32. **Canonical Gyroscope.** This is a cartoon of a canonical vibratory gyroscope. It is adapted from the canonical accelerometer shown in Fig. 1. In much the same way as the accelerometer, there is a “sense” mechanical mode with stiffness  $k_{\text{sense}} = m\omega_{\text{sense}}^2$  and quality factor,  $Q_{\text{sense}}$ , which is used to sense mechanical motion. Now, there is also a “drive” mechanical mode, with stiffness  $k_{\text{drive}} = m\omega_{\text{drive}}^2$ , and quality factor,  $Q_{\text{drive}}$ , which allows the test mass to move in a direction orthogonal to the sense mode. If the test mass is rotating about the z-axis and moving in the drive mode the resulting coriolis force will cause a displacement in the sense mode, which can be read-out and used to infer the rotational velocity.

vibratory gyroscope as follows [63, 64].

$$\Omega_{\text{th}} = \sqrt{\frac{k_B T \omega_{\text{sense}}}{m Q_{\text{sense}} \omega_{\text{drive}}^2 A^2}} \quad (37)$$

Into Eq. (37) we can plug in the parameters of our demonstrated accelerometers, assuming we have also engineered a drive mode of comparable frequency, and integrate electrostatic drive capacitors on-chip (like those discussed in Section VII). Assuming the parameters of the device presented in part A. and a drive amplitude of  $1 \mu\text{m}$  results in  $\Omega_{\text{th}} \approx 10^\circ/\text{hour}/\sqrt{\text{Hz}}$ , and with a drive of  $10 \mu\text{m}$ ,  $\Omega_{\text{th}} \approx 1^\circ/\text{hour}/\sqrt{\text{Hz}}$ . If instead we assume the device parameters of the heavy accelerometer from Section X in vacuum, assuming a drive amplitude of  $1 \mu\text{m}$  results in  $\Omega_{\text{th}} \approx 0.3^\circ/\text{hour}/\sqrt{\text{Hz}}$ , and with a drive of  $10 \mu\text{m}$ ,  $\Omega_{\text{th}} \approx 0.03^\circ/\text{hour}/\sqrt{\text{Hz}}$ . The noise-equivalent rotation is called the angular random walk (obviously, not necessarily set by thermal noise of the sense mode), and its value for several devices from the literature is shown in Fig. 33 (this figure is adapted from Ref. [64]). Our projected thermal noise numbers are shown as red stars in Fig. 33, and indicates that gyroscopes of navigation grade should be possible.

## XII Gyro design, fabrication, and characterization

Our gyro design is based around the zipper-cavity optomechanical accelerometer described above, but with a structure engineered to have a de-coupled, orthogonal drive mode as well the primary sense mode of the initial accelerometer designs. The simplest way to achieve this is to attach the

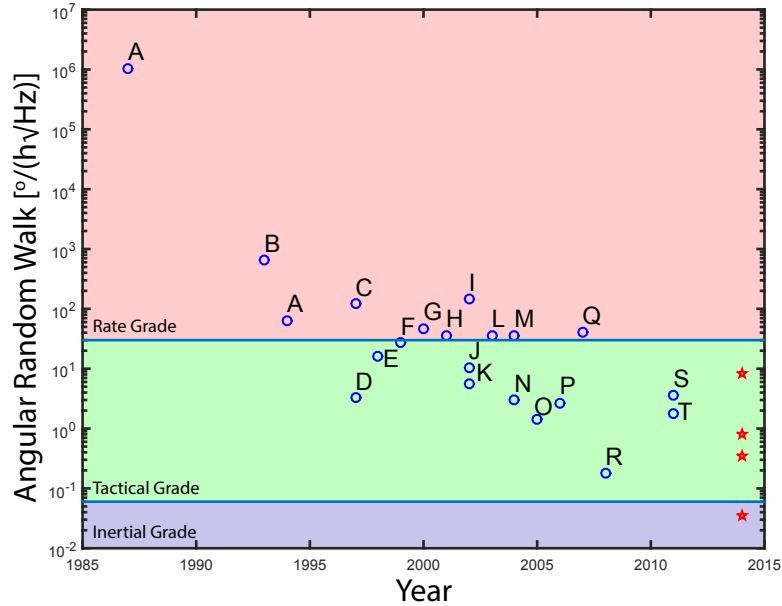


FIG. 33. **ARW of Micromachined Gyroscopes.** This figure is adapted from Ref. [64]. A is Ref. [65]. B is Ref. [66]. C is Ref. [67]. D is Ref. [68]. E is Ref. [69]. F is Ref. [70]. G is Ref. [71]. H is Ref. [72]. I is Ref. [73]. J is Ref. [74]. K is Ref. [75]. L is Ref. [76]. M is Ref. [77]. N is Ref. [78]. O is Ref. [79]. P is Ref. [80]. Q is Ref. [81]. R is Ref. [82]. S is Ref. [83]. T is Ref. [84]. The thermal noise limited angular random walk of our proposed devices are shown as red stars. The regions for rate, tactical, and inertial grade gyroscopes are taken from Ref. [5].

accelerometer to a “frame”, which is in turn suspended from the bulk in the orthogonal direction. A Comsol simulation of an example configuration is shown in Fig. 34.

One must take care, however, when attempting to implement this method. The frame (rectangular annulus) cannot simply be made from the same silicon nitride device layer of the accelerometer. The reason being, if this frame of nitride is released from the underlying silicon, all of its internal stress will be released. This, in turn, will cause the stress to disappear from the nano-strings supporting the enclosed accelerometer. All of the great advantages that high-stress silicon nitride provides (notably high mechanical frequencies and quality factors) will be lost. We must design the frame in such a way that the stress is maintained, which means leaving the silicon layer on the backside of the frame. In this way, the silicon will hold the nitride in place, preventing it from contracting and releasing its stress. Comsol mechanical simulations illustrating these results are shown in Fig. 35.

The way to design the gyroscope, therefore, is to take the heavy-mass accelerometer (shown in Fig. 26 and discussed in Section X) and add the accelerometer from part A. to the center of the large test mass and add electrostatic driving capacitors. Optical microscope images of a fabricated prototype of an optomechanical gyroscope is shown in Fig. 36. As can be seen by comparing Fig. 36 to Fig. 26, the structures are qualitatively similar with the device in Fig. 36 having some added features. The large rectangle in the center of the image is the “frame” and it is fully suspended by thousands of nanostring drive mode support tethers. There is a large gap opened up in the middle of the support tethers where an optical cavity is made. One of the zipper optical beams is placed

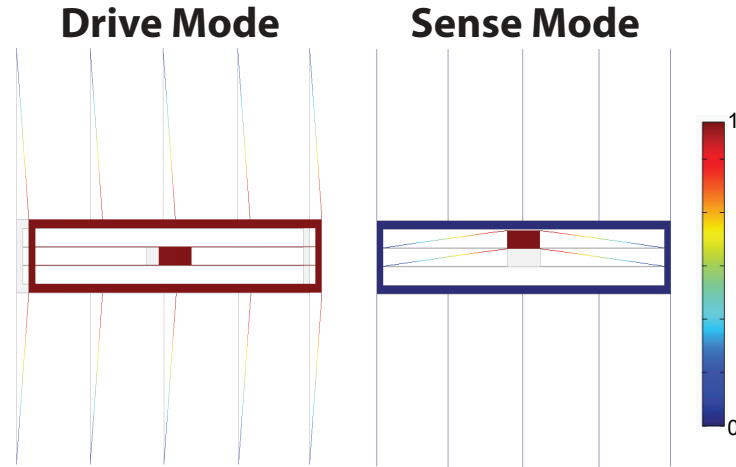


FIG. 34. **Comsol Simulation of Drive and Sense Modes.** Comsol eigenmode mechanical simulation illustrating both the sense and drive modes of the example gyroscope structure. Color indicates displacement with blue indicating zero and red indicating 1 on a normalized scale.

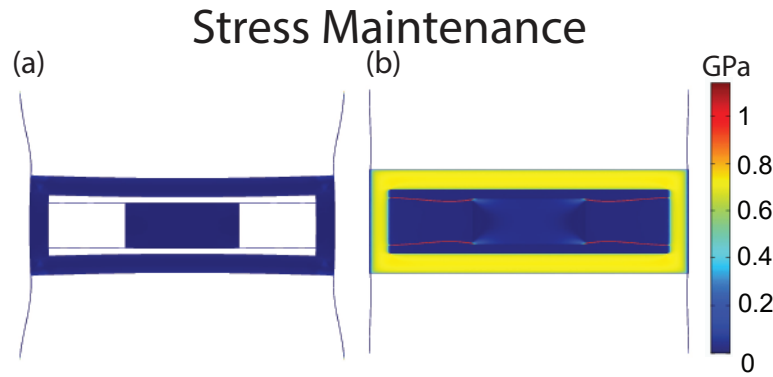


FIG. 35. **Comsol Simulation Stress in Gyro Designs.** This is a plot of the x-axis (along the length of the sense tethers) stress in the example gyroscope structure using Comsol. (a) The case of no silicon on the backside of frame. All of the stress in the nitride film is released, including, most importantly, in the sense mode tethers. (b) In this case,  $\sim 200 \mu\text{m}$  of Silicon is left attached to the underside of the frame. The frame is unable to contract to release its tension, and the sense mode tethers maintain their  $\sim 1 \text{ GPa}$  stress.

on a support tether and the other is connected to a rigid platform protruding from the bulk (see Fig. 36c). The optical cavity is end-coupled to an on-chip optical waveguide with an adiabatic coupler built into it for rapid optical testing using our fiber taper technology. This is called the drive mode optical cavity and is simply used to characterize and monitor the drive mode motion.

In the center of the frame is the sense mechanics, comprised of an accelerometer of the same mechanical design as that studied in part A. and shown in Fig. 3. One side of the zipper optical cavity is connected to the sense mode test mass (see Fig. 36d), the rigid side of the cavity is connected to the frame by its own nanostring tether, and laser light is side-coupled into the optical cavity using an on-chip waveguide. Crucially, the light in this waveguide must make it out of

the frame. This can be done with a dimpled, tapered optical fiber, but, as already discussed (see Section VI), this is far from ideal for a practical sensor. Therefore, we showed, as of proof of principle, that a gap can be opened in the frame, which allows the coupling waveguide too pass through and connect to the bulk. In more advanced designs, this coupling waveguide could be used in a V-groove coupling scheme as in Section VI. In the device shown in Fig. 36, we are only concerned with the proof of principle and the coupling waveguide has an adiabatic coupler region shortly after exiting the frame, upon which a dimpled, tapered fiber is set. The main idea of this waveguide is to couple light into the sense mode optical cavity without disturbing or sensing the drive motion.

Fabricating these devices requires four lithography steps (three electron-beam and one optical). First the metal pattern is written, chrome-gold layer evaporated, and then the topside gyro pattern is aligned to the gold pattern. The topside gyro pattern contains alignment marks to align the backside pattern. The end result is the device in Fig. 36.

The most important fundamental properties of the gyroscope will be the mechanical quality factors of the sense and drive modes. As shown in Eq. (37),  $Q_{\text{sense}}$  sets the thermal noise resolution, and  $Q_{\text{drive}}$  will set the amplitude of the drive mode when the device is driven on resonance. Therefore, it is important to characterize these devices by measuring their mechanical quality factors. The mechanical quality factor of the drive mode in vacuum of a device similar to that shown in Fig. 36 was found to be  $Q_{\text{drive}} = 70,000$ , consistent with the Q-factor of the heavy mass accelerometer in vacuum (see Section X B), which is obviously what one would expect. The mechanical quality factor of the sense mode in vacuum of a device similar to that shown in Fig. 36 was found to be  $Q_{\text{sense}} = 3.7 \times 10^6$ . This data is shown in Fig. 37.

Electrostatic actuation of drive mode is accomplished using interdigitated capacitors on one side of the frame (see Fig. 36a-b). Interdigitated capacitors are necessary as opposed to parallel wire capacitors (as discussed in Section VII A) because of the large amplitude of motion desired. For  $1 \mu\text{m}$  motion, a parallel plate capacitor would need a gap of  $3 \mu\text{m}$  to avoid stiction, which makes its applied force relatively tiny. Interdigitated capacitors capitalize on small gaps between the fingers (here designed to be  $300 \text{ nm}$ ). The capacitance and applied force for an interdigitated capacitor are given below (assuming, for simplicity, parallel plate capacitance between the wires).

$$C_{id} = \frac{2(L-x)\epsilon_0 t}{d} N \quad (38)$$

$$F_{id} = \frac{1}{2} V_a^2 \frac{2\epsilon_0 t}{d} N \quad (39)$$

In Eqs. (38) and (39),  $t$  is the thickness of the wires,  $N$  is the number of interdigitations,  $V_a$  is the applied voltage, and the rest of the geometry is shown in Fig. 38. For our device geometry,  $F_{id}$  is predicted to be approximately 25 times greater than that for a parallel wire capacitor with a gap of  $3 \mu\text{m}$ . Using the equation for mechanical susceptibility of the structure and interdigitated capacitor force from Eq. (39), one obtains a drive amplitude,  $A$ , equal to:

$$A = \frac{1}{2} V_a^2 \frac{2\epsilon_0 t}{d} N \frac{Q_{\text{drive}}}{m_{\text{frame}} \omega_{\text{drive}}^2}. \quad (40)$$

In Fig. 39, we present a calibration of a drive tone applied to the interdigitated capacitors of a device very similar to the one shown in Fig. 36 (except without the sense-mode coupling waveguide).

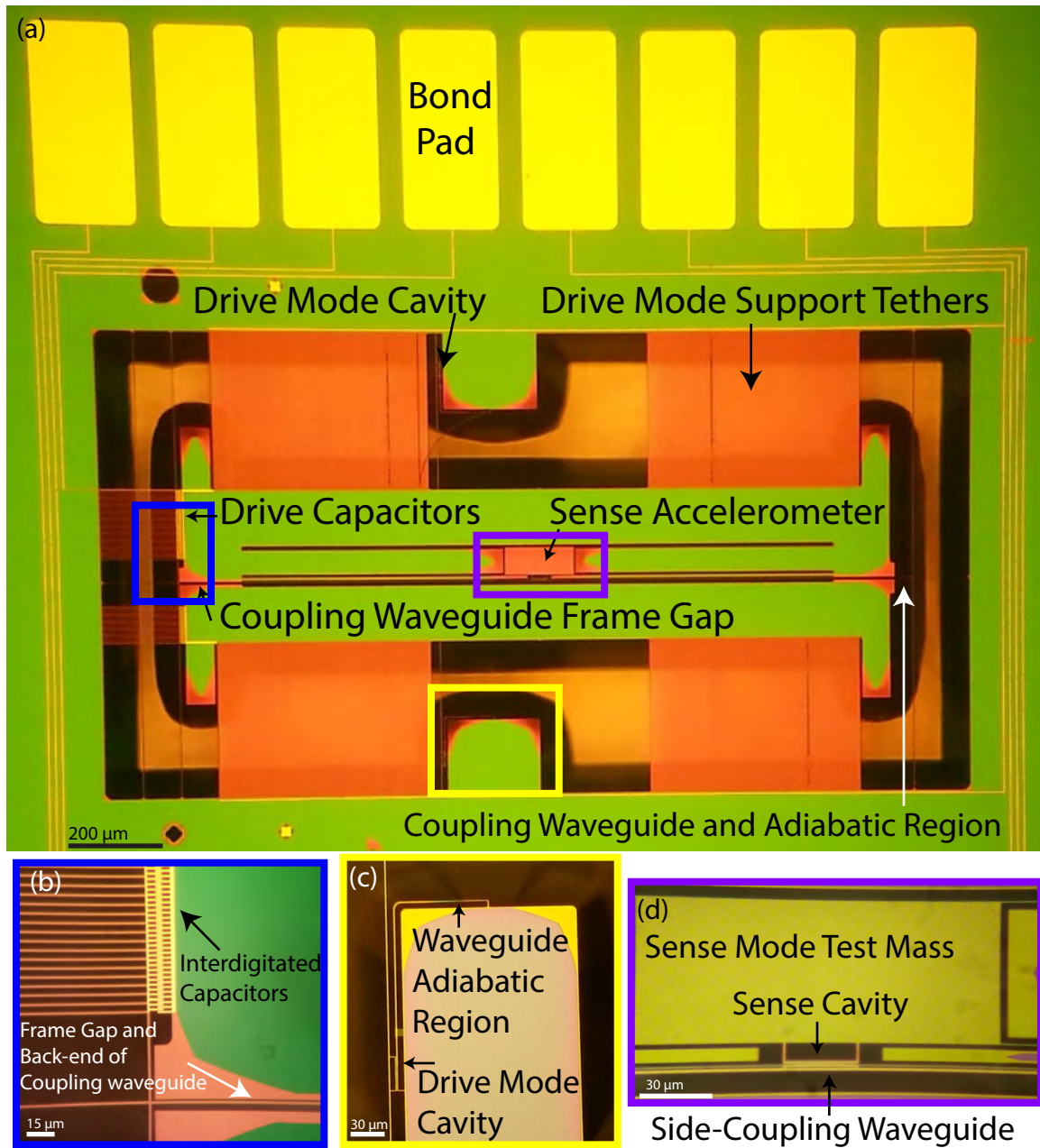


**FIG. 36. Prototype Optomechanical Gyroscope.** These are a series of annotated optical microscope images of a prototype optomechanical gyroscope device. It is qualitatively similar to the heavy-mass accelerometer shown in Fig. 26 with some additional features. (a) Shows an overview of one whole gyroscope device complete with bond pads (only 2 bond pads are used for this devices, the remaining are for other devices on the chip). (b) This image shows a zoom-in of the interdigitated capacitor region and the gap in the frame for the coupling waveguide. (c) Zoom-in of the drive mode optical cavity, showing the optical cavity and its coupling waveguide. (d) Zoom-in of the sense mode test mass with its associated optical cavity and the coupling waveguide.

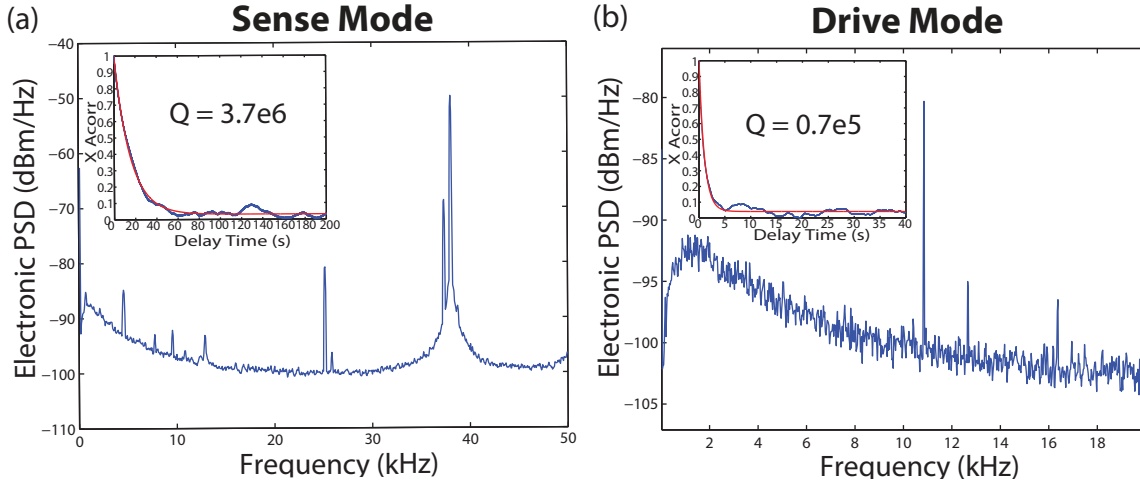


FIG. 37. **Measured Drive and Sense Mode Quality Factors.** (a) Electronic power spectral density of laser light reflected from the sense optical mode. The sense mode is the best transduced feature at approximately 38 kHz. inset: autocorrelation of the sense mode amplitude signal, showing  $Q_{\text{sense}} = 3.7 \times 10^6$ . (b) Electronic power spectral density of laser light reflected from the drive optical mode. The drive mode is the best transduced feature at approximately 11 kHz. inset: autocorrelation of the drive mode amplitude signal, showing  $Q_{\text{drive}} = 70,000$ . The specific devices used to obtain this data were similar to the device shown in Fig. 36, but did not have the metallized capacitors nor the backside frame tethers. Neither of these should significantly affect the mechanical quality factors.

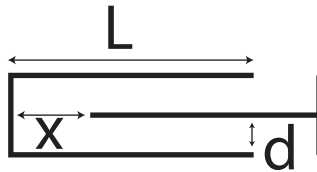
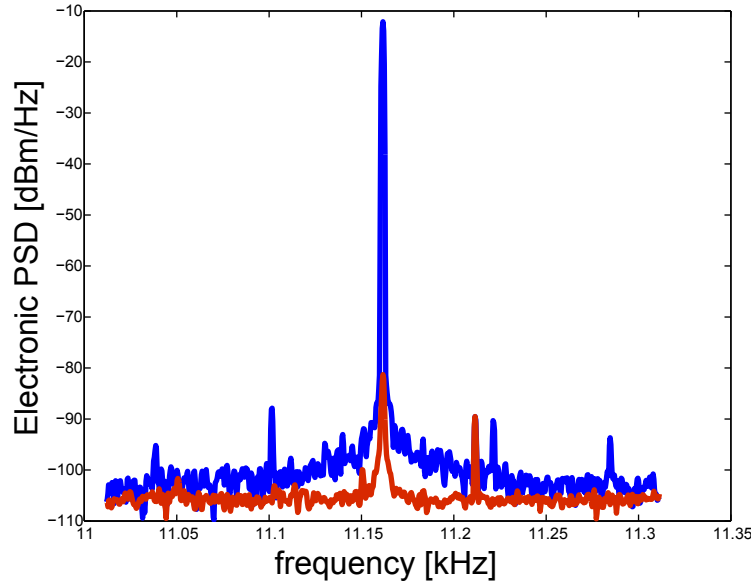


FIG. 38. **Interdigitated Capacitor Geometry.** This is a parameterized geometry for one section of an interdigitated capacitor. The length of each finger (or digit) is  $L$ , the spacing between them in the lateral direction is  $d$ , and the distance between the tip of one finger and the back line is  $x$ . When a voltage is applied there will be a resulting force along the  $x$ -direction.

uide). The mechanical frequency and quality factor of the drive mode were calibrated in vacuum to be  $Q_{\text{drive}} = 21,000$  and  $\omega_m = 2\pi \times 11.165$  kHz. The red curve shows the electronic power spectral density of laser light reflected from the drive optical cavity with the capacitive drive off, and hence this is the thermal noise of the drive mode. The blue curve is the electronic PSD with 1 Volt applied to the interdigitated capacitors at the half-frequency of the drive mechanical mode (because  $F_{id} \sim V_a^2$ , one must drive at the half-frequency). Comparing the driven tone height to the measured thermal noise height allows us to calibrate the driven tone height to be an amplitude of 4 nm. This is comparable to the prediction of Eq. (40),  $A = 6.8$  nm, using the measured parameters of  $V_a = 1$ ,  $t = 200$  nm,  $d = 300$  nm,  $N = 78$ ,  $Q_{\text{drive}} = 21000$ ,  $m = 290$  nKg, and



$\omega_m = 2\pi \times 11.165$  kHz. Unfortunately, we cannot calibrate drive mode amplitudes significantly larger than this because the optical transduction scheme becomes non-linear (mechanical displacements shift the optical cavity frequency by an amount comparable to or greater than its linewidth). However, we can successfully apply 10 Volts to the capacitors and, extrapolating this calibration, this corresponds to a drive amplitude of  $0.4 \mu\text{m}$ , on the order of the drive amplitudes we were hoping for in Section XI.



**FIG. 39. Calibration of Gyroscope Drive Amplitude.** This is a comparison of the electronic power spectral density of laser light reflected from the drive optical mode with the interdigitated capacitor drive on (blue curve) and off (red curve). The capacitors are driven with 1 Volt at the half-frequency of the mechanical mode. By comparing the height of the driven tone (blue) to the thermal noise curve (red) we can calibrate the drive amplitude to be 4 nm.

### XIII Vibration Isolation

The prototype gyroscope discussed in the last section and shown in Fig. 36 has the drawback that it is sensitive to linear accelerations as well as rotations. If a vibration (linear acceleration) struck the device along the sense axis, the sense mode would respond and produce an output. This is non-ideal. Ideally, when the gyroscope produces an output near the drive frequency the user should be confident the sensor is measuring a rotation and not a linear acceleration.

This is a well-known problem in micromachined gyroscopes and for an excellent introduction to the design of gyroscopes with vibration immunity see Chapter 1 of Ref. [64]. One solution is to use symmetry to cancel out linear accelerations. Dual mass [82] and even quad-mass [83, 85] gyroscopes have been developed, which utilize symmetry between the coupled masses to gain immunity from linear accelerations. The main idea of designs such as these is to engineer a drive mode where the identical masses move completely out-of-phase with one another. Then the coriolis force on each mass will be of equal magnitude, but opposite direction, thus driving the out-of-phase sense mode. Linear accelerations, on the other hand, will force the identical masses in the same direction. This allows one to distinguish between linear acceleration and rotations by designing



your sense electrodes to reject common motion and sense differential motion. Another solution to vibration sensitivity is a degenerate mode disk gyroscope (see Ref. [81] for an example). Here two ideally degenerate internal flexural modes of a disk are used as the drive and sense modes. Since these modes have zero net momentum, they can not be excited by linear accelerations.

The provided examples [81–83] are certainly highly impressive. However, the dual mass and quad mass designs of Refs. [82, 83, 85] have considerable design complexity, the need for very precise and robust nanofabrication so that the masses are as close to identical as possible, and control electronics to counter fabrication imperfections for optimal performance. The disk gyroscope [81] is elegant even if it does have small drive mode displacements given the high frequencies of the mechanical mode. Additionally, the design does not work well with our silicon nitride structures because all of the stress (and the benefits it provides) is released in such designs.

An alternative to defeating linear acceleration sensitivity with symmetry is to implement passive low-pass mechanical filters (i.e., vibration isolation stages) to prevent vibrations and linear acceleration from reaching the sensor of the device. These techniques are known to the gyroscope community and a good introduction is provided by Chapter 3 of Ref. [86]. A prominent example of a passive vibration isolation stage in the literature is a vacuum packaging system complete with isolation suspensions and an isolation platform to which the MEMS device is bonded [87–89]. Another example is a chip-scale vibration isolation platform that is fabricated separately from the sensor and to which the sensor is later bonded [90]. These results, while certainly impressive, add a great deal of complexity to the fabrication and design process. We sought a simple solution to vibration isolation that would require no additional fabrication steps or processes.

This can be achieved by connecting the gyroscope to another frame that has a low resonance frequency (100's of Hz to a few kHz). This can be viewed as a continuation of the structure we've already shown in Fig. 36. Just as the inner accelerometer is connected to the frame which is also suspended, we can suspend this entire gyro structure on yet another frame with a low resonance frequency that will damp out high-frequency vibrations. This method requires no extra fabrication steps or techniques and is trivial to incorporate into our existing fabrication methods. We will discuss the design in much more detail below, but first we will describe the working principle of this passive mechanical isolation scheme.

### A Passive mechanical isolation: working principles

Prima facie, this passive mechanical isolation scheme may seem counter-intuitive, as in, we will reduce our signal as much as our noise and thereby gain nothing. The key point to remember is that signals in a vibratory gyroscope will be mixed up to the drive frequency, as dictated by Eq. (36). For example, a constant rotation will appear at the drive frequency. What becomes important, therefore, is our confidence that output signal from the gyroscope in some specified bandwidth around the drive frequency is due to rotations and not linear accelerations. Thus, we can design a low-pass passive mechanical filter that allows our low-frequency signals to pass through, and greatly damps linear vibrations at/near the drive frequency.

This is simply accomplished by attaching our gyroscope to a mechanical structure with a low frequency resonance (say around 1 kHz). Vibrations much below 1 kHz will pass unfettered, while vibrations much above 1 kHz will be attenuated because the low frequency mechanical resonance will not be able to significantly respond at those frequencies. To be more exact, we can write down a mathematical model for this vibration isolation. Suppose we shake the entire chip with some amplitude,  $x_{\text{chip}}$ , and at a variable frequency,  $\omega$ . The motion of the low frequency mechanical resonance, hereafter called the frame, relative to the chip,  $x_{\text{frame,rel}}$ , is simply given by the following.

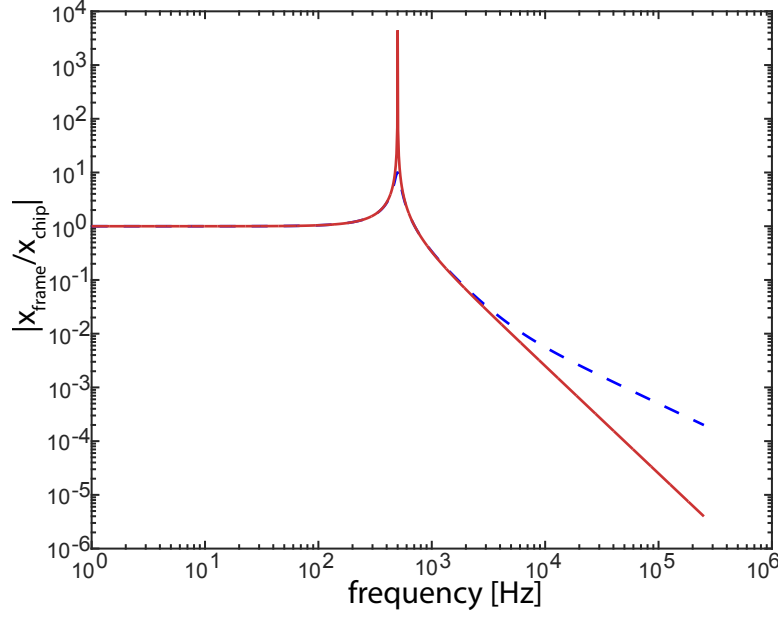


FIG. 40. **Passive Mechanical Isolation Theory.** This is a plot of Eq. (43) for the case of  $\omega_m = 2\pi \times 500$  Hz and  $Q_m = 5000$  (solid red curve) and  $Q_m = 10$  (dashed blue curve).

$$x_{\text{frame,rel}} = x_{\text{chip}} \omega^2 \chi(\omega) \quad (41)$$

In Eq. (41),  $\chi(\omega)$  is the mechanical susceptibility to accelerations. Therefore, the absolute motion of the frame,  $x_{\text{frame}}$ , is given by the following.

$$|x_{\text{frame}}| = |x_{\text{chip}} + x_{\text{chip}} \omega^2 \chi(\omega)| \quad (42)$$

$$\left| \frac{x_{\text{frame}}}{x_{\text{chip}}} \right| = |1 + \omega^2 \chi(\omega)| \quad (43)$$

Eq. (43) is plotted in Fig. 40 using two different frame resonators both with  $\omega_m = 2\pi \times 500$  Hz and one with  $Q_m = 5000$  (solid red curve) and the other with  $Q_m = 10$  (dashed blue curve). For both resonators,  $\left| \frac{x_{\text{frame}}}{x_{\text{chip}}} \right| = 1$  for frequencies below the resonance frequency of the frame. As one can see in Fig. 40, for frequencies above the frequency of the frame,  $\left| \frac{x_{\text{frame}}}{x_{\text{chip}}} \right|$  falls off like  $\left( \frac{\omega}{\omega_m} \right)^{-2}$  (as long as the  $Q_m$  is reasonably high, for low  $Q_m$  the suppression is not as large). That is,  $\left| \frac{x_{\text{frame}}}{x_{\text{chip}}} \right| = 10^{-2}$  for  $\frac{\omega}{\omega_m} = 10$  and  $\left| \frac{x_{\text{frame}}}{x_{\text{chip}}} \right| = 10^{-4}$  for  $\frac{\omega}{\omega_m} = 100$  (for the case that  $Q_m \gtrsim 5000$ ). In this way, incoming vibrations at low frequency are allowed to pass while those at high frequency are greatly suppressed. This is the type of behavior we expect to observe in the next section.

## B Frame Isolation Results

The device used for passive mechanical isolation using concatenated frames surrounding the sensor is shown in an optical image in Fig. 41. A more basic schematic of the device is shown in Fig. 42. In these images, a gyroscope very similar to the one shown in Fig. 36, instead of being mounted to the bulk of the chip, is mounted to a frame. This frame is suspended by the same nanostring tethers as the gyroscope drive mode, there's just far fewer of them (10's or 100's of tethers instead of 1000's for the gyroscope drive mode). This gives the first frame a low frequency, fundamental in-plane mechanical resonance in the drive direction. This first frame is mounted to a second frame that is suspended by nanostring tethers in the orthogonal direction. This gives the second frame a low frequency, mechanical resonance in the sense mode direction. Combined, these two frames should provide isolation from linear accelerations in both the x and y directions. These frames should also provide attenuation for z-axis vibrations because the frames also have fundamental out-of-plane mechanical modes at nearly degenerate frequencies to the fundamental in-plane mode (as seen first in Fig. 6), although this will not be tested. These devices are fabricated using the exact same double-sided lithography methods used previously in this thesis for the heavy-mass accelerometer and the gyroscope.

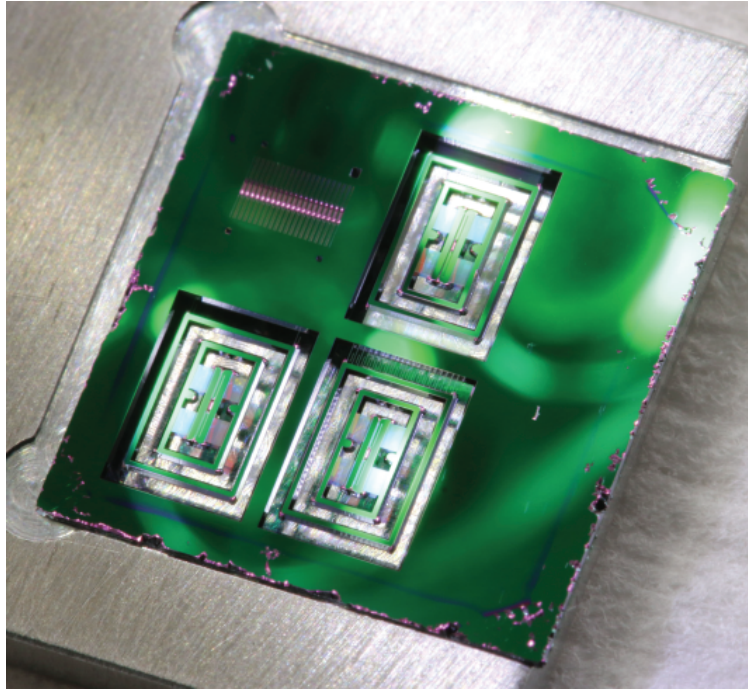


**FIG. 41. Vibration Isolation Device Optical Image.** This is an optical image of the chip containing the frame structures for vibration isolation testing. The chip contains three gyroscope devices, each located at the center of a set of nested frames. The first frame (moving outwards from the center) is suspended such that it suppresses vibration in the drive-mode direction and vice-versa for the second frame. In the upper right-hand corner of the chip there is a field of non-isolated accelerometers, used for calibration.

In order to confirm that the frames do indeed provide vibration isolation, we subjected the chip to shaker table tests (the shaker table was first described in Fig. 4). Included on the chip was a field of non-isolated accelerometers (see Fig. Fig. 41), which were used as a baseline. Accelerations

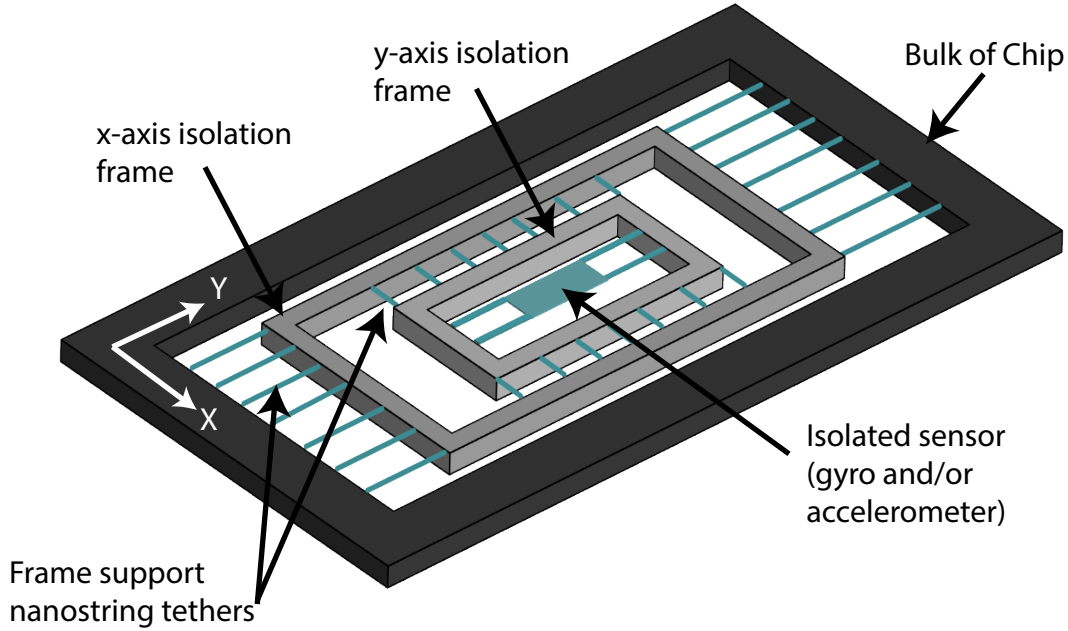


FIG. 42. **Vibration Isolation Device Schematic.** This is a simplified schematic version of the vibrational isolation structure. At the center of the nested frames we did not draw the full gyroscope structure, but a simple sensor for clarity.

tions were applied to the chip, observed by the optomechanical accelerometer, and compared to the intrinsic thermal noise of the fundamental in-plane mechanical mode. These shaker tests were repeated with two of the isolated accelerometers, again comparing the transduced tone to the intrinsic thermal noise for an absolute calibration. Light was coupled into the structures using the dimpled, tapered optical fiber and on-chip adiabatic waveguide couplers. The data is presented in Fig. 43.

Fig. 43a shows the results of shaking the non-isolated accelerometers, Fig. 43b shows data for shaking an accelerometer isolated by a set of  $x$ - $y$  frame isolators each with 180 nanotethers on a side, and Fig. 43c shows data for shaking an accelerometer isolated by a set of  $x$ - $y$  frame isolators each with 19 nanotethers on a side. It must be noted that that the applied acceleration tones shown in Fig. 43 have been normalized such that they all correspond to the same voltage applied to shear piezo. This was done to allow the reader to easily observe the diminishing tone heights with increased isolation. In practice, the non-isolated accelerometers must be shaken with much smaller amplitudes than the isolated accelerometers or else transduction will become non-linear. The intrinsic thermal noise for each device is plotted in red in Fig. 43. The intrinsic mechanical quality factors of each device were within 10% of  $3 \times 10^6$ , and the shake measurements were taken at optical powers where optomechanical back-action was insignificant. By comparing each applied acceleration tone (blue) to the intrinsic thermal noise of each device (red) we obtain the inferred acceleration for each device. Then we compare each device to the bare (non-isolated) accelerometer to obtain the amount of vibration isolation. For the frame isolation device in Fig. 43b, with 180 nanotethers on each side of the frames, the average vibration suppression is 22 dB. For the frame isolation device in Fig. 43c, with 19 nanotethers on each side of the frames, the average vibration suppression is 32 dB. This implies a corresponding fundamental in-plane mechanical mode of

approximately 3.1 kHz and 950 Hz, respectively.

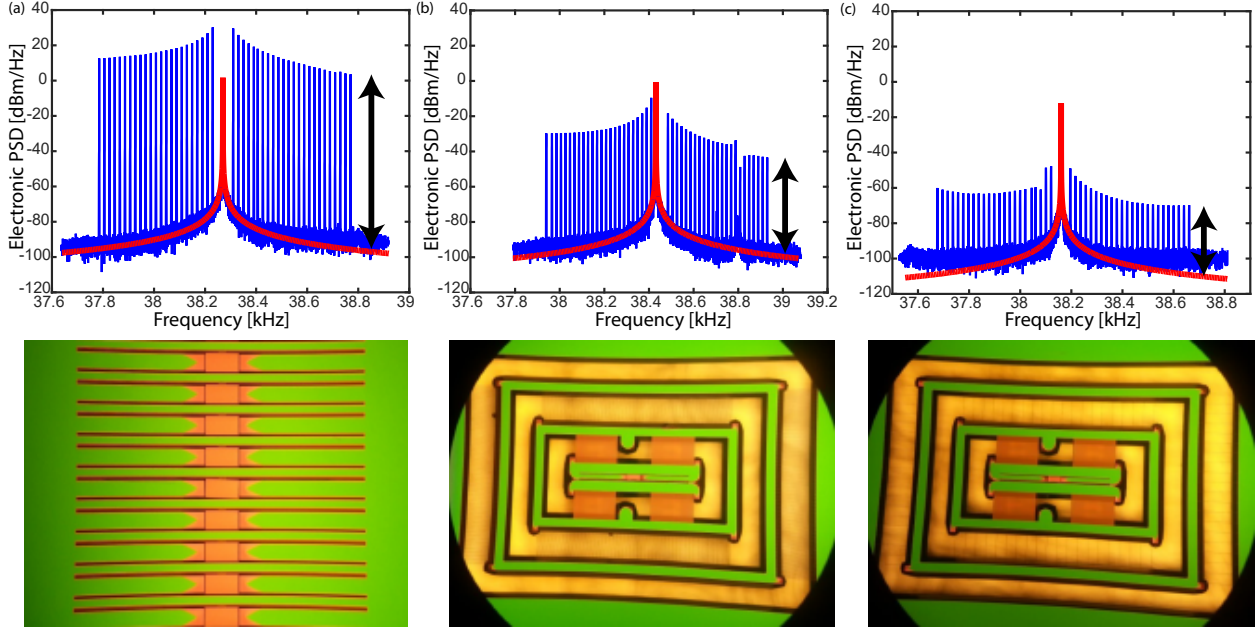


FIG. 43. **Vibration Isolation Results.** (a) Electronic power spectral density of light reflected from a non-isolated accelerometer's optical resonance. The blue spikes are accelerations due to applying a tone at that frequency to the shaker table. Their heights have been normalized to correspond to the drive strengths used for the isolated device in (c). Absolute acceleration calibration is obtained by comparing the blue tone heights to the fitted intrinsic thermal noise of the device. Below the plot is an optical microscope image of example non-isolated optomechanical accelerometers. (b) Same as in (a) except the internal accelerometer is isolated from the environment using a set of  $x$ - $y$  isolator frames each suspended by 180 nanotethers on a side. (c) Same as (b) except the device now has frames suspended by 19 nanotethers on a side.

#### XIV Conclusions

In this chapter we have described our work to develop several of the key pieces needed to demonstrate an optomechanical gyroscope. That is, high mechanical quality factors on both the drive and sense modes, reasonable drive amplitudes for improved resolution, and a simple method to isolate our devices from unwanted linear accelerations. If the demonstrated vibration isolation is insufficient for a given application, the results can, in theory, be significantly improved by chaining on additional isolation frames. As an additional note, such vibration isolation may be useful for a wide range of practical sensors, including improving cross-axis sensitivity in accelerometers.

## E. References

- [1] G. M. Harry and the LIGO Scientific Collaboration, *Classical and Quantum Gravity* **27**, 084006 (2010).
- [2] J. Aasi and the LIGO Scientific Collaboration, *Classical and Quantum Gravity* **32**, 115012 (2015).
- [3] M. Eichenfield, R. Camacho, J. Chan, K. J. Vahala, and O. Painter, *Nature* **459**, 550 (2009).
- [4] G. Krishnan, C. U. Kshirsagar, G. K. Ananthasuresh, and N. Bhat, *Journal of the Indian Institute of Science* **87**, 333 (2012).
- [5] N. Yazdi, F. Ayazi, and K. Najafi, *Proceedings of the IEEE* **86**, 1640 (1998).
- [6] P. Zwahlen, A. M. Nguyen, Y. Dong, F. Rudolf, M. Pastre, and H. Schmid, in *2010 IEEE 23rd International Conference on Micro Electro Mechanical Systems (MEMS)* (IEEE, 2010) pp. 631–634.
- [7] *Accelerometer Selection Based on Applications*, Tech. Rep. (Endevco, 2006).
- [8] C. Acar and A. M. Shkel, *Journal of Micromechanics and Microengineering* **13**, 634 (2003).
- [9] H. Kulah, J. Chae, N. Yazdi, and K. Najafi, *IEEE Journal of Solid-State Circuits* **41**, 352 (2006).
- [10] S. Tadigadapa and K. Mateti, *Measurement Science and Technology* **20**, 092001 (2009).
- [11] A. Partridge, J. Reynolds, B. Chui, E. Chow, A. Fitzgerald, L. Zhang, N. I. Maluf, and T. Kenny, *Journal of Microelectromechanical Systems* **9**, 58 (2000).
- [12] C.-H. Liu, A. Barzilai, J. Reynolds, A. Partridge, T. Kenny, J. Grade, and H. Rockstad, *Journal of Microelectromechanical Systems* **7**, 235 (1998).
- [13] R. H. O. U. Krishnamoorthy, *Sensors and Actuators A: Physical* **145**, 283 (2008).
- [14] K. Zandi, B. Wong, J. Zou, R. V. Kruzelecky, W. Jamroz, and Y. A. Peter, in *2010 IEEE 23rd International Conference on Micro Electro Mechanical Systems (MEMS)* (IEEE, 2010) pp. 839–842.
- [15] W. Noell, P.-A. Clerc, L. Dellmann, B. Guldemann, H.-P. Herzig, O. Manzardo, C. Marxer, K. Weible, R. Dandliker, and N. de Rooij, *IEEE Journal of Selected Topics in Quantum Electronics* **8**, 148 (2002).
- [16] T. Berkoff and A. Kersey, *IEEE Photonics Technology Letters* **8**, 1677 (1996).
- [17] H. Nakstad and J. T. Kringlebotn, *Nature Photonics* **2**, 147 (2008).
- [18] X. Jiang, F. Wang, M. Kraft, and B. E. Boser, *Solid-State Sensor, Actuator and Microsystems Workshop, Hilton Head Island* **2**, 2 (2002).
- [19] A. Salian, H. Kulah, N. Yazdi, G. He, and K. Najafi, *Technical Digest. Solid-State Sensor and Actuator Workshop, Hilton Head Island, SC* (2000).
- [20] H. Luo, G. Fedder, and L. Carley, in *The Thirteenth Annual International Conference on Micro Electro Mechanical Systems, 2000. MEMS 2000* (2000) pp. 502–507.
- [21] C. Yeh and K. Najafi, *IEEE Transactions on Electron Devices* **44**, 1875 (1997).
- [22] H. Rockstad, J. Reynolds, T. Tang, T. Kenny, W. Kaiser, and T. Gabrielson, in *The 8th International Conference on Solid-State Sensors and Actuators, 1995 and Eurosensors IX.. Transducers '95*, Vol. 2 (1995) pp. 675–678.
- [23] “Guralp cmg-pepp,” .
- [24] M. Lemkin and B. E. Boser, *IEEE Journal of Solid-State Circuits* **34**, 456 (1999).
- [25] “Adxl05 datasheet,” ().
- [26] C.-H. Liu and T. Kenny, *Journal of Microelectromechanical Systems* **10**, 425 (2001).
- [27] J. Bernstein, R. Miller, W. Kelley, and P. Ward, *Journal of Microelectromechanical Systems* **8**, 433 (1999).
- [28] “Adxl105 datasheet,” ().
- [29] R. Kubena, G. Atkinson, W. Robinson, and F. Stratton, *IEEE Electron Device Letters* **17**, 306 (1996).
- [30] “Endevco, model 752a13 accelerometer,” .
- [31] A. G. Krause, T. D. Blasius, and O. Painter, arXiv:1506.01249 [physics, physics:quant-ph] (2015).

- [32] A. G. Krause, M. Winger, T. D. Blasius, Q. Lin, and O. Painter, *Nature Photonics* **6**, 768 (2012).
- [33] “Comsol multiphysics,” .
- [34] B. C. Stipe, H. J. Mamin, T. D. Stowe, T. W. Kenny, and D. Rugar, *Physical Review Letters* **87**, 096801 (2001).
- [35] W. B. Davenport and W. L. Root, *An introduction to the theory of random signals and noise* (McGraw-Hill, 1958).
- [36] J. D. Cohen, S. M. Meenehan, and O. Painter, *Optics Express* **21**, 11227 (2013).
- [37] M. Winger, T. D. Blasius, T. P. Mayer Alegre, A. H. Safavi-Naeini, S. Meenehan, J. Cohen, S. Stobbe, and O. Painter, *Optics Express* **19**, 24905 (2011).
- [38] A. W. Fang, H. Park, O. Cohen, R. Jones, M. J. Paniccia, and J. E. Bowers, *Optics Express* **14**, 9203 (2006).
- [39] S. M. Meenehan, *Cavity Optomechanics at Millikelvin Temperatures*, phd, California Institute of Technology (2015).
- [40] A. Yariv and P. Yeh, *Photonics: Optical Electronics in Modern Communications* (Oxford University Press, 2007).
- [41] A. B. Matsko, A. A. Savchenkov, N. Yu, and L. Maleki, *Journal of the Optical Society of America B* **24**, 1324 (2007).
- [42] A. Chijioke, Q.-F. Chen, A. Y. Nevsky, and S. Schiller, *Physical Review A* **85**, 053814 (2012).
- [43] M. L. Gorodetsky and I. S. Grudinin, *Journal of the Optical Society of America B* **21**, 697 (2004).
- [44] S. S. Verbridge, J. M. Parpia, R. B. Reichenbach, L. M. Bellan, and H. G. Craighead, *Journal of Applied Physics* **99**, 124304 (2006).
- [45] K. Yasumura, T. Stowe, E. Chow, T. Pfafman, T. Kenny, B. Stipe, and D. Rugar, *Journal of Microelectromechanical Systems* **9**, 117 (2000).
- [46] Y. T. Yang, C. Callegari, X. L. Feng, and M. L. Roukes, *Nano Letters* **11**, 1753 (2011).
- [47] M. Girons i Nogu, *Inorganic and polymeric microsieves : strategies to reduce fouling*, info:eu-repo/semantics/doctoralThesis, University of Twente, Enschede (2005).
- [48] S. I. Raider, R. Flitsch, J. A. Aboaf, and W. A. Pliskin, *Journal of The Electrochemical Society* **123**, 560 (1976).
- [49] D. B. Asay and S. H. Kim, *The Journal of Physical Chemistry B* **109**, 16760 (2005).
- [50] M. A. Henderson, *Surface Science Reports* **46**, 1 (2002).
- [51] S. H. Lee and P. J. Rossky, *The Journal of Chemical Physics* **100**, 3334 (1994).
- [52] M. James, T. A. Darwish, S. Ciampi, S. O. Sylvester, Z. Zhang, A. Ng, J. J. Gooding, and T. L. Hanley, *Soft Matter* **7**, 5309 (2011).
- [53] M. Szri, P. Jedlovsky, and M. Roeselov, *Physical Chemistry Chemical Physics* **12**, 4604 (2010).
- [54] M. M. Sung, G. J. Kluth, and R. Maboudian, *Journal of Vacuum Science & Technology A* **17**, 540 (1999).
- [55] U. Srinivasan, M. Houston, R. Rowe, and R. Maboudian, in , *1997 International Conference on Solid State Sensors and Actuators, 1997. TRANSDUCERS '97 Chicago*, Vol. 2 (1997) pp. 1399–1402 vol.2.
- [56] R. Maboudian, W. R. Ashurst, and C. Carraro, *Sensors and Actuators A: Physical* **82**, 219 (2000).
- [57] U. Srinivasan, M. Houston, R. Howe, and R. Maboudian, *Journal of Microelectromechanical Systems* **7**, 252 (1998).
- [58] R. Zhang, C. Ti, M. I. Davano, Y. Ren, V. Aksyuk, Y. Liu, and K. Srinivasan, *Applied Physics Letters* **107**, 131110 (2015).
- [59] Y. Rudich, I. Benjamin, R. Naaman, E. Thomas, S. Trakhtenberg, and R. Ussyshkin, *The Journal of Physical Chemistry A* **104**, 5238 (2000).



- [60] J. Hautman and M. L. Klein, *Physical Review Letters* **67**, 1763 (1991).
- [61] R. A. Norte, *Nanofabrication for On-Chip Optical Levitation, Atom-Trapping, and Superconducting Quantum Circuits*, phd, California Institute of Technology (2015).
- [62] H. M. Gibbs, *Optical Bistability: Controlling Light with Light* (Academic Press, 1985).
- [63] H. Xie and G. Fedder, *Journal of Aerospace Engineering* **16**, 65 (2003).
- [64] J. Y. Cho, *High-Performance Micromachined Vibratory Rate- and Rate-Integrating Gyroscopes*, phd, University of Michigan (2012).
- [65] A. Kourepenis, J. Borenstein, J. Connelly, R. Elliott, P. Ward, and M. Weinberg, in *Position Location and Navigation Symposium, IEEE 1998* (1998) pp. 1–8.
- [66] J. Bernstein, S. Cho, A. King, A. Kourepenis, P. Maciel, and M. Weinberg, in *Micro Electro Mechanical Systems, 1993, MEMS '93, Proceedings An Investigation of Micro Structures, Sensors, Actuators, Machines and Systems. IEEE.* (1993) pp. 143–148.
- [67] T. Juneau, A. Pisano, and J. Smith, in , *1997 International Conference on Solid State Sensors and Actuators, 1997. TRANSDUCERS '97 Chicago*, Vol. 2 (1997) pp. 883–886 vol.2.
- [68] M. Weinberg, J. Connelly, A. Kourepenis, and D. Sargent, in , *AIAA/IEEE Digital Avionics Systems Conference, 1997. 16th DASC*, Vol. 2 (1997) pp. 8.5–33–8.5–40 vol.2.
- [69] W. Geiger, B. Folkmer, J. Merz, H. Sandmaier, and W. Lang, in , *The Eleventh Annual International Workshop on Micro Electro Mechanical Systems, 1998. MEMS 98. Proceedings* (1998) pp. 615–620.
- [70] R. L. Kubena, D. J. Vickers-Kirby, R. J. Joyce, and F. P. Stratton, *Journal of Vacuum Science & Technology B* **17**, 2948 (1999).
- [71] H. Song, Y. Oh, I. Song, S. Kang, S. Choi, H. Kim, B. Ha, S. Baek, and C. Song, in *The Thirteenth Annual International Conference on Micro Electro Mechanical Systems, 2000. MEMS 2000* (2000) pp. 520–524.
- [72] S. Kim, B. Lee, J. Lee, and K. Chun, in *The 14th IEEE International Conference on Micro Electro Mechanical Systems, 2001. MEMS 2001* (2001) pp. 30–33.
- [73] “Analog devices adxr614 data sheet,” ().
- [74] G. He and K. Najafi, in *The Fifteenth IEEE International Conference on Micro Electro Mechanical Systems, 2002* (2002) pp. 718–721.
- [75] S. Y. Bae, K. J. Hayworth, K. Y. Yee, K. Shcheglov, and D. V. Wiberg (2002) pp. 316–324.
- [76] M. Palaniapan, R. Howe, and J. Yasaitis, in *IEEE The Sixteenth Annual International Conference on Micro Electro Mechanical Systems, 2003. MEMS-03 Kyoto* (2003) pp. 482–485.
- [77] J. Kim, S. Park, D. Kwak, H. Ko, and D.-I. D. Cho, in *Micro Electro Mechanical Systems, 2004. 17th IEEE International Conference on. (MEMS)* (2004) pp. 556–559.
- [78] D. Karnick, G. Ballas, L. Koland, M. Secord, T. Braman, and T. Kourepenis, in *Position Location and Navigation Symposium, 2004. PLANS 2004* (2004) pp. 49–55.
- [79] J.-Y. Lee, S.-H. Jeon, H.-K. Jung, H.-K. Chang, and Y.-K. Kim, in *18th IEEE International Conference on Micro Electro Mechanical Systems, 2005. MEMS 2005* (2005) pp. 359–362.
- [80] M. Zaman, A. Sharma, and F. Ayazi, in *19th IEEE International Conference on Micro Electro Mechanical Systems, 2006. MEMS 2006 Istanbul* (2006) pp. 66–69.
- [81] H. Johari and F. Ayazi, in *IEEE 20th International Conference on Micro Electro Mechanical Systems, 2007. MEMS* (2007) pp. 47–50.
- [82] A. Sharma, M. Zaman, M. Zucher, and F. Ayazi, in *IEEE 21st International Conference on Micro Electro Mechanical Systems, 2008. MEMS 2008* (2008) pp. 6–9.
- [83] I. Prikhodko, S. Zotov, A. Trusov, and A. Shkel, in *Solid-State Sensors, Actuators and Microsystems Conference (TRANSDUCERS), 2011 16th International* (2011) pp. 2809–2812.



- [84] E. Sahin, S. Alper, and T. Akin, in *Solid-State Sensors, Actuators and Microsystems Conference (TRANSDUCERS), 2011 16th International* (2011) pp. 2817–2820.
- [85] I. P. Prikhodko, S. A. Zotov, A. A. Trusov, and A. M. Shkel, *Sensors and Actuators A: Physical* 24th IEEE International Conference on Micro Electro Mechanical Systems, **177**, 67 (2012).
- [86] S. W. Yoon, *Vibration Isolation and Shock Protection for MEMS.*, phd, University of Michigan (2009).
- [87] S.-H. Lee, S. Lee, and K. Najafi, in *Solid-State Sensors, Actuators and Microsystems Conference, 2007. TRANSDUCERS 2007. International* (2007) pp. 335–338.
- [88] S.-H. Lee, J. Cho, S. Lee, M. Zaman, F. Ayazi, and K. Najafi, in *IEEE 22nd International Conference on Micro Electro Mechanical Systems, 2009. MEMS 2009* (2009) pp. 753–756.
- [89] S.-H. Lee, *Wafer-Level Packaging for Environment-Resistant Microinstruments.*, phd, University of Michigan (2009).
- [90] J. Reid, V. Bright, and J. Kosinski, *IEEE Transactions on Ultrasonics, Ferroelectrics, and Frequency Control* **45**, 528 (1998).